Engineering Upgrades to the Motional Stark Effect Diagnostic on Alcator C-Mod

by

Robert Thomas Mumgaard

B.S. Mechanical Engineering (2008)
B.S. Interdisciplinary Engineering- Physics (2008)
University of Nebraska-Lincoln

Submitted to the Department of Nuclear Science and Engineering
in partial fulfillment of the requirements for the degree of

Masters of Science in Nuclear Science and Engineering

at the

MASSACHUSETTS INSTITUTE OF TECHNOLOGY

June 2015

Author .....
Department of Nuclear Science and Engineering
May 19, 2015

Certified by .....
Steven D. Scott
Principal Research Physicist, Princeton Plasma Physics Laboratory
Thesis Supervisor

Certified by .....
Ian H. Hutchinson
Professor, Department of Nuclear Science and Engineering
Thesis Reader

Accepted by .....
Mujid S. Kazimi
TEPCO Professor of Nuclear Engineering
Chair, Department Committee on Graduate Students

Engineering Upgrades to the Motional Stark Effect Diagnostic on Alcator C-Mod

by

Robert Thomas Mumgaard

Submitted to the Department of Nuclear Science and Engineering
on May 19, 2015, in partial fulfillment of the
requirements for the degree of
Masters of Science in Nuclear Science and Engineering

Abstract

The Motional Stark Effect (MSE) diagnostic deployed on the ALCATOR C-MOD tokamak previously experienced unacceptable calibration drift and sensitivity to partially-polarized background light that limited its ability to measure magnetic field pitch-angles. The need to identify the cause of the polarization drift and to characterize sources of error motivated the development of a robotic calibration system consisting of a motorized three axis positioning system and a light source capable of generating arbitrary polarization states. The system produces linear polarization angles with accuracy of $< 0.05°$, operates during maintenance periods, has a Lambertian and laser illumination source, and captures the complex diagnostic polarization response using a Fourier expansion of the detector signals in terms of even harmonics of the input polarization angle.

This study guided the fielding of a first-of-a-kind inter-shot calibration (ISC) system for the MSE diagnostic—a long sought capability. The ISC inputs high quality polarized light at four carefully chosen polarization angles into the diagnostic objective lens within ten seconds of the plasma discharge using a single high-precision moving part internal to the vacuum vessel. Fiber optics are used to sequentially illuminate the calibration polarizers via backlight scattering similar to an LCD screen, fully filling the view of each of the ten MSE sightlines with polarization angles repeatable to better than $0.05°$. The system has operated inside the vacuum for over 8500 cycles and is used to reconstruct the diagnostic calibration on a variety of timescales.

This system was used to identify thermal-stress induced birefringence in several of the diagnostic's lenses as the cause of polarization calibration drift. Gold-plated radiative heat-shields and low-conduction lens and periscope mounts thermally isolate the in-vacuum periscope, and a forced-flow active thermal control system regulates the ex-vessel periscope and vacuum window. This successfully controls the optic stress in thermal environment ranging $\pm 150°C$.

A high-throughput narrow-bandpass filter-based polychromator was developed as a new configuration for MSE detectors. The system allows high-spectral selectivity at an étendue of $> 15mm^2$ sr for four simultaneous polarization measurements on the same viewing sightline. It sequentially passes light among four different $< 0.9nm$ FWHM temperature-tuned filters to custom avalanche photodiode detectors operating at $NA = 0.6$. The polychromator is imaging, non-vignetting, high transmission, utilizes mostly off-the shelf optics, is easily aligned, remote-controlled and can be replicated at relatively low cost. This enables wavelength-interpolation of the MSE background light and simultaneous detection of different parts of the Stark manifold.

Thesis Supervisor: Steven D. Scott
Principal Research Physicist, Princeton Plasma Physics Laboratory

Thesis Reader: Ian H. Hutchinson
Professor, Department of Nuclear Science and Engineering

The walls between art and engineering exist only in our minds.
-Theo Jansen

ACKNOWLEDGMENTS

This work could not have been completed without the help and support of many different people. My advisor, Steve Scott, planted and nurtured the seed for many of the different engineering systems presented in this this thesis. His insight into possible approaches and possible pitfalls was invaluable, usually focusing the problem at hand into a few key components. Additionally, he has done an outstanding job of shepherding the projects through the myriad hurdles in engineering approvals and procurement, freeing me to design with imagination unhindered by the typical problems of building things at large laboratories. His perseverance in solving problems inherent in MSE systems is admirable.

Jinseok Ko and Howard Yuh first pointed out many of the problems that this thesis solves and performed early brainstorming of possible solutions. This is especially true of Jinseok whose sketches of an in-situ calibration system and in-vessel wire grid polarizer shutter were the starting point of the ISC system. His identification of thermal-stress induced-birefringence as a source of polarization drift and design and simulation work on the radiative heat shield was the trail-head of the thermal-control system. Howard's identification of the problems with beam-into-gas calibration, polarization aberrations inherent in mirrors, polarization calibration using Fourier decomposition, calibration with rotational stages, and first identification of polarized background light were all important in the evolution of the C-MOD MSE system. His later work on the ITER MSE system clarified the need to develop solutions to potential problems and the opportunity of using the C-MOD MSE installation for this purpose. Matthew Khoury, a freshman UROP, was integral in assembling the multi-spectral polychromators.

This work could not have happened without the insight and guidance of the C-MOD engineering team who helped flesh out engineering concepts, pointed out alternative paths, identified possible pitfalls, and provided suggestions for vendors, processes and materials, and told me when my ideas stunk (tactfully). Their help clarifying the important tokamak specific engineering issues (what is outgassing?, what are JxB forces?) was critical for the survival of the components. The expertise of Rui Vieria, Dave Terry, Jim Irby, Sam Pierson and Ed Fitzgerald were key to this enterprise. Learning with them through this process has been integral to my engineering education.

The technical staff at the PSFC made all this possible by cutting metal, baking components, helping with drawings, procuring components, and keeping the data system stable under my calibration

load. Mark Iverson, Bill Forbes, Josh Stillerman, Ron Rossati, and Tom Toland were always happy to help.

Thanks is also due to my physicist colleagues, many of whom questioned the complexity of or need for such systems but stood by me anyway, and were sometimes surprised that these systems worked and at just how hard MSE is to implement properly. Jerry Hughes, John Rice, and Matt Reinke were always supportive and listened to my latest ups and downs in MSE engineering.

Importantly, Mike Churchill spent several critical hours teaching and motivating me to fit through the very confining C-MOD vacuum ports, thus enabling me to become invessel certified even though I was a tight (and presently tighter) fit. Without the insights gained from my (too much) time inside the tokamak vessel and the ability to install this complex precision hardware myself this project would have been a flop, likely taking my PhD with it. Maria Silveria patiently babysat my many hours in vessel for which I am grateful. I apologize that the job always took longer than I said it would (similar to this thesis).

Ian Hutchinson deserves credit for proposing this document instead of trying to squeeze this engineering work into my already over-stuffed PhD thesis or relegating it to the purgatory known as PSFC reports. His support of the idea was likely key in obtaining department approval of this non-traditional "thesis as supplement to thesis" approach.

Thanks to my friends at the PSFC, chief among them Geoff Olynyk, Mike Garrett and Dan Brunner who offered moral support and humor when things did not go well which was the norm and not the exception. Lastly, thanks to my wonderful wife who tolerated my absence, listened intently to engineering discussions, smiled and nodded when I showed her parts, and proof-read this document (don't send notice of typos).

CONTENTS

LIST OF FIGURES

LIST OF TABLES

1 INTRODUCTION

An important problem for the development of tokamak fusion reactors is confidently specifying and realizing the desired current profile during non-inductive current drive. High-quality measurement of the current profile can then be compared to theory and to numerical simulations of current drive. These comparisons challenge the validity of the analytic and numerical models of current drive, and thus aid in the development of improved models. The ultimate goal is to increase confidence that the numerical models can be reliably used to predict and optimize the performance of future tokamak fusion reactors.

1.1 THE MOTIONAL STARK EFFECT DIAGNOSTIC

First a reliable method to measure the current profile is required. Various techniques have been developed to measure the current profile. The most successful technique is termed the Motional Stark Effect (MSE) diagnostic, which uses polarized light to determine the angle of the local magnetic field [1, 2].

The MSE diagnostic collects and analyzes polarized light from the tokamak diagnostic neutral beam (DNB). The measured polarization angle can be used to determine the magnetic topology using a geometric projection. From this measurement the current density can be calculated using a magnetic equilibrium reconstruction such as EFIT [3].

The most widely used and successful type of MSE diagnostic is termed MSE line-polarization (MSE-LP) a schematic of which of which is shown in Figure 1. The elements in a MSE-LP system are:

1. Light is emitted by a high energy neutral hydrogen beam (50keV on C-MOD) as the atoms are excited by collisions with the plasma ions and electrons and through spontaneous or stimulated de-excitation. This light is Stark split due to the large Lorentz electric field from the high velocity neutrals crossing the magnetic field. In installations to date, the single Balmer α line is split into nine different lines with the magnitude of the wavelength split being proportional to the magnetic field and the beam velocity. This emission is shifted away from the cold plasma edge emission due to the Doppler shift.

2. A periscope uses discrete sightlines to collect the emission from different regions along the beam trajectory. The light is transmitted out of the tokamak vacuum vessel using a set of polar-

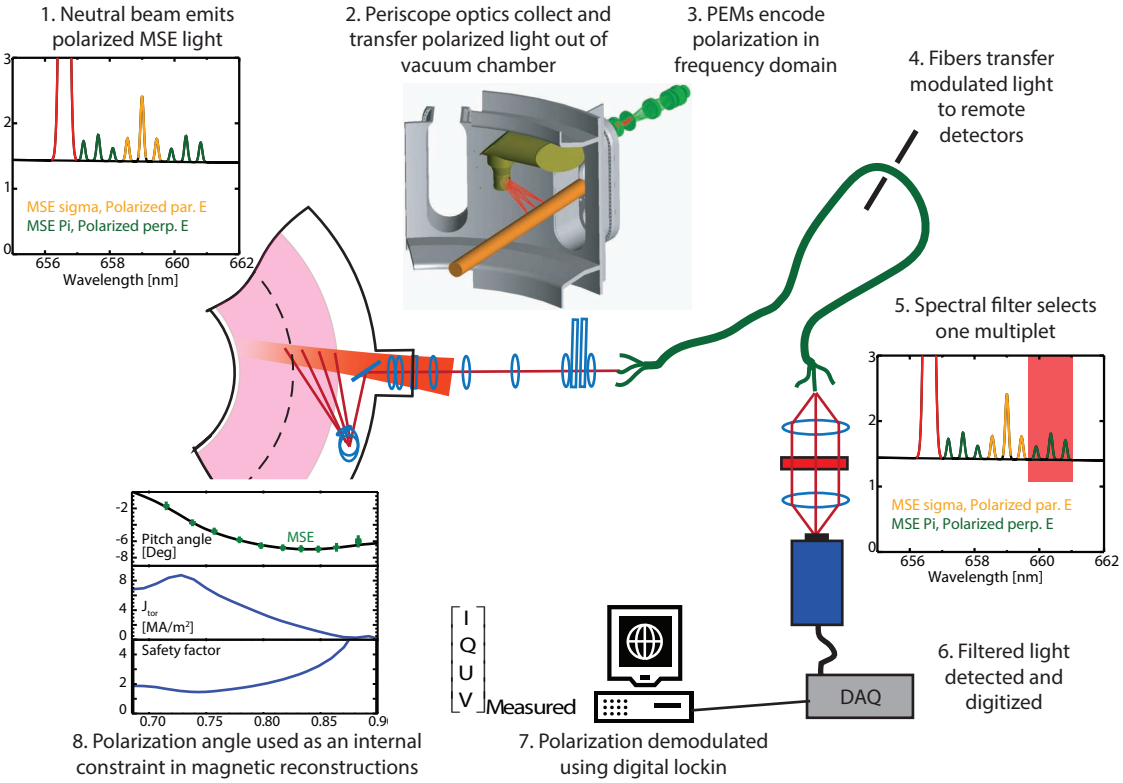

Figure 1: Layout of a MSE-LP system. Starting from the top left and moving clockwise.

ization preserving optics inside an optical periscope which also contains a vacuum window.

3. The polarized light is incident on a set of dual photo-elastic modulators (PEMs) which encode the polarization of the light into time-varying amplitude modulated signals [4–6].

4. The signal, now no-longer needing polarization preservation, is collected and transmitted from the tokamak to a diagnostic hall using traditional fiber optics.

5. The light is spectrally filtered for one of the three different MSE triplets (labeled π and σ, with the π lines to each side of a central σ triplet) using a narrow bandpass filter that is tuned to the proper spectral location to collect the desired lines.

6. The light is then detected by a high sensitivity detector, typically an avalanche photodiode (APD), and digitized with a fast digitizer.

7. The signal is later (and sometimes even in real-time) demodulated to obtain the polarization, represented as Stokes vectors.

8. The polarization angle from this process, which is related to the polarization angle incident on the diagnostic entrance pupil, is

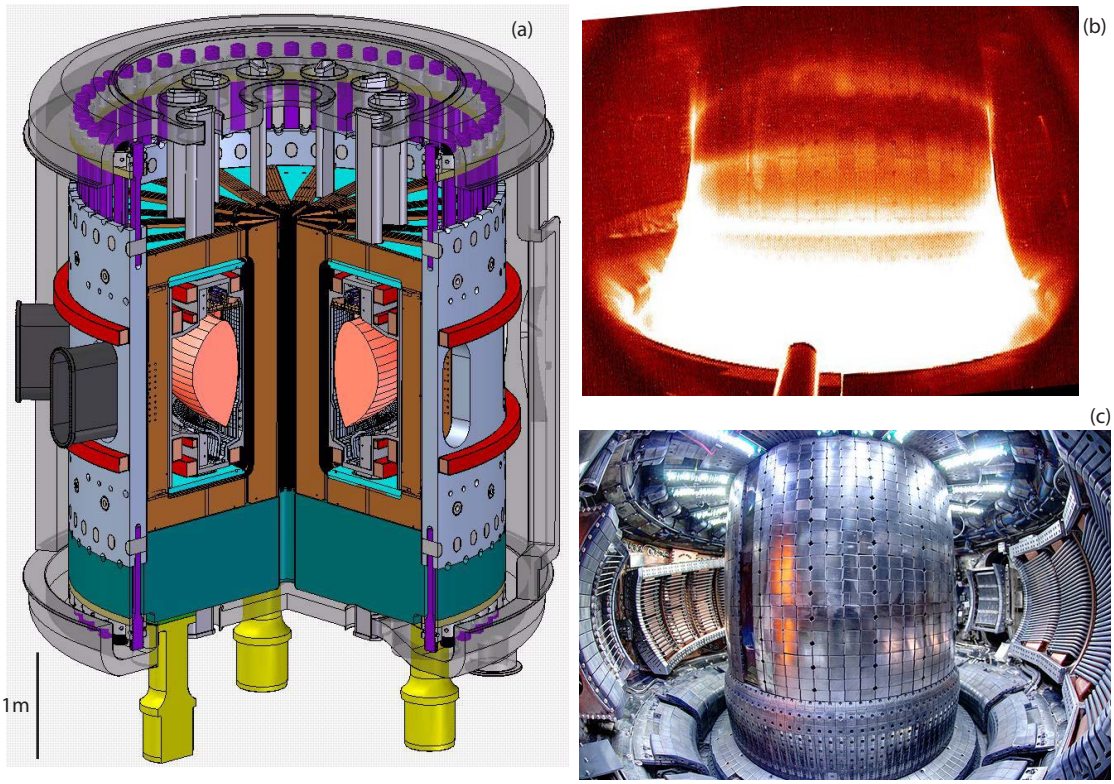

Figure 2: The ALCATOR C-MOD tokamak at MIT. An engineering diagram (a) showing the toroidal field magnets (brown), the poloidal field magnets (red), the supporting superstructure (gray), and the plasma (pink). A photo of the interior of the vessel during a plasma (b). The interior of the tokamak during a maintenance period (c). The LHCD launcher is visible immediately to the right of the central column (c). Photo credit: Robert Mumgaard.

then used to constrain the magnetic pitch angle in magnetic reconstructions, yielding a measured current profile across the plasma minor radius.

This process is well established and has been fielded on several tokamaks, providing significant physics results [7].

1.2 MSE ON ALCATOR C-MOD

The work in this thesis was conducted on the ALCATOR C-MOD tokamak at the Massachusetts Institute of Technology [8]. This tokamak is a compact machine operating at high magnetic field and high density, with metallic walls (molybdenum) and high-power radio frequency heating and lower hybrid current drive. The primary research directions include the study of core transport, radio frequency heating and current drive, and plasma-material interactions at the densities, magnetic fields, shaping, and power densities anticipated in a reactor.

The ALCATOR C-MOD tokamak presents several challenges for the MSE diagnostic. Its weak beam diagnostic beam, though good for

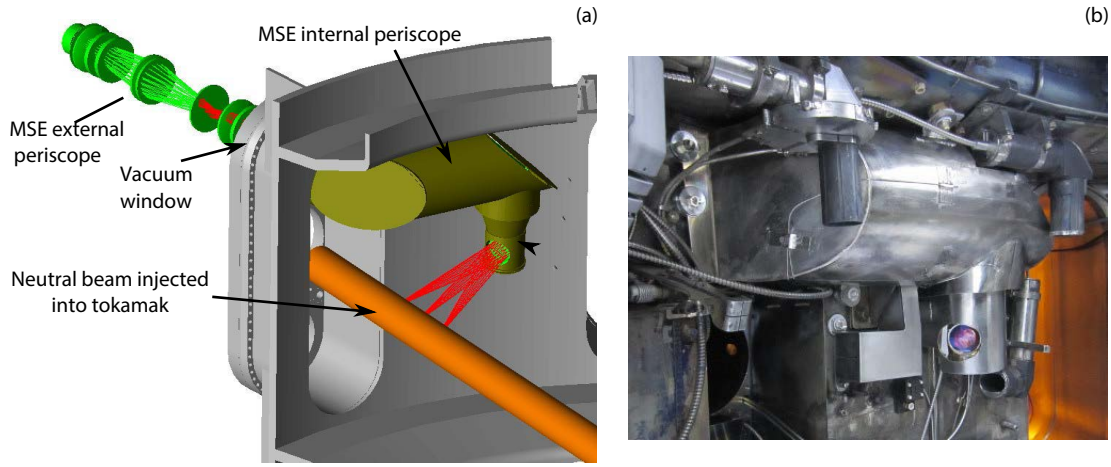

Figure 3: The internal and external MSE periscopes viewing the neutral beam (orange) (a) A photograph of the internal periscope covered by its radiative heat shield (b).

physics studies because it is non-perturbing, is dim and thus generates little signal. This is compensated by installing large étendue MSE optics. The compact machine requires a long optical periscope that must make several turns inside the vessel, something that had not previously been attempted with an MSE diagnostic. The many optical elements affect the polarization, creating polarization aberrations that need to be accounted for in the calibration and can make the diagnostic calibration sensitive to environmental changes. This is exacerbated by the unique construction of the tokamak. Components inside the vacuum vessel are exposed to the intense radiation from the plasma and the walls are heated to 65°C, but all the diagnostics must pass through the vacuum ports which are surrounded by transient cryogenic magnet cooling to ~ -100°C creating large thermal gradients.

The lack of access to the interior of the machine due to its small size makes calibrating or servicing the diagnostic arduous and challenging. Furthermore, since the diagnostic has many components inside the vessel it is prone to failure which can take the system off-line for the better part of a year. The small size and tight clearances inside the vessel require precise fabrication of components. The high field and current of the device leads to very large disruption forces on internal components which can break or deform them.

The MSE-LP system for ALCATOR C-MOD was proposed in 1997 [9] and designed from 1999 to 2002 as part of a collaboration between PPPL and the ALCATOR team [10]. The system was installed and commissioned by Howard Yuh and Steve Scott from 2000-2005 [11]. Necessary upgrades were added prior to the first physics result by Jinseok Ko from 2004-2008 [12]. Since the system's installation it has been almost completely rebuilt several times, both to withstand the

unforeseen harsh operational conditions inside ALCATOR C-MOD and to provide the necessary accuracy and confidence for physics studies.

A complex periscope is used to collect the light from an optimal location as shown in Figure 3. This periscope uses five lenses and three mirrors mounted inside the vessel vacuum to transfer the light to the single vacuum window that is positioned immediately above the DNB duct entrance. To allow for assembly and view optimization, this internal periscope is composed of two distinct and separable supporting components, designated the "canister" and the "turret". Due to the large radial build of the C-MOD support structure and cryostat, the light is further transported radially in air using five lenses. Finally, it is incident on the dual-PEM-based polarimeter.

The dual-PEM-based polarimeter with PEMS operating at 20 and 22kHz encodes the polarization of the light into amplitude-modulated frequency components. After being encoded by the PEMS, the light is focused by the tenth lens onto a curved image plane. A set of ten $\sim$ 30m fiber bundles, each containing 16 1mm core diameter (numerical aperture $= 0.37$) fibers, collect the light at the image plane and transmit it out of the tokamak cell to the the diagnostic hall $\sim$ 20m away. The ten optical fiber bundles each input the light into a filter oven assembly. Each oven contains lenses that collimate the light through a narrow-bandpass (FWHM $0.4 - 0.8$nm) 50mm diameter optical interference filters and refocuses it onto 10mm diameter avalanche photo-diode (APD) detectors. The filter ovens are temperature controlled to tune the bandpass of the filters to only pass the desired part of the beam emission spectrum.

The APDS detect the frequency modulated light with high quantum efficiency (~ 0.9) and internal gain ($M = 30 - 100$). The output current is amplified by a trans-impedance amplifier (2×10^7 V/A) integrated into the APD module before the signal is recorded by a 16 channel, 14-bit, differential analog to digital converter sampling at 1MHz. The square wave drive signals from each of the PEMS are transmitted over a fiber optic link from the PEM drivers in the tokamak cell to the diagnostic lab and are digitized with the same unit. The data, with setup parameters, calibrations, and analysis is stored in the MDSPLUS database system and a digital lock-in analysis program calculates the polarization angle incident on the objective lens of the diagnostic system using a calibration.

1.2.1 *Problems in the diagnostic performance*

As indicated by its long development time, MSE has been a difficult diagnostic to implement on C-MOD. The tokamak geometry forces the system to use a complex optical train inside the vacuum vessel. Previous work involved developing robust optics and new calibration strategies [11] and showed that temperature variations during an ex-

perimental run day are responsible for stress-induced birefringence in lenses [12]. This is believed to cause the calibration drifts that have been observed in the diagnostic and that limit its use. Other systematic errors are present in the diagnostic affecting the measured polarization angle. These need to be systematically explored and minimized. Ultimately, in-situ calibration of the diagnostic is required.

The high plasma density in the C-MOD tokamak generates copious light, some of which is in the wavelength band used for the MSE measurement. The interior of the tokamak is covered in shiny tile and other reflective surfaces with complicated geometries, which leads to significant reflected light entering the MSE diagnostic sightlines. Unfortunately, this background light becomes partially polarized upon reflection, thus in addition to the (desired) polarized light generated by the beam, MSE also observes partially polarized background light that can vary rapidly in time and space. Unless this polarized background light can be measured and accurately subtracted from the total measured signal, the polarization angle measurement will be skewed. A novel polarization polychromator is required to enable this multi-spectral MSE measurement.

The problem of calibration drift is a general problem with MSE diagnostics, particularly ones that have complex optical periscopes with the associated polarization errors. It is anticipated that future devices will have significant polarization aberrations that will also be time-varying due to the deposition on and/or erosion of the plasma-facing first mirror in the neutron shielding labyrinth. In-situ calibration is therefore anticipated. Future burning plasma tokamaks will likely have very bright backgrounds and relatively weak polarized light from the beam due to large reflections and poor beam penetration leading to significant errors in polarization angle absent accurate background subtraction.

1.3 SUMMARY OF NEW RESULTS

The work comprised in this thesis involved performing several upgrades to the C-MOD MSE diagnostic to enable it to be used to perform systematic studies of the current profile during Lower Hybrid Current Drive (LHCD) which is a promising technique to modify the current profile and therefore the magnetic geometry. Current drive is required for steady-state tokamak operation and therefore developing techniques and simulations and comparing those measurements to numerical simulations is of high priority. These upgraded systems present unique engineering challenges due the precision, reliability and robustness required to operate on and inside of the tokamak. The four main engineering subsystems developed in this thesis are:

1. **A robotic polarization calibration system.** This system is used to accurately and remotely calibrate the MSE diagnostic dur-

ing maintenance periods when personnel can enter the tokamak. The system can calibrate the diagnostic to better than 0.05 degrees in absolute polarization angle relative to gravity. The system includes two sources of polarized light, a Lambertian source that is used to flat-field calibrate the diagnostic and a laser-source used to perform polarized ray-tracing of the diagnostic. The robotic operation allows the system to operate remotely for long periods of time to systematically explore how the polarization calibration of the diagnostic depends on operating conditions. The system involves interfacing with the C-Mod database and control system, and high reliability and flexible operation is desired. The primary challenge is to produce such an accurate source of polarized light and to control it robotically. This is the first calibration system of its kind and should be applicable to other tokamaks around the world.

2. **The development of an in-situ calibration system for the MSE diagnostic** An electro-mechanical-optical system is required to calibrate the MSE diagnostic at arbitrary times during a campaign. This system inputs light with four known polarization angle into the diagnostic objective lens inside the tokamak vacuum vessel within centimeters of the multi-million degree plasma. The system must be accurate to 0.05 degrees and must be absolutely reliable or else it jeopardizes the use of the entire MSE diagnostic, impacting the team that depends on it. The primary challenges for deploying this system are the constraints imposed by operating with such precision inside the tokamak environment. The system operates in atmosphere to ultra-high vacuum, experiences temperature changes of over 100°C and accelerations of up to 200g's. The system carries its own illumination source inside the vessel to enable calibration during any situation and is designed to provide a uniform illumination source. In-situ calibration systems have been long-sought by the diagnostic community and will be essential for the operation of MSE diagnostics on next-generation tokamak experiments and reactors.

3. **The development of thermal mitigation strategies and hardware for the MSE diagnostic.** The diagnostic requires thermal isolation from its harsh environment. This includes the installation of a radiative heat shield internal to the machine which isolates the internal periscope from plasma radiation and an external active thermal control system for the external components, particularly the vacuum window. Extensive modeling is required to develop a system that can provide the adequate thermal isolation in such harsh, confined environments. The thermal system includes specialized high-strength lens mounts and

periscope supports that can survive large forces during tokamak disruptions while still providing thermal isolation. The thermal control system also includes a 32 channel thermocouple monitoring system which is used to evaluate the performance of the upgrades.

4. **The development of a high-throughput, high-spectral selectivity polarization polychromator.** This system is used to simultaneously detect polarized light at four different wavelengths on the same sightline, enabling new types of MSE measurements to be performed. The work primarily involves the design of a large imaging polychromator taking care to ensure proper operation of highly-specialized narrow-bandpass filters. The optical layout requires optimization and the design of custom optical components. The development of the opto-mechanical design requires care to ensure that the large optical system can be easily aligned to prevent vignetting. Custom thermal ovens are incorporated into the design to enable the center wavelengths of the narrow bandpass filters to be adjusted remotely. The specification of the filter passbands was based on studies of light from the tokamak to identify impurity free regions that can be used to measure the MSE background. High sensitivity avalanche photodiode detectors are designed to detect the relatively weak signals form the beam. A power and control system enables the entire detector to be commanded remotely. This system replaces the existing MSE detectors on C-MOD. It is anticipated that the design will be replicated for use on other tokamaks.

It is hoped that these major engineering upgrades will enable better physics utilization of this challenging diagnostic and experience gained will inform others who work on these diagnostics on other fusion experiments.

BIBLIOGRAPHY

[1] F. M. Levinton, R. J. Fonck, G. M. Gammel, R. Kaita, H. W. Kugel, E. T. Powell, and D. W. Roberts. Magnetic field pitch-angle measurments in the PBX-M tokamak using the motional Stark effect. *Physical Review Letters*, 63(19):2060, November 1989.

[2] F. M. Levinton. The motional Stark effect: Overview and future development (invited). *Review of Scientific Instruments*, 70(1):810–814, January 1999.

[3] L. L. Lao, H. St John, R. D. Stambaugh, A. G. Kellman, and W. Pfeiffer. Reconstruction of current profile parameters and plasma shapes in tokamaks. *Nuclear Fusion*, 25(11):1611, November 1985.

[4] G. R. Boyer, B. F. Lamouroux, and B. S. Prade. Automatic measurement of the Stokes vector of light. *Applied Optics*, 18(8):1217–1219, April 1979.

[5] Baoliang B. Wang. Stokes polarimeter using two photoelastic modulators. In *Proceedings of SPIE*, pages 1–8, Seattle, WA, USA, 2002.

[6] Mattias Kuldkepp, Nick C. Hawkes, Elisabeth Rachlew, and Beatrix Schunke. Accurate polarization measurements with a dual photoelastic modulator. *Applied Optics*, 44(28):5899–5904, October 2005.

[7] R. Mumgaard. Review of Results from MSE Diagnostics. MIT PSFC Research Report PSFC/RR-15-2, MIT, April 2015.

[8] M. Greenwald, A. Bader, S. Baek, M. Bakhtiari, H. Barnard, W. Beck, W. Bergerson, I. Bespamyatnov, P. Bonoli, D. Brower, D. Brunner, W. Burke, J. Candy, M. Churchill, I. Cziegler, A. Diallo, A. Dominguez, B. Duval, E. Edlund, P. Ennever, D. Ernst, I. Faust, C. Fiore, T. Fredian, O. Garcia, C. Gao, J. Goetz, T. Golfinopoulos, R. Granetz, O. Grulke, Z. Hartwig, S. Horne, N. Howard, A. Hubbard, J. Hughes, I. Hutchinson, J. Irby, V. Izzo, C. Kessel, B. LaBombard, C. Lau, C. Li, Y. Lin, B. Lipschultz, A. Loarte, E. Marmar, A. Mazurenko, G. McCracken, R. McDermott, O. Meneghini, D. Mikkelsen, D. Mossessian, R. Mumgaard, J. Myra, E. Nelson-Melby, R. Ochoukov, G. Olynyk, R. Parker, S. Pitcher, Y. Podpaly, M. Porkolab, M. Reinke, J. Rice, W. Rowan, A. Schmidt, S. Scott, S. Shiraiwa, J. Sierchio, N. Smick, J. A. Snipes, P. Snyder, B. Sorbom, J. Stillerman, C. Sung, Y. Takase,

V. Tang, J. Terry, D. Terry, C. Theiler, A. Tronchin-James, N. Tsujii, R. Vieira, J. Walk, G. Wallace, A. White, D. Whyte, J. Wilson, S. Wolfe, G. Wright, J. Wright, S. Wukitch, and S. Zweben. 20 years of research on the Alcator C-Mod tokamak a). *Physics of Plasmas (1994-present)*, 21(11):110501, November 2014.

[9] E. S. Marmar, J. L. Terry, W. L. Rowan, and A. J. Wootton. Diagnostic neutral beam and active spectroscopy requirements for the Alcator C-Mod tokamak (invited). *Review of Scientific Instruments*, 68(1):265, 1997.

[10] N. Bretz, D. Simon, R. Parsells, R. Bravenec, W. Rowan, N. Eisner, M. Sampsell, H. Yuh, E. Marmar, and J. Terry. A motional Stark effect instrument to measure q(R) on the C-Mod tokamak. *Review of Scientific Instruments*, 72(1):1012, 2001.

[11] H.Y. Yuh. *The Motional Stark Effect diagnostic on Alcator C-Mod*. PhD, Massachusetts Institute of Technology, 2005.

[12] J. Ko. *Current profile measurements using Motional Stark Effect on Alcator C-Mod*. PhD, Massachusetts Institute of Technology, 2009.

2

ROBOTIC CALIBRATION OF THE MSE DIAGNOSTIC

The optical components of the MSE periscope are optimized to preserve the polarization until it can be encoded by the PEMs. However, real imperfect optical components placed prior to the PEMs modify the polarization of the light being transmitted through them or reflected off of them. Furthermore, non-ideal operation of the PEMs can introduce additional systematic changes that can lead to errors if not properly accounted for. The optical polarization response, the action of the PEM-based polarimeter, the geometry of the view, and the bandpass of the spectral filters all require careful calibration.

The optimization of the diagnostic operation and the evaluation of sources of systematic error in the diagnostic will be important as MSE diagnostics become more complex, and are installed in harsher environments, and as physics studies demand more accurate measurements. In current and future fusion devices, it will be increasingly important to determine precise diagnostic calibrations, to determine the diagnostic's susceptibility to systematic errors, and to develop mitigation strategies without using machine operation time. Therefore, the development of calibration systems that can be used at various stages in the diagnostic deployment, including during development, in test environments, and in-situ, is important to ensure reliable diagnostic results.

This chapter summarizes previously demonstrated calibration techniques and then describes a robotic calibration system and its use for accurate polarization and geometric calibration of the MSE diagnostic on ALCATOR C-MOD during maintenance periods. The accuracy, repeatability, and limitations of the technique are discussed, as well as its capability to study systematic errors and sensitivities in the diagnostic response.

2.1 PREVIOUSLY USED CALIBRATION TECHNIQUES

In many tokamaks, the MSE calibration is determined using a beam-into-gas technique in which the neutral beam is fired into a gas-filled torus with the tokamak magnet system energized [1]. The calibration, relating measured PEM signals to the applied vacuum magnetic fields, is developed using successive shots or magnetic field ramps. The main advantage of this technique is that the diagnostic is calibrated in a situation very similar to the operational conditions during plasma

experiments, although the beam spectra has been shown to differ significantly [2]. Unfortunately, the prompt polarized emission from the beam is partially polluted by emission from secondary beam neutrals. These are neutrals that ionize, then gyrate about the local magnetic field—changing their local velocity direction—and then recombine or charge exchange and emit a photon before leaving the viewing volume [3]. Some of this secondary neutral emission has Doppler shifts and Stark splits, such that it falls within the bandpass of the diagnostic's filters. The polarization of this emission is thus captured by the diagnostic by the diagnostic. This collected light is emitted at random positions during a gyro-motion, thus the Lorentz electric field is not easily related to the background magnetic and electric fields. This emission, though dimmer than the primary beam neutral emission, systematically biases the net collected polarization during a beam-into-gas discharge making the calibration difficult to interpret.

The effect is strongest in tokamaks with near radial beam injection, such as ALCATOR C-MOD, and increases as the torus gas pressure is increased. Low gas pressures are thereby required, thereby increasing the necessary signal integration time. Although progress has been made in understanding the beam-into-gas experimental results, beam-into-gas calibration remains difficult to interpret in some operating regimes—especially those on C-MOD. However, future large tokamaks, including ITER, may limit operation of beam-into-gas experiments due to potential damage to the plasma-facing components from neutral beam shine-through[4], meaning other calibration techniques will need to be developed.

Other neutral beam-based techniques have been developed in which the edge magnetic pitch angle of the plasma is used to calibrate the MSE sightlines near the edge of the plasma using the known plasma current and data from external magnetic diagnostics. The input polarization angle is scanned at multiple sightlines either through plasma position jogs [5–7] or the plasma current is ramped at various plasma sizes [8]. Although these techniques capture the full diagnostic response, they require significant dedicated tokamak plasma operation time to establish a calibration database. This impacts tokamak availability while only providing a limited calibration range. Additionally, these techniques rely on magnetic reconstructions of the plasma edge, which may introduce systematic sources of error.

The neutral beam-based techniques require dedicated machine operation time with the nominal magnetic field while providing only a very limited set of calibration data. This makes it difficult to characterize systematic errors and sensitivities in the diagnostic or to explore novel operational modes. It is therefore desirable to develop a calibration technique that can be performed during a maintenance period that would not impact tokamak operation and would allow the di-

agnostic response to be studied comprehensively using many high resolution, repeated calibrations.

Historically, the discharge-based MSE calibrations on C-MOD have been complemented by invessel calibrations that illuminate the diagnostic with linearly polarized light from a high precision, rotatable polarized light source. The polarized light source was manually positioned at each of the ten MSE sightlines and manually oriented to illuminate the MSE objective lens. Similar techniques have been implemented on the DIII-D [9] and JET [10] tokamaks. This system provided an accurate calibration of the diagnostic response to polarized light (relative polarization angle accuracy $\sim 0.05°$), but was tedious. It required significant manned time invessel and additional techniques to calibrate the diagnostic geometry. Additionally, it was susceptible to mis-alignment errors and was not as accurate in absolute angle as desired to investigate systematic errors.

This chapter describes the development and use of a robotic calibration system that automatically positions and orients a precision polarization generation source at each MSE sightline and also determines the diagnostic geometry self-consistently. The system illuminates the diagnostic with light having a precisely controlled polarization state from a precisely controlled position inside the tokamak. It also determines the MSE measurement geometry using the same high-precision hardware. The system is comprised of a three-axis positioning system, a high precision polarization generation head, and control software. The robotic calibration system decreases the time required for a complete MSE calibration by an order of magnitude relative to the previous manual approach while increasing calibration accuracy and repeatability. The increased performance facilitates studies of diagnostic effects, such as non-ideal performance of the PEM-based polarimeter, variability of the diagnostic response due to birefringence in the relay optics, and the effects of non-ideal mirrors. The technique provides high-fidelity calibration of the diagnostic in multiple operational modes to optimize performance. The use of this system has substantially expanded the understanding of the operation of PEM-based MSE systems and has increased confidence in the diagnostic performance and physics results based on the diagnostic measurements.

2.2 ROBOTIC POSITIONING SYSTEM

One key part of the diagnostic calibration is to provide light from a known location inside the tokamak. Calibration heads are aligned to a laser that traces the neutral beam trajectory and are pointed toward the MSE objective lens using a three-axis positioning system. This system uses precision screw adjustments and a stepper-motor actuated linear translation stage with a positioning accuracy of $\pm 15\mu m$ and a repeatability of $< 2.5\mu m$ to translate components along the neutral

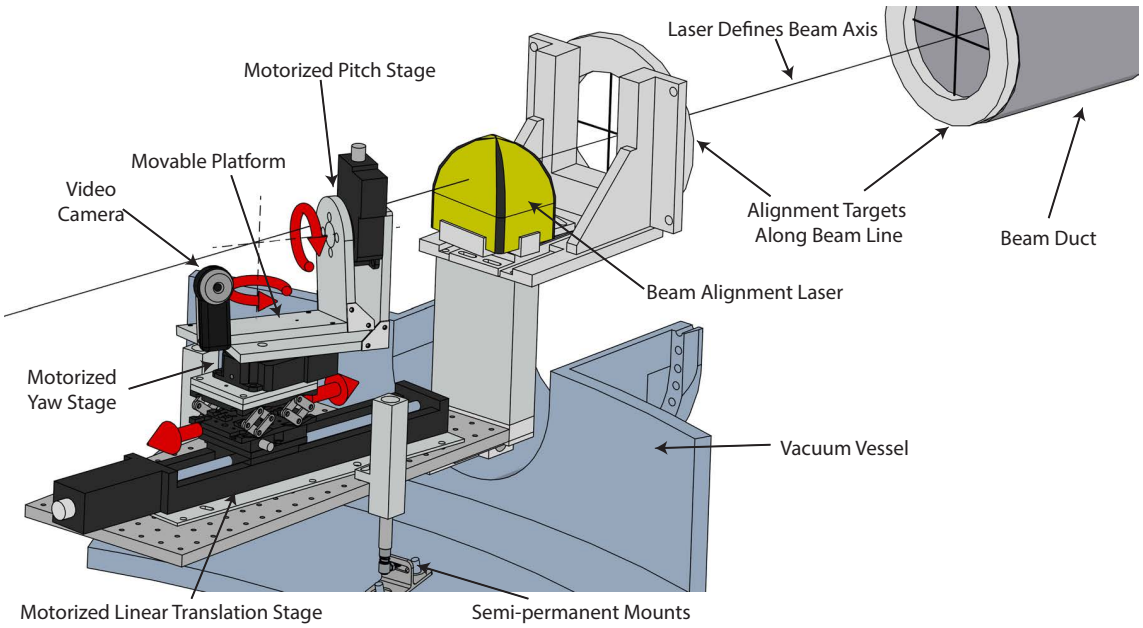

Figure 4: The positioning system of the robotic calibration system. A laser is aligned coincident to the beam axis using targets inserted in the beam duct during maintenance periods. The motorized linear translation stage is aligned to this laser and can translate along the low-field side of the beam trajectory. Mounted to the moving element of this stage are two orthogonally orientated motorized rotational stages. These stages move a platform in the pitch and yaw directions with the pivot point centered on the beam axis. Various calibration heads can be placed on this platform.

beam line. This motorized stage can travel along the entire low-field side beam trajectory, covering the entire field of view of the ALCATOR C-MOD MSE diagnostic. The linear stage carries two stepper-motor actuated rotation stages mounted orthogonally to one another to point calibration heads in the proper direction. These rotation stages move a platform in the pitch and yaw directions with the pivot point centered on the beam axis with a positioning accuracy of $\pm 0.05°$ and a repeatability of $< 0.02°$. This system thus creates a platform that can be located at any point along the beam axis on the low-field side of the tokamak and can be oriented to point in any desired direction. The positioning system is shown in Figure 4.

2.3 POLARIZATION GENERATION HEAD

The positioning system typically carries a precision polarization generation head that creates user-defined polarization states. The head consists of a large stepper-motor actuated rotational stage with positioning accuracy of $\pm 0.02°$ with a repeatability $< 0.003°$. A dichroic linear polarizer is mounted on the calibration side of the rotating element of the stage. The transmission axis of the linear polarizer is calibrated using a Malus-law calibration technique detailed later in this section. The orientation of the tokamak vacuum magnetic field is typically well known relative to gravity and to the other magnetic

diagnostics [11, 12], thus the MSE diagnostic polarization response is calibrated with respect to the local gravity direction using an electronic inclinometer attached to the base of the stage. This inclinometer determines the position of the base relative to gravity to $< 0.02°$ in two orthogonal directions (pitch and roll).

A removable, digitally controlled, variable liquid-crystal retarder is optionally mounted in front of the linear polarizer with its fast axis angled 45° with respect to the linear polarizer's transmission axis. The unit's retardance can be varied to impart over a quarter-wave of retardance, thus generating fully circular polarized light.

Two light sources are mounted on the opposite side of the rotational element. One source consists of a uniformly spaced array of 196 red LEDs (40 nm FWHM centered at 640 nm) behind an optical diffuser. This creates a nearly Lambertian red light source with a controllable brightness with a clear aperture of approximately 75 mm diameter. The other source is a red laser diode (5 mW @ 655 nm) mounted behind the LED array and aligned to shine along the rotation axis of the rotational stage through a small hole in the LED array and diffuser. The rotational stage carries the polarizer, retarder, LED array, and laser as a single unit as it rotates.

The polarization generation head can therefore generate arbitrary Stokes vectors with either a Lambertian or a laser light source, with polarization ellipticity ranging from 0 to 1 with total polarization fraction > 0.99 and with an azimuthal polarization angle known to better than $0.05°$ relative to gravity. For typical MSE calibrations, the system is operated without the variable retarder since the calibration is concerned predominately with linearly polarized light. The polarization generation head is shown in Figure 5.

The polarization generation head is mounted on the positioning system platform with its rotation axis orthogonal to both the pitch and yaw axis of the position system. In this configuration, the calibration system is capable of generating arbitrary polarizations with a user-specified $\vec{k}$ that always intersects the neutral beam axis from a Lambertian source. This is ideal for approximating the motional Stark emission from the neutral beam.

2.4 CALIBRATION OF THE TRANSMISSION AXIS OF THE LINEAR POLARIZER

The polarization head is capable of creating very repeatable polarizations and relative changes, but the polarization angle relative to gravity needs to be calibrated. This has several components:

$$\theta_{\text{polarization}} = \theta_{\text{level angle}} + \theta_{\text{stage angle}} - \theta_{\text{TA offset}} \tag{1}$$

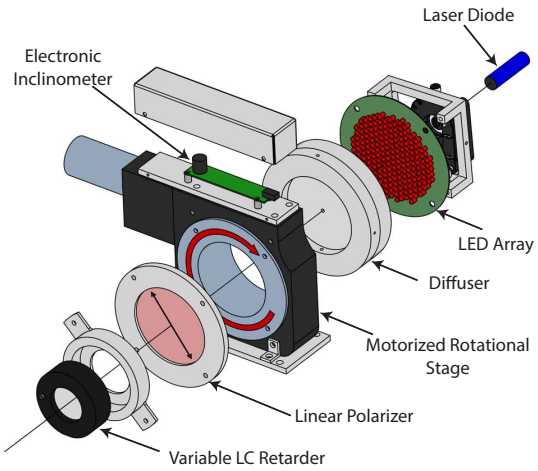

Figure 5: The polarization head assembly. The polarization generation head is capable of generating light with arbitrary polarization states using a variable liquid crystal retarder mounted at 45° relative to the transmission axis of a dichroic linear polarizer. A red LED array behind an Opal glass diffuser generates a nearly Lambertian polarized plane source, or a laser diode generates a polarized ray coincident with the rotational axis of the system. All the components are mounted on a stepper-motor-based precision rotational stage. An electronic inclinometer mounted to the stage base references the polarization parameters relative to gravity.

where $\theta_{\text{level angle}}$ is the angle of the stage base with respect to gravity measured by the electronic inclinometer, $\theta_{\text{stage angle}}$ is the angle of the polarization generation stage relative to its base which is known to high accuracy from the stepper-motor encoder, and $\theta_{\text{TA offset}}$ is the angle of the transmission axis of the linear polarizer relative to the rotating part of stage on which it is fixed. The last angle is not known a-priori, thus a bench calibration using Malus's law has been performed to measure it.

In this calibration, a laser shines through a beam expander then through a high-quality polarizing beam splitter that is placed on a stage and leveled relative to gravity using a high precision digital level. The laser beam then shines through the linear polarizer mounted on the polarization generation head (with the sources removed) and is then focused and detected by a photodiode with a trans-impedance amplifier. The setup is shown in Figure 6. A polarizing beam splitter is chosen because the transmission axis is well-defined relative to the sides and the variation of the transmission axis across the beam splitter is small [13].

The polarization head is commanded through a series of $\sim$ 600 angles spanning several revolutions, and the voltage from the photodiode, $\theta_{\text{level angle}}$, and $\theta_{\text{stage angle}}$ are recorded. The resulting voltage follows Malus's law:

$$\frac{V_{\text{transmitted}}}{V_{\text{incident}}} = \text{ER} + (1 - \text{ER}) \cos^2(\theta_{\text{beam splitter}} - \theta_{\text{polarization}}) \tag{2}$$

where ER is the extinction ratio of the polarizer pair and $\theta_{\text{beam splitter}} = 0°$ or $90°$, depending on the orientation of the beam splitter.

The voltage from the photodiode is then fit to the equation:

$$\frac{V_{\text{transmitted}}}{V_{\text{incident}}} = \text{ER} + (1 - \text{ER}) \times \cos^2\left(\theta_{\text{beam splitter}} + \theta_{\text{level angle}} + \theta_{\text{stage angle}} - \theta_{\text{TA offset}}\right) \tag{3}$$

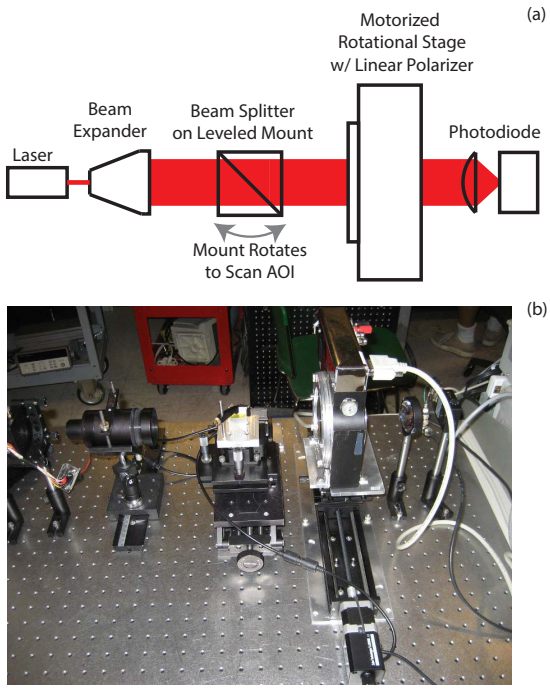

Figure 6: $\theta_{\text{TA offset}}$ is measured using a Malus's law setup in which a laser beam is expanded to ~ 1 cm diameter and passed through a polarizing beam splitter on a stage leveled to gravity before being passed through the polarization generation head and then focused onto a photodiode. The polarization generation head rotates the linear polarizer installed on it. The angle between the beam splitter and linear polarizer faces can be varied by rotating the beam splitter slightly (a). Photograph of the setup (b).

with V_{incident}, ER, and $\theta_{\text{TA offset}}$ as fitting parameters.

A sample set of data and the resulting fit and fit residuals are shown in Figure 7. The fit is performed over various angle ranges from $\pm 30°$ to $\pm 360°$, and the fit parameters are observed to be independent of the subset of data used. The fit parameters are also independent of which direction the stage moves, or if the angles are randomly chosen, indicating there is no significant hysteresis in the polarization head operation.

The stability of the laser source and detector was monitored and found to vary $< 0.1\%$ over the timescale of the data acquisition which is ~ 0.5 hr. The test was done at multiple detector orientations with negligible difference, indicating that the detector is polarization insensitive.

The $\theta_{\text{TA offset}}$ from the fit depends on the angle between the beam splitter face and the linear polarizer face due to a geometric projection. Both of the faces are plumb, leaving one free parameter. The stage upon which the beam splitter sits is rotated slightly about its vertical axis to scan the angle between these two faces. The beam splitter is then flipped 180° about the vertical axis and the angle of incidence (AOI) scan is repeated, reversing the projection. The cube is then flipped 180° about the laser axis and the process is repeated. This yields four sets of fitted $\theta_{\text{TA offset}}$ vs. AOI. The two faces are most parallel where the curves cross, yielding an accurate estimate of $\theta_{\text{TA offset}}$. This process is shown in Figure 8. The process was repeated

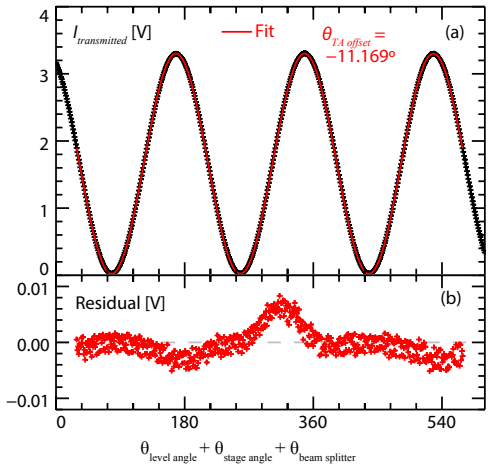

Figure 7: The light intensity as the polarizer is rotated is fit using Equation 3 to determine the $\theta_{TA\ offset}$ (a), yielding small residuals (b).

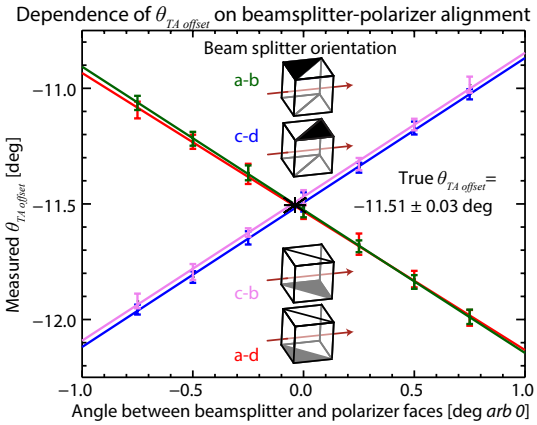

Figure 8: The angle between the beamsplitter face and the linear polarizer face is varied by rotating the beam splitter about its vertical axis. This results in a change in the fitted $\theta_{TA\ offset}$ (a-b). The beam splitter is flipped 180° about the vertical axis and the scan is repeated (c-d). The beam splitter is then rotated 180° about the laser trajectory and the process is repeated again (c-b, a-d). The location where the four sets of data cross indicates where the two faces are most parallel yielding an accurate $\theta_{TA\ offset}$.

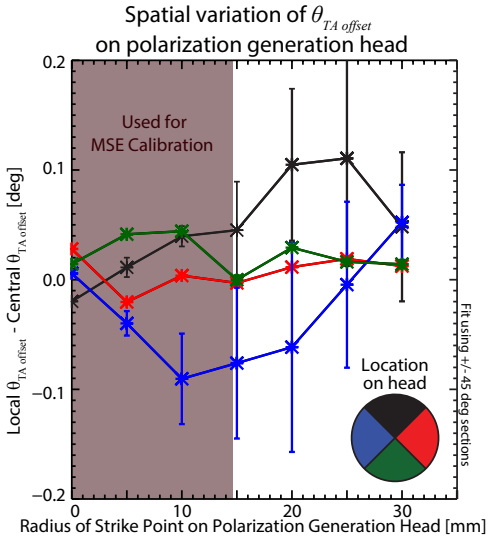

Figure 9: The spatial variation of $\theta_{TA\ offset}$ across the face of the polarization generation head is calculated by performing Malus's law fits over $\pm 45°$ portions of the polarizer face. The gray shading represents the region sampled by a MSE sightline during a calibration.

with a beam splitter from another manufacturer, yielding consistent results.

The spatial variation of $\theta_{TA\ offset}$ across the face of the polarization generation head is determined by varying the location at which the expanded laser beam impacts the linear polarizer instead of having it impact the polarizer at the center. The laser beam then traces an annulus on the face of the linear polarizer as the polarization generation head rotates. A fit is then performed over $90°$ portions of the angular scan. This results in a measured variability of $\theta_{TA\ offset}$ (within the central 15 mm radius used to calibrate MSE) of $\pm 0.05°$, which is consistent with previous measurements of high performance dichroic linear polarizers [13]. The process and results are shown in Figure 9. Calibration of the MSE diagnostic utilizes a $\sim 360°$ rotation of the polarizer to minimize errors. In the future, the dichroic linear polarizer will be replaced by a wire grid polarizer to reduce this variability, which is the largest single source of uncertainty in this technique.

2.5 CALIBRATION WORK FLOW

The robotic calibration system is controlled via TCP/IP and serial communications using a custom software package written in MATLAB. Signals are routed from a portable computer and electronics system in the C-MOD cell via three cables to the calibration system inside the tokamak vacuum vessel. The computer controls the light source intensity and polarization parameters, positions the stages and the light source, triggers the MSE data acquisition system, sets the PEM retardances, sets the APD bias voltage, and has several analog and digital inputs and outputs for interfacing with other equipment. The control system contains logic that prevents movements that would cause collisions with other elements installed in the vessel or would damage

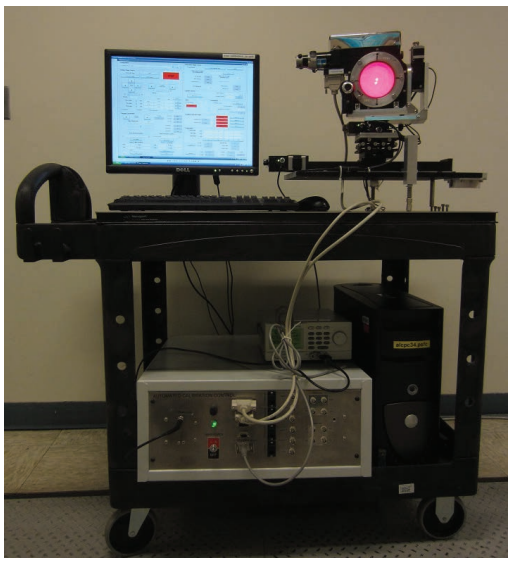

Figure 10: The MSE calibration system and its transportable support hardware outside the vessel. The system is controlled by a computer running a MATLAB program that communicates with the calibration system, triggers the MSE data acquisition, controls other processes, and allows the system to be commanded with a GUI.

the robotic components due to over-extension. The calibration system with control system is shown in Figure 10.

During calibration of the MSE diagnostic, the positioning system carries the polarization generation head to the intersection of an MSE sightline and the beam axis and points the polarization generation head axis at the center of the MSE objective lens. This aligns the linear polarizer perpendicular to the mean sightline $\vec{k}$. The polarization head illumination area is large enough to fully fill the sightline viewing volume. The system then rapidly generates various polarizations while triggering the MSE data acquisition system. It records the polarization state and other calibration information into the MDSPLUS database for each discharge.

Once sufficient data is taken to characterize a sightline, the system then typically moves to another MSE sightline. Alternatively, it varies other parameters such as the light intensity, the PEM retardance, or it activates heaters to change the temperature of the optics. The installed system, as it would appear during the calibration of an MSE sightline, is shown in Figure 11. The automated system has decreased the time required for a full calibration of all ten MSE sightlines from > 10 hrs to < 3 hrs. Faster and slightly less accurate modes of operation wherein the calibration system inputs multiple polarizations in the same data cycle reduces the required time further by a factor of 8, allowing the calibration to be determined in transient situations.

The C-MOD vacuum chamber is small and access is difficult. The system is therefore comprised of three pin-aligned components which fit through the narrow C-MOD vacuum entrance port. These components attach to sturdy, semi-permanent, ball-in-socket mounting points on the vacuum vessel in a highly reproducible way. The system can be installed and removed from inside the vessel by a technician in approximately fifteen minutes without tools or a lifting system. Once

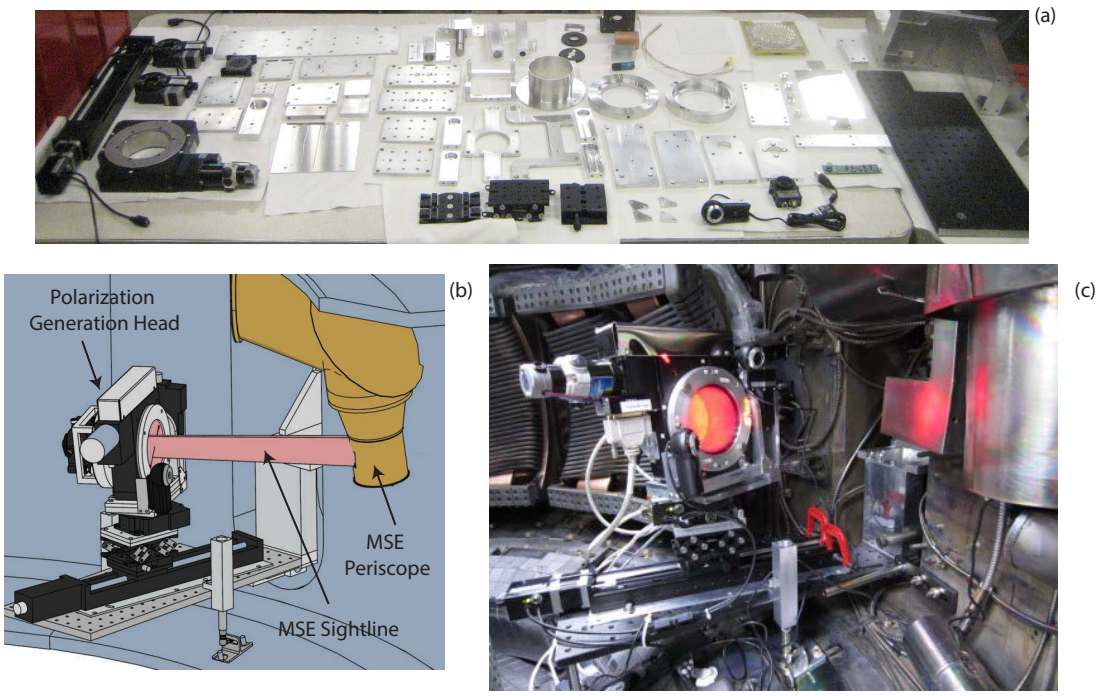

Figure 11: MSE calibration system parts (a). A schematic of the system installed invessel calibrating an MSE sightline. During the calibration, the polarization head is placed at the intersection of the beam and the MSE sightline to be calibrated and is pointed at the MSE objective lens, filling the sightline footprint with polarized light (b). The system, as built, installed calibrating the diagnostic (c).

installed, the calibration system performs an automated alignment procedure which is verified by pointing the laser at permanent landmarks inside the vessel.

The MSE calibration typically restricts manned access, precluding other maintenance activities. The system is therefore often installed at the end the day shift. It performs calibrations overnight without human oversight and is then removed in the morning to allow other work to continue. The system is re-installed to continue calibration with minimal loss of calibration accuracy at the end of the day's shift. Some work inside the vessel is compatible with the calibration, allowing the system to remain in place.

A digital video camera is incorporated into the positioning system with two additional cameras installed in the vessel to allow the system to be monitored remotely. The system performs a script of various calibration tasks, posts its progress in logs, and updates the MSE diagnostician via SMS text message. In addition to autonomous operation, the system can also be controlled remotely or from inside the vessel via a graphical user interface on a small laptop or tablet with a wireless connection. The system has operated with minimal human interaction for over 72 continuous hours and has been used for MSE calibrations since 2009.

2.6 GEOMETRIC CALIBRATION OF THE MSE DIAGNOSTIC

The polarization angle from the Motional Stark Effect is a function of the projection of the sightline onto the electric field in the atom's frame. This electric field is composed of the field from the plasma itself and the Lorentz field due to atom's traversing of the magnetic field at high velocity: $\vec{E} = \vec{E}_{plasma} + \vec{v}_{beam} \times \vec{B}_{plasma}$. The linear polarization angle relative to the toroidal plane of the σ multiplet (θ^{σ}_{pol}) emitted at a location in the plasma is therefore a function of the local field components, the beam velocity, and the viewing vector. The most general form for the polarization angle can be derived as:

$$\tan(\theta^{\sigma}_{pol}) = \frac{A_1 B_z + A_9 B_R + A_8 B_\phi + A_5 E_R/v + A_{10} E_\phi/v}{A_2 B_\phi + A_3 B_R + A_4 B_z + A_6 E_z/v + A_7 E_R/v + A_{11} E_\phi/v} \tag{4}$$

$$\begin{aligned}
A_1 &= -\cos(\alpha+\Omega)\cos\beta \\
A_2 &= \sin\alpha\cos\beta\cos\theta + \sin\beta\sin\Omega\sin\theta \\
A_3 &= \cos\alpha\cos\beta\cos\theta - \sin\beta\cos\Omega\sin\theta \\
A_4 &= \sin(\Omega+\alpha)\cos\beta\sin\theta \\
A_5 &= -\cos\Omega \\
A_6 &= -\cos\theta \\
A_7 &= \sin\Omega\sin\theta \\
A_8 &= -\sin\beta\cos\Omega \\
A_9 &= -\sin\beta\sin\Omega \\
A_{10} &= \sin\Omega \\
A_{11} &= \cos\Omega\sin\theta
\end{aligned}$$

where α is the angle between the beam velocity and local toroidal direction ($\hat{\phi}$) in the horizontal plane; β is the angle between the beam velocity and the horizontal plane; Ω is the angle between the sightline $\vec{k}$ and the local toroidal direction in the horizontal plane; θ is the angle between the sightline and the horizontal plane, and v is the beam scalar velocity. The geometry is shown in Figure 12 (a) and (b). It is apparent that an arbitrary MSE sightline's geometry calibration can be reduced to six numbers: angles α, β, Ω, and θ, and the major radius and height of the intersection between the sightline and the beam. The goal of the geometric calibration is to determine these six quantities for each sightline in an accurate and self-consistent manner. The small size and difficult access conditions of C-MOD makes measuring these quantities by hand difficult. Therefore, it was decided that the robotic calibration system should determine these remotely.

A set of alignment targets and a laser beam were used to align the duct and beam tank when the 50 keV diagnostic neutral beam [14] was installed inside the ALCATOR C-MOD experimental hall. After

the beam components were installed, the beamline gate valve and calorimeter were opened, allowing a laser beam to shine through the entire beam system and onto the beam acceleration grids to confirm that the grids were centered on the duct axis. During long duration maintenance periods, the beam alignment has been confirmed using IR imaging by firing the beam into castellated targets.

The alignment targets and laser are reinstalled in the beam duct and are used as a reference for the beam axis during maintenance periods. The calibration positioning system is then installed, and it is aligned so that the translation stage path is collinear with—and the pitch and roll axes intersect with—the laser tracing the beam axis.

An illuminated 1mm wide vertical slit is installed on the linear positioning stage in place of the polarization generation head to determine the viewing volumes of the MSE sightlines. This slit is moved in 1mm steps along the beam trajectory while the data acquisition is triggered. The detected signal intensity as a function of linear stage position can then be used to accurately determine the locations along the beam axis where the MSE sightline crosses the beam trajectory. The result is shown in Figure 12(c). The dual columns of fibers in each MSE sightline are evident along with the change in magnification from the optical axis (sightline 6) to the field extents (sightlines 1 and 10).

The geometric calibration angles and resulting coefficients are then determined at the centroid of each sightline viewing footprint. The positioning system's capability to accurately measure relative angles using stepper motors is used to determine the geometric calibration angles. This is done using only relative angle changes. To measure the location of the stage inside the tokamak, the stage moves in the yaw axis in the horizontal plane until the laser of the polarization generation head is tangent to one side of the center column of the tokamak. Then the stage rotates until the laser is tangent to the other side of the center column of the tokamak. The center column diameter is known very accurately, thus simple trigonometry yields the major radius at which the stage is located. The accuracy of the angle measurement is limited by the width of the laser beam and the tile shape of the inner wall and is typically $d\psi_1 \sim 0.3°$, resulting in an uncertainty of major radius of $dR_{view} \sim 1$mm. The local toroidal direction is perpendicular to the bisector of the angle between the two tangent positions.

The positioning system then points the laser through the targets in the beam duct and is finally pointed at the center of the MSE objective lens. The calibration angles Ω, θ, α, and β are derived from the relative angles and the inclinometer output. The geometry is shown in Figure 12 (a) and (b).

Once the position and orientation of the positioning system are determined inside the vessel at a few positions via this technique, the system can reliably calculate the appropriate calibration angles and

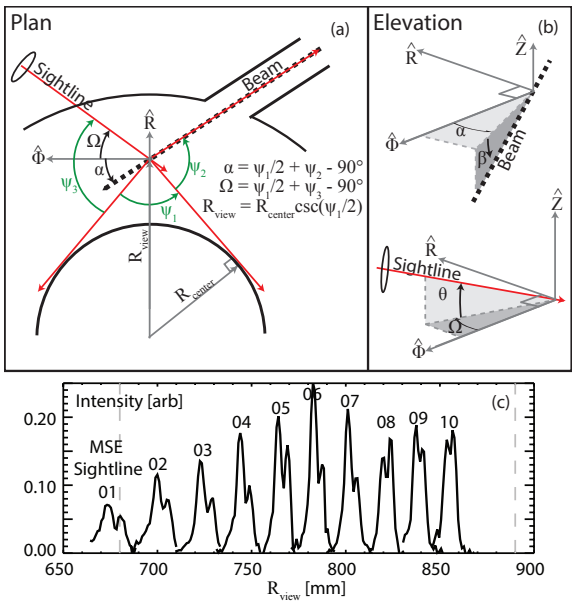

Figure 12: The angles used in the calibration of an MSE sightline are calculated from relative angle measurements obtained by the robotic calibration system. The polarization generation head laser (red) is brought tangent to the two sides of the tokamak center column (ψ_1), then pointed though the beam alignment targets (ψ_2) and then pointed at the MSE objective lens (ψ_3) (b). The vertical angles of the view and beam θ and β are measured using the inclinometer on the calibration system (c). The viewing volumes are measured by moving a 1mm wide slit along the beam trajectory while triggering the MSE detectors (c). The calibration angles are determined at the centroids of the sightline viewing volumes.

the major radius for any position along the beam trajectory. The accurate encoders in the system can also be used as a metrology tool to determine the absolute location of the diagnostic objective lenses or other features inside the vessel via triangulation from opposite ends of the translation stage. The absolute accuracy of the four angles is estimated at $< 0.5°$, and the absolute accuracy of the major radius and height of the view is estimated at $<$ 2mm using the robotic calibration system to make tangent measurements of the inner wall. The dominant geometric uncertainty is the location and trajectory of the DNB.

2.7 POLARIZATION CALIBRATION OF THE MSE DIAGNOSTIC

The linear polarization calibration relates the measured signal intensities at the second-harmonic PEM frequencies to the polarization angle of the linearly polarized light incident on the diagnostic objective lens. In an ideal PEM-based polarimeter, the polarization angle incident on the polarimeter is encoded in the amplitudes at the second harmonics of the PEMs ($I_{2\omega_1}$ and $I_{2\omega_2}$):

$$-\frac{1}{2}\tan^{-1}\left(\frac{J_2(R_2)}{J_2(R_1)}\frac{I_{2\omega_1}}{I_{2\omega_2}}\right) = \theta_{pol} \tag{5}$$

where R_1 and R_2 are the retardances of the first and second PEM, respectively. Both retardances are usually set to be near 3.054 radians, which maximizes the signal intensities at the second harmonics of the PEMs and makes the system insensitive to small drifts in the PEM retardance. Typically, the retardances of the two PEMs are assumed to be equal and the error associated with this assumption is incorporated

into the polarization calibration. Work is underway to incorporate on-line measurement of the PEM retardance into the data processing system.

Optical elements that are positioned in front of the polarimeter (lenses, mirrors, vacuum windows) modify the polarization state of the light incident on the polarimeter. In theory this can be accounted for using the Mueller matrix formulation for polarized light a priori using known component properties. Results have been discussed for a single non-ideal mirror [9, 10]. However, the inclusion of three non-ideal mirrors, many lenses, and a non-ideal polarimeter (e.g., slightly misaligned PEM or linear polarizer, or unequal PEM retardances, or finite PEM illumination) presents a highly non-linear system with a large number of required parameters. Additionally, each diagnostic sightline is composed of many rays that strike optical elements at different locations and angles of incidence and thus have different polarization modifications. The calibration of the sightline is thus a weighted average of these rays.

These effects cause Equation 5 to deviate from a linear dependence. It is unlikely that the accuracy required for the calibration ($< 0.1°$) can be reliably achieved using a Mueller formalism with a priori optical properties and geometry for a system this complex. Therefore, an empirical technique is used.

Polarization angles are modulo π; therefore, it is reasonable to assume the deviation of the ideal polarimeter response from linear can be represented with even harmonics, similar to a Fourier decomposition. In practice, the polarization response of the ALCATOR C-MOD MSE diagnostic is extremely well fit using an offset, a linear term, and the first two even harmonics in the following manner:

$$-\frac{1}{2}\tan^{-1}\left(\frac{I_{2\omega_1}}{I_{2\omega_2}}\right) = B_0 + B_1\theta_{pol} + B_2\cos(2\theta_{pol} + B_{2p}) + B_4\cos(4\theta_{pol} + B_{4p}) \quad (6)$$

with the coefficients B_x found empirically by fitting the detected intensities at the PEM harmonics to the known input polarization angle θ_{pol} from the polarization generation head. For physics reasons, $B_1 = 1$ is enforced, which is found to be consistent with the operation of the diagnostic.

Typically, the polarization head is used to illuminate the MSE objective lens from a MSE sightline viewing volume with a set of ~ 35 different polarization angles spanning $\sim 360°$. The ratio of the measured intensity ratios at each input polarization are fit to Equation 6, resulting in an rms residual fit error of $< 0.03°$. A sample data set is shown in Figure 13, where panel A shows the measured angle as a function of input polarization angle. Note that this is nearly, but not quite, a linear dependence. Panel B shows the residual after including only B_0 and $B_1 = 1$ in the fit with the $\cos(4\theta_{pol})$ structure evident.

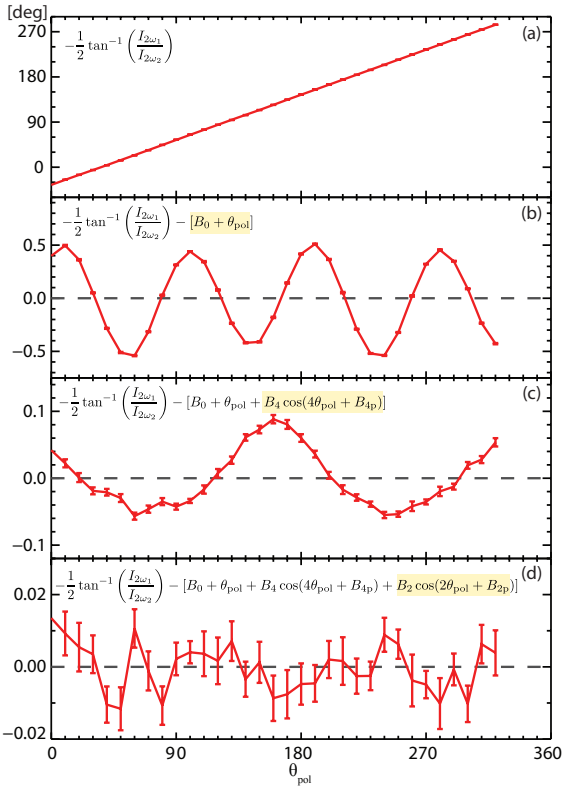

Figure 13: The fitting of the polarimeter polarization response. The measured polarization angle (a) contains non-linear response due to non-ideal components in the polarization response (b). Subtracting off the dominate $\cos(4\theta_{\mathrm{pol}})$ term leaves structure in the residuals (c). Including the first two even terms in the decomposition results in a small and structureless residual at the level of the uncertainty in the individual angle measurements (d).

Panel C shows the residual after fitting using an additional $\cos(4\theta_{\mathrm{pol}})$ term with remaining $\cos(2\theta_{\mathrm{pol}})$ structure evident. Panel D shows the residual after fitting the full calibration function, (Equation 6). Note that there is no longer any periodic structure in the residual above the level of individual angle statistical measurement uncertainty.

Increasing the number of angles measured, increasing the range of angles measured, or changing the order of polarization angles has no effect on the computed fit coefficients or the magnitude of the residual error. The fit continues to yield small residuals even in extreme cases, such as illuminating the MSE diagnostic with elliptically polarized light or operating MSE with non-optimized mirrors or non-equal PEM retardances.

Although the Fourier representation is used because it works empirically, the terms can be shown to arise due to physical polarization effects using the Mueller formalism and numerical simulation of the polarimeter and optical system. As shown in Table 1, the calibration system is repeatable to $0.04°$ after removal and re-installation of the robot components and is repeatable to $0.02°$ in successive calibrations without component removal. The MSE diagnostic polarization response drifts by $< 0.05°$ over 48 hours during tokamak maintenance periods when the tokamak is at atmospheric pressure and temperature. The automation, repeatability. and rapid action of the robotic calibration system allows the dependence of the MSE calibration on

Table 1: Variation of MSE calibration coefficients when the calibration system was used to calibrate the same MSE sightline on three different occasions. The calibration system was removed and re-installed between each trial. All values have units of degrees.

Trial	B_0	B_4	B_{4p}	B_2	B_{2p}	rms Residual
1st	−62.640	0.254	228	0.058	235	0.021
2nd	−62.623	0.327	223	0.058	238	0.013
3rd	−62.626	0.313	224	0.057	238	0.014
Stdev	0.009	0.039	3	0.001	2	
Max-Min	0.017	0.073	5	0.001	3	

various parameters to be studied in detail by performing repeated calibrations as some parameter of interest is varied.

The flexibility of the system allows the systematics in the diagnostic to be fully explored. For example, polarization calibrations can be performed repeatedly while changing the PEM retardance, the detector gains, or the filter wavelengths. The system can perform calibrations with parts of the diagnostic objective lens masked to determine the variability of the diagnostic response within a sightline. The laser source can be used to determine the diagnostic response along a single ray within a sightline or to examine the optics for vignetting. The system is accurate enough to monitor slight changes due to atmospheric temperature changes or from changing diagnostic components such as mirrors or the linear polarizer.

The use of fast digitization and numerical phased-locked loops in the MSE analysis allows the intensity at all the PEM harmonics ($I_{1\omega_j}$,$I_{2\omega_j}$...$I_{n\omega_j}$), to be precisely determined at each input polarization. This calculation is routinely performed on ALCATOR C-MOD for each plasma discharge and calibration shot[1]. Decomposing the detected intensity at a PEM harmonic as a function of input polarization angle into even Fourier components is also shown to capture the variability. Each of the n PEM harmonics are fit the equation:

$$\begin{aligned} I_{n\omega_{1,2}} &= C_0 + C_2\cos(2\theta_{pol} + C_{2p}) \\ &\quad + C_4\cos(4\theta_{pol} + C_{4p}) \end{aligned} \tag{7}$$

where C_2 is typically ~ 100 times larger than C_0 or C_4. A sample of this process is shown in Figure 14. Panel A shows the absolute value of the measured intensity at various PEM harmonics that have been normalized by $\sqrt{I_{2\omega_1}^2 + I_{2\omega_2}^2}$ averaged over all the input polarizations. The primary dependence is $\cos(2\theta_{pol})$, as seen by the small residuals in panel B after accounting for this term. This is expected from Equation 5. Note that the residual in the 1st (red, asterisks), 3rd (orange, triangle) and 4th (green, square) harmonics are at or below

1 Sets of mixed harmonics (i.e., $I_{3\omega_2-1\omega_1}$) are also calculated upon demand.

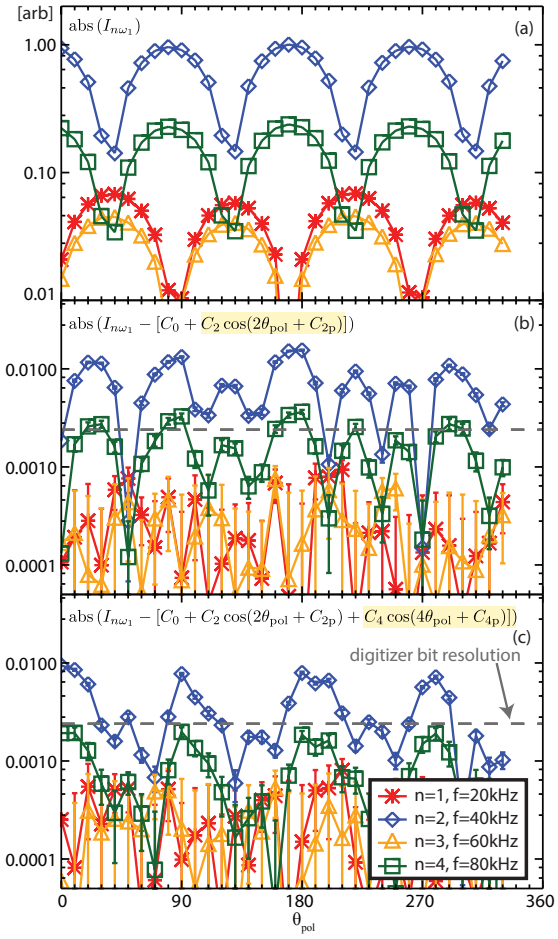

Figure 14: The fitting of the intensities at the first four PEM harmonics. The measured intensities at different PEM harmonics (a). All the intensities have been normalized by $\sqrt{I_{2\omega_1}^2 + I_{2\omega_2}^2}$ averaged over all the input polarizations. The residual after fitting the offset and term varying by $\cos(2\theta_{pol})$ (b). The residual after fitting all the terms in the Equation 7 (c). The digitizer bit resolution is shown as the grey dashed line.

the digitizer bit resolution (dark grey dashed line), while the 2nd harmonic (blue, diamond) remains above this level. Including all the terms in the Equation 7 results in a small, structureless residual (c) for all harmonics. The entire system response can therefore be accurately distilled into a table of coefficients, five per PEM harmonic.

2.8 CALIBRATION SOURCE MIS-ALIGNMENT

The accuracy of aligning the linear polarization angle relative to gravity and the quality of the polarized light produced by the polarization generation head have been discussed previously. However, errors in positioning the calibration head relative to the sightline can also cause errors in the polarization calibration. A projection effect is expected to skew the polarization angle if the calibration head linear polarizer is not perpendicular to the sightline. The robotic calibration system enables this conjecture to be tested by purposefully misaligning the normal of the linear polarizer on the polarization generation head relative to the mean $\vec{k}$ of the MSEsightline. The results of this study are shown in Figure 15. Note that this misalignment produces a change in the calibration offset coefficient, B_0, with a slope of 0.045 $^{\text{degree}}/_{\text{degree}}$

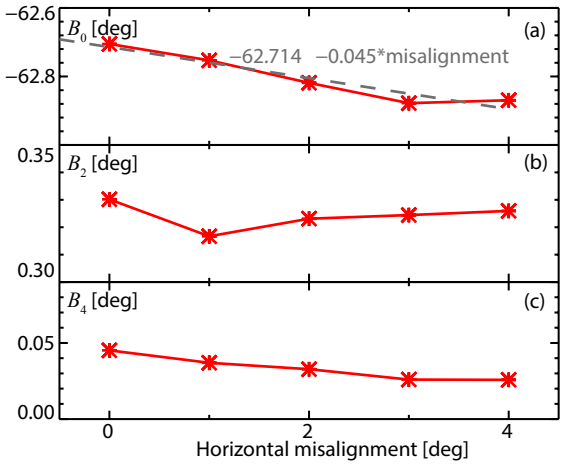

Figure 15: The polarization generation head was turned so that the polarizer was not normal to the MSE sightline and calibration cycles were performed. The resulting coefficients of the Fourier decomposition fit are shown.

for this geometry (a). There is little effect on the magnitude of the fit coefficient with the form $\cos(2\theta_{pol})$ (b) and a larger, though still small, effect on the coefficient with the form as $\cos(4\theta_{pol})$. If the center of the polarization generation head is not on the center of the sightline, but the normal is still parallel to the sightline $\vec{k}$, there is no measurable effect on the polarization calibration.

Prior to the development of the robotic calibration system, the linear polarizer in the light source was manually orientated to be perpendicular to the MSE slightline $\vec{k}$. This manual alignment was likely insufficient. The new robotic calibration system can easily obtain the required alignment tolerance of 0.5° to the sightline $\vec{k}$, resulting in a calibration error in B_0 of less than 0.022° due to this effect.

2.9 OTHER USES FOR THE ROBOTIC CALIBRATION SYSTEM

In addition to calibrating the MSE diagnostic in-situ, the robotic calibration system has also been used to perform calibrations of other invessel diagnostics, particularly the polarization transmission of the core CXRS diagnostic.

The calibration system has also been used to calibrate the PEM-based polarimeter on the bench. The PEM-based polarimeter assembly was removed from the MSE periscope and the polarization generation head was used to shine the laser source through the PEMs. It was coupled into the fibers in the fiber dissector, which transmitted it to the APD detectors. This geometry is illustrated in Figure 16. The position system was used to translate and rotate the PEM assembly to enable scans in the location of the laser's impact on the PEM surface and the angle of incidence of the laser through the PEMs, respectively. These investigations led to better understanding of the operation of the PEM-based polarimeter since there were no optical elements prior to the PEMs to modify the polarization of the light.

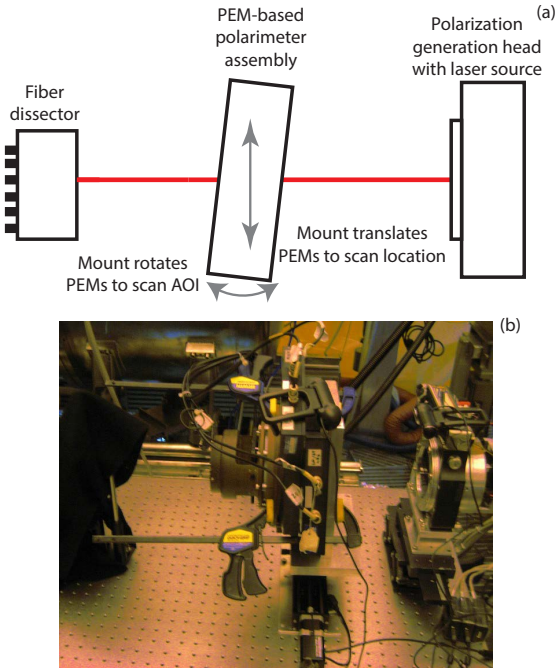

Figure 16: The PEM-based polarimeter was removed from the periscope to be calibrated with no optical elements in front of it. The polarization generation head inputs a laser through the PEMs and into the fiber dissector. The PEM assembly was rotated and translated by the positioning system to scan the measurement point across the PEM surface and to vary the angle of incidence, respectively (a). A photograph of the test (b).

In addition to the polarization generation head, several other components have been developed that can be mounted on the stage platform, including an integrating sphere to calibrate the spectral throughput of MSE and other beam based diagnostics; a bright unpolarized LED-based Lambertian source to calibrate the throughput of the MSE system; a movable slit to calibrate the viewing footprint of beam-based diagnostics; and a laser system to perform precision metrology inside the C-MOD vessel.

BIBLIOGRAPHY

[1] F. M. Levinton, G. M. Gammel, R. Kaita, H. W. Kugel, and D. W. Roberts. Magnetic field pitch angle diagnostic using the motional Stark effect (invited). *Review of Scientific Instruments*, 61(10):2914, 1990.

[2] M. F. Gu, C. T. Holcomb, R. J. Jayakuma, and S. L. Allen. Atomic models for the motional Stark effect diagnostic. *Journal of Physics B: Atomic, Molecular and Optical Physics*, 41(9):095701, May 2008.

[3] Howard Y. Yuh, F. M. Levinton, S. D. Scott, and J. Ko. Simulation of the motional Stark effect diagnostic gas-filled torus calibration. *Review of Scientific Instruments*, 79(10):10F523, 2008.

[4] R. S. Hemsworth, A. Tanga, and V. Antoni. Status of the ITER neutral beam injection system (invited). *Review of Scientific Instruments*, 79(2):02C109–02C109–5, February 2008.

[5] F. M. Levinton, S. H. Batha, M. Yamada, and M. C. Zarnstorff. q-profile measurements in the Tokamak Fusion Test Reactor. *Physics of Fluids B: Plasma Physics (1989-1993)*, 5(7):2554–2561, July 1993.

[6] F. M. Levinton, S. H. Batha, and M. C. Zarnstorff. Calibration of the upgraded motional Stark effect diagnostic on TFTR. *Review of Scientific Instruments*, 68(1):926, 1997.

[7] T. Fujita, H. Kuko, T. Sugie, N. Isei, and K. Ushigusa. Current profile measurements with motional Stark effect polarimeter in the JT-60U tokamak. *Fusion Engineering and Design*, 34-35:289–292, March 1997.

[8] J. Ko. *Current profile measurements using Motional Stark Effect on Alcator C-Mod*. PhD, Massachusetts Institute of Technology, 2009.

[9] M A Makowski, M. Brix, and N C Hawkes. Semi-Empirical Calibration Technique for the MSE Diagnostic on the JET and DIII-D Tokamaks. Heronsissos, Greece, June 2008.

[10] Yuejiang Shi. Improved signal analysis for the calibration of the motional Stark effect diagnostic. *Review of Scientific Instruments*, 77(2):023503, 2006.

[11] B. Shen, W.B. Xi, J.P. Qian, Y.W. Sun, and H.Y. Fan. The magnetic field configuration measurement on EAST tokamak. *Fusion Engineering and Design*, 84(1):19–23, January 2009.

[12] F. Piras, J.-M. Moret, and J.X. Rossel. Measurement of the magnetic field errors on TCV. *Fusion Engineering and Design*, 85(5):739–744, August 2010.

[13] Jl Pezzaniti and Ra Chipman. Linear-polarization uniformity measurements taken with an imaging polarimeter. *OPTICAL ENGINEERING*, 34(6):1569–1573, June 1995.

[14] D. Beals, R. Granetz, W. Cochran, W. Byford, W. Rowan, A. Ivanov, P. Deichuli, V. Kolmogorov, and G. Shulzhenko. Installation and operation of new long pulse DNB on Alcator C-Mod. In *21st IEEE/NPS Symposium on Fusion Engineering SOFE 05*, pages 1–4, Knoxville, TN, USA, September 2005.

3

DESIGN OF THE INTER-SHOT CALIBRATION (ISC) SYSTEM

The only significant time-varying systematic error found in the C-MOD MSE diagnostic periscope is due to birefringence in the various lenses and the vacuum window. The importance of birefringence was identified in previous work by Ko [1] as the cause of diagnostic response changes on the order of several degrees throughout experimental run day. This error is problematic primarily because it changes shot-to-shot in a manner that cannot be accounted for without a calibration taken very close in time to when the diagnostic is used.

An approach was devised to bridge the gap between highly accurate and flexible invessel robotic calibration during maintenance periods and sparse calibration using beam-into-gas or beam-into-plasma discharges during normal operation. This approach involved installing an in-situ calibration system to calibrate the diagnostic during and between discharges. This system is able to fill the diagnostic objective lens with linearly polarized light at any desired time, from operation in air to operation with plasma. The system can then be used to monitor changes to the diagnostic response with greater flexibility and accuracy than using plasma discharges. Since the in-situ system is designed to calibrate the diagnostic between discharges, it is termed the inter-shot calibration (ISC) system. There were several requirements which drove the design of the system:

1. The system must input polarized light into the periscope with a polarization angle known to better than 0.1°.
2. The system must be repeatable to better than 0.05° in polarization angle and to better than 1mm in illumination position.
3. The system must input two or more polarization angles, preferably from same location. These angles must bracket the range of polarization angles observed by the diagnostic (~ 15°) during operation. Four or more angles would be preferable to better capture the non-linear character of the diagnostic response.
4. The system must be able to simultaneously calibrate all ten MSE sightlines.
5. The system must illuminate the sightlines with an illumination pattern similar to that from the beam. This requires fully filling the diagnostic objective lens with light for all the sightlines.
6. The system must incorporate its own illumination source to allow it to operate without plasma. Plasma emission should not contaminate the illumination from the system.

7. The system must produce very high quality polarized light, including high linear polarization fractions (Degree of linear polarization, DOLP, > 0.9).
8. The system must be able to operate at any time, from atmospheric pressure to vacuum, with or without magnetic fields, and at all temperatures that the diagnostic experiences.
9. The system must be able to operate immediately before or after a plasma discharge, fully calibrating the diagnostic within two minutes of the discharge. It should be able to operate both before and after a discharge.
10. The system must be compatible with the environment inside the tokamak. It cannot degrade the vacuum and it must not be degraded by vacuum or plasma exposure. Plasma operation should not change the quality of the calibration due to coatings or erosion of the polarizing elements.
11. The system must reliably operate for $>$ 10000 calibrations (approximately four experimental campaigns) before requiring major servicing. It must survive worst-case C-MOD disruptions (200 G) without degrading the quality of the calibration.
12. Operation of the system should not interfere with other tokamak systems or diagnostics.
13. For practical reasons, it is preferable for the system to reside within the existing MSE envelope in the main tokamak vessel and to utilize only vacuum feedhtru ports currently used by MSE.

The requirement that the system be able to operate during a plasma discharge eliminates placing the system at the beamline. Furthermore, the requirement to fully calibrate all the sightlines while filling the entire objective lens with polarized light dictates that the system be installed immediately in front of the diagnostic objective lens rather than on a far wall. For robustness, it was decided to use multiple calibration sources to provide the different polarization angles instead of a rotating single calibration source that could change angle in a manner similar to the invessel robotic calibration system.

The inter-shot calibration (ISC) system is used to illuminate the diagnostic lens with known polarizations at any time—during maintenance, between shots, and during shots. The mechanical system rotates sources of polarized light that have very accurately known polarization angles (with respect to gravity) in front of the objective lens. This system can quickly calibrate the diagnostic, illuminating it with a full field of high-quality linearly polarized light within seconds of a plasma discharge. This system is the first of its kind designed to in-situ calibrate a MSE-LP diagnostic every plasma discharge.

By illuminating the objective lens, the system ensures that the entire diagnostic response is captured in the same manner as would be observed when using the neutral beam. This allows the ISC system to correct for a wide variety of possible diagnostic problems, including polarization aberrations in the periscope, the action of the PEMs, and the response of the detectors. The system inputs four different polarization angles sequentially over a period of ten seconds. The polarization angles are chosen to allow the diagnostic response to be interpolated across the range of polarization angles typically observed from the neutral beam. Additionally, the angles are also chosen to provide insight into what type of polarization aberration is causing changes to the diagnostic response.

The challenges in fielding such a system are predominately mechanical. The system must provide repeatable and accurate alignment of the polarizers and of the illumination in a reliable manner inside the tokamak vacuum within centimeters of the plasma edge. The necessary polarizer alignment repeatability of $< 0.05°$ requires great care to achieve.

3.1 SYSTEM OVERVIEW

Several different design concepts for the ISC system were considered, including fixed mirrors placed at the periphery and mirrors that translate in front of the diagnostic objective lens [1]. Instead, the decision was made to develop a mechanical "carousel"-based system. The primary component is a cylindrical carousel that rotates around the "turret" part of the MSE periscope on precision vacuum-compatible bushings. The carousel carries and mechanically aligns four different linear polarizers, each of which incorporates a component of the illumination system termed the "backlight scatterer." There is also an opening in the carousel that allows the objective lens to view the plasma. Remote LEDs couple light into optical fibers that carry it into the vessel to a custom ferrule that is rigidly mounted to the MSE turret. The ferrule contains optics which free-space couple the light into the edge of the aligned backlight scatterer and also optically detects when the carousel is in the correct position. The carousel is rotated about the turret by an actuation system outside the vessel operating via cable-in-conduit. The key components of ISC system are shown in Figure 17.

The design of this system configuration has three key advantages:

1. The system has only a single moving part inside the tokamak —the carousel—which can be very precisely are repeatedly mechanically positioned. The only movement is rotation on high precision bushings.

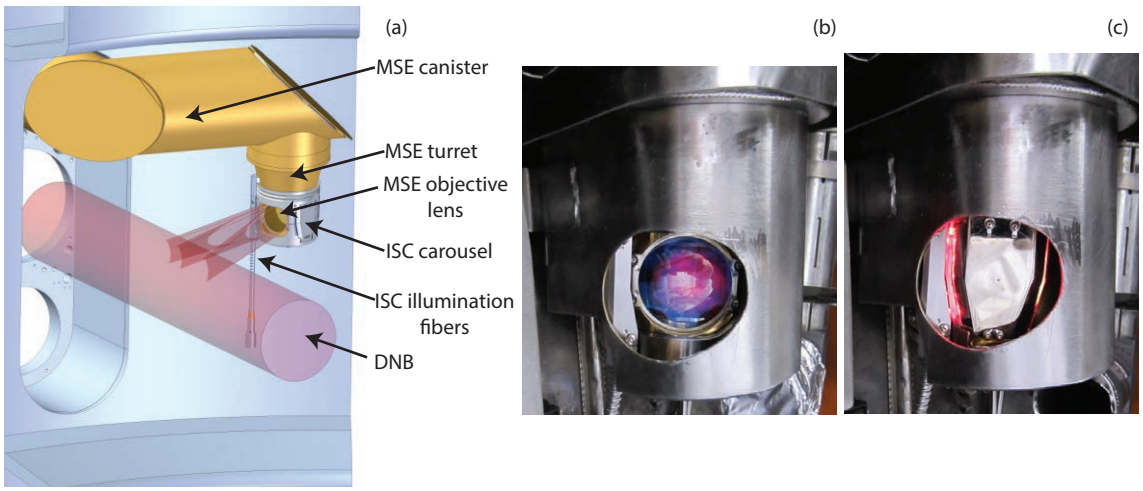

Figure 17: An overview of carousel-based ISC system. A carousel and a fiber optic-based illumination system are mounted on the MSE turret portion of the invessel periscope. The carousel rotates four different polarizers in front of the objective lens, which are illuminated by the illumination system (a). The system in the open position, allowing the objective lens to view the plasma (b). The system in one of the four calibration positions with the illumination system activated (c).

2. The system has its own illumination source—allowing it to be operated at any time, independent of light from the plasma or beam.
3. The system can fully illuminate the diagnostic objective lens with a flat field of calibration light as opposed to only illuminating a small portion of the lens. This allows it to capture any ray-dependent effects, providing an accurate calibration of the full diagnostic response.

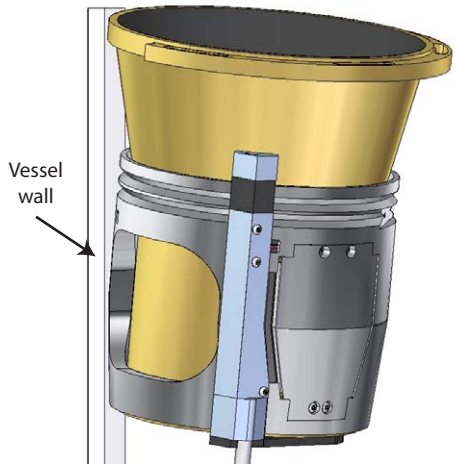

Figure 18: The tight spatial constraints around the ISC system, particularly between the carousel and the vessel wall.

The ISC system operates inside the tokamak and fits within the existing envelope of the MSE radiative heat shields. The development of this system was complicated by the harsh environment inside the tokamak, limited access, and tight spatial constraints. The clearances between the MSE turret and the vessel wall is very small, < 2cm, with a similar clearance between the turret and the heat shield. The carousel with the polarizers and backlight scatterers must therefore be thin and the ferrule must be small. Furthermore, there are only two < 20mm diameter vacuum ports available through which to operate the illumination and mechanical actuation subsystems. The turret was redesigned to accommodate the rotating bushing-based shutter prior to the installation of the ISC. The turret was strengthened and made as small as possible without interfering with the

MSE optical path and had bushing races incorporated during this redesign. The tight clearances are shown in Figure 18.

The temperature environment inside and around the tokamak is very harsh. The invessel components are subject to $> 50°C$ temperature swings due to flash heating by the plasma discharges. Meanwhile, the vacuum ports can reach cryogenic temperatures. The components must be able to expand and contract with these temperature changes while still maintaining the necessary alignment of the polarizers and integrity of the vacuum seals. Additionally, the mechanical components must be able to move in these temperature and vacuum conditions. Furthermore, the tokamak has a very high-quality vacuum that cannot be contaminated by the ISC components, placing constraints on what materials can be used.

The internal components are subject to large electromagnetic forces during disruptions. The orientation of the carousel makes this component especially prone to large disruption torques due to the interaction between the eddy currents circulating in the carousel and the tokamak toroidal field. The ISC components are therefore fabricated from Inconel, which has a lower conductivity and higher strength than stainless steels. Finite element analysis was conducted to quantify the disruption forces and verify that the ISC components and MSE periscope would survive repeated C-MOD disruptions. The eddy currents also cause large voltages to develop between components, thus electrical conduction paths are carefully incorporated to prevent arcing without increasing eddy currents.

3.2 CALIBRATION CAROUSEL WITH POLARIZERS

The main component in the ISC is the calibration carousel. This component, the only moving part, carries and mechanically aligns the polarizers in front of the diagnostic. The carousel construction is shown in Figure 19. The carousel surrounds the turret portion of the MSE periscope, which contains and aligns the objective lens (L1) and the first mirror (M1). The carousel is an Inconel cylinder, approximately 8.5mm thick and 100mm tall, and is slightly conical due to the tight clearances between the vessel and the MSE turret. The carousel, machined from a single piece of Inconel, has five large openings cut into its circumference. One opening enables the diagnostic to view the plasma through the carousel. The remaining four openings are designed to hold and precisely align linear polarizers and backlight scatterers.

The linear polarizers are 0.7mm thick vacuum-compatible wire grid polarizers (WGPS). These consist of a series of very fine, < 100nm thick, regularly spaced parallel wires deposited on a BK7 substrate[1]. The WGPS act as polarizers in transmission, have a spatially uniform trans-

1 Manufactured by Moxtek.

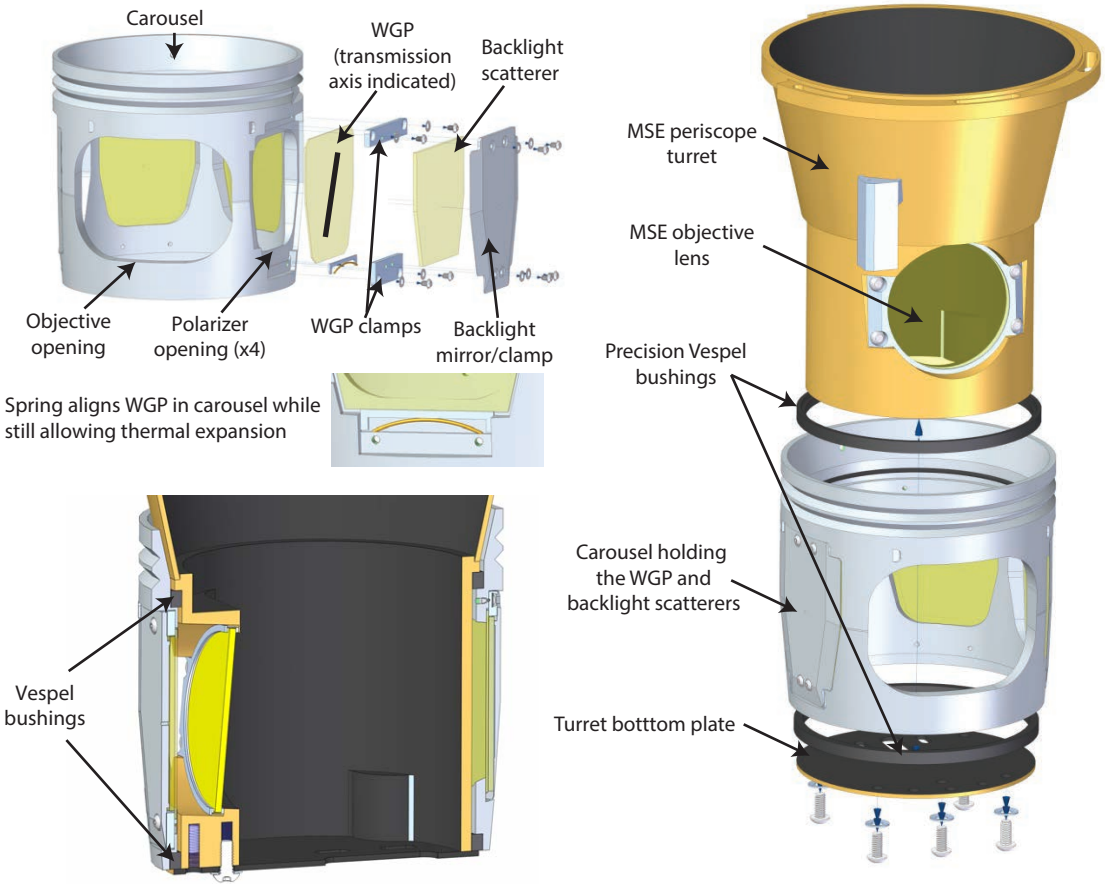

Figure 19: The ISC carousel construction. The carousel has one opening to allow the diagnostic to view the plasma and four openings to hold calibration sources. Each of these four openings contains a wire grid polarizer (WGP) acting in transmission. The polarizers are aligned in Teflon coated frames machined into the carousel using springs to allow for differential thermal expansion. Each WGP is backed by a backlight scatterer which is held in place with a mirror/clamp. The carousel rotates around the MSE turret on two precision Vespel bushings with well-controlled running clearances. When in calibrating position, the WGP is placed directly in front of the diagnostic objective lens.

mission axis angle, a large allowable viewing angle, and a contrast ratio > 800. The side of the WGP with the wires deposited on it, which does the polarizing, is positioned inward—toward the lens—to prevent Faraday rotation in the substrate from affecting the polarization angle of the light. These components are very fragile can can be easily damaged, so care must be taken in their use and handling. The WGPs are held lightly in Teflon coated frames in the carousel using Teflon coated clamps. Pressure is applied to the bottom of each WGP by a spring, pushing the top edge of the WGP against the top edge of the frame in which it sits. This allows for differential expansion between the WGP and the carousel while still maintaining the polarizer alignment relative to the carousel. The orientation of the WGP transmission axis relative to its top edge is carefully specified. This ensures the desired polarization angle relative to gravity is input when the WGP is placed in front of the objective lens.

A backlight scatterer is placed on the outside of each WGP. The 1.6mm thick BK7 backlight scatterer accepts light from its thin vertical edge and is textured to scatter this light uniformly into the objective lens. This process is discussed further in the next section. The backlight scatterer is held in place with a clamp that protects it and acts as mirror to enhance the light scattered into the objective lens. This element also prevents plasma emission from penetrating the calibration system, allowing the system to be used during plasma discharges without plasma light leakage, which may skew the result.

The WGP and backlight scatterer are sized so that they nearly fill the entire étendue observed by the diagnostic as shown in Figure 20. This results in a clearance of $\sim$ 1.5mm between the WGP and the outer surface of the turret. The filling of the sightlines recreates the illumination pattern from the beam and plasma, enabling the ISC to capture the correct diagnostic response. A smaller illumination pattern or the use of only a few calibration rays would only sample a subset of the diagnostic response.

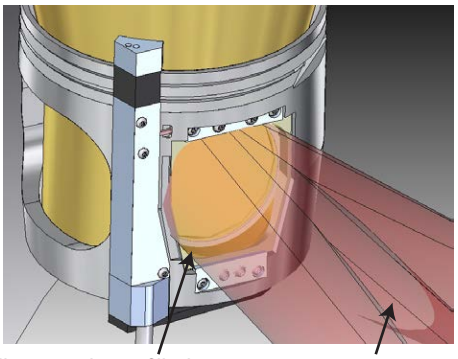

Figure 20: The ISC WGP and backlight scatterers nearly fill the entire objective lens of the diagnostic. View cones for sightlines at the optical axis and field extents are shown.

The carousel is mounted onto the MSE turret using two precision-machined Vespel bushings. Vespel is a vacuum-compatible, high-strength, low-creep, low-outgassing, low-friction, high-temperature, very expensive, engineered plastic used in the aerospace industry[2]. The high-dimensional stability and strength of the plastic allows complex, tight tolerance components to be fabricated. The plastic has low friction when sliding on steels in vacuum—lower than in air—making it ideal for mechanical appli-

2 Vespel SP3, manufactured by Dupont was used. See material specifications located at Dupont's website.

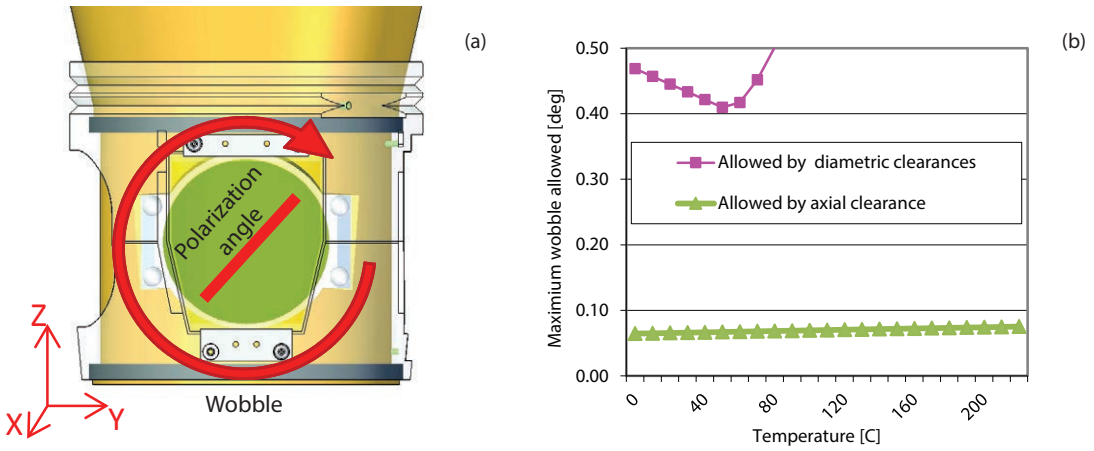

Figure 21: The ISC carousel "wobble" affects the polarization angle from the WGP relative to gravity (a). The wobble is controlled using tight bushing running clearances in the axial (z) direction. The dimensions of the components are chosen to provide a constant axial running clearance, and therefore allowed wobble, as a function of bulk temperature (b). The bushings are apparent inside the carousel which is rendered transparently.

cations in vacuum. The plastic is used in high precision mechanical movement systems inside the beamline of the Large Hadron Collider and in space applications. The out-gassing properties of the plastic were tested and found to be compatible with the C-MOD vacuum requirements. The two bushings ride on precision-machined races on the inside of the ISC carousel and on the outside of the MSE turret. The carousel and bushings are installed over the turret from the bottom and held by a bottom plate that also supports the adjustable M1 mirror mount inside the turret.

The amount that the WGP transmission axis can change relative to gravity depends on the degrees of freedom (DOF) of the carousel relative to the MSE turret. The most important of these DOF is the rotation of the carousel about the axis of the objective lens, termed here the "wobble." The situation is shown schematically in Figure 21. In this figure, wobble corresponds to allowing the carousel to rotate about the x-axis. If the carousel is allowed to wobble, this will directly rotate the transmission axis of the WGP, leading to improper calibration. The carousel and bushings are therefore designed to minimize wobble while still allowing the carousel to rotate about its axis (the z-axis in Figure 21).

There are three running clearances in the bushing system. The axial clearance (i.e., how much the carousel can translate along the z-axis) is set by the distance between bushing races on the turret and carousel and the thickness of the bushings in the vertical direction. The two diametric clearances (i.e, how much the carousel can translate along the x- and y-axes) are set by the outer diameter of the bushings and inner diameter of the carousel and by the outer diameter of the turret and inner diameters of the bushings.

Table 2: How each ISC DOF is controlled.

DOF	Constrained by	Allowed movement
X,Y translation	Diametric clearance	0.25mm
Z translation	Axial clearance	< 0.2mm
Rotation about X,Y (wobble)	Axial clearance	$< 0.07°$
Rotation about Z	Actuator	$< 1°$

The wobble is controlled by running very tight, < 0.2mm, axial clearances. This prevents the turret from rotating about the x- and y-axes because such a rotation would cause a compression of one side of the bushings in the axial direction. The tight axial clearance results in an allowed wobble of $< 0.07°$. The final axial clearance is tuned using 0.02mm shims between the turret and the turret bottom plate. Additionally, the carousel is pulled slightly downward against the bushings by the actuation system to provide a consistent bushing sliding surface, limiting the wobble in practice. The only remaining rotation DOF is about the z-axis—the polarization angle of the WGP is much less sensitive to this angular rotation—is controlled by the actuator system. How each of the six DOFs is controlled is listed in Table 2.

Vespel (bushings), stainless steel (turret), and Inconel (carousel) all have different coefficients of thermal expansion. The running clearances are therefore temperature dependent. This is mitigated for the axial clearance by choosing the axial thickness of the bushings such that the thermal expansion of the combined carousel and bushings equals the thermal expansion between the bushing races on the turret. This results in the axial running clearance—and therefore allowed wobble—being nearly independent of bulk changes in temperature, as shown in Figure 21. Bulk temperature changes result in much larger changes in the diametric clearances; the sliding interface shifts from being between the bushing outer diameter and the carousel race inner diameter at low temperatures to being between the bushing inner diameter and the turret outer diameter at higher temperatures.

The basic design of the carousel-bushing system was developed prior to the ISC system as part of an upgraded, more robust MSE shutter. The tight clearances Vespel bushing concept was tested inside a vacuum test chamber using push-pull feedthrus acting via cable-in-conduit. The system was cycled over 18000 times (approximately equivalent to six C-MOD campaigns) at various temperatures from room temperature to 200°C and from atmospheric pressure to vacuum during this test. The force required to rotate the system was monitored and found to decrease at high temperatures and to remain unchanged with increasing cycles. Subsequent disassembly found very little evidence of wear in the bushings and the races. The torque required to rotate the actual ISC hardware was tested in air at

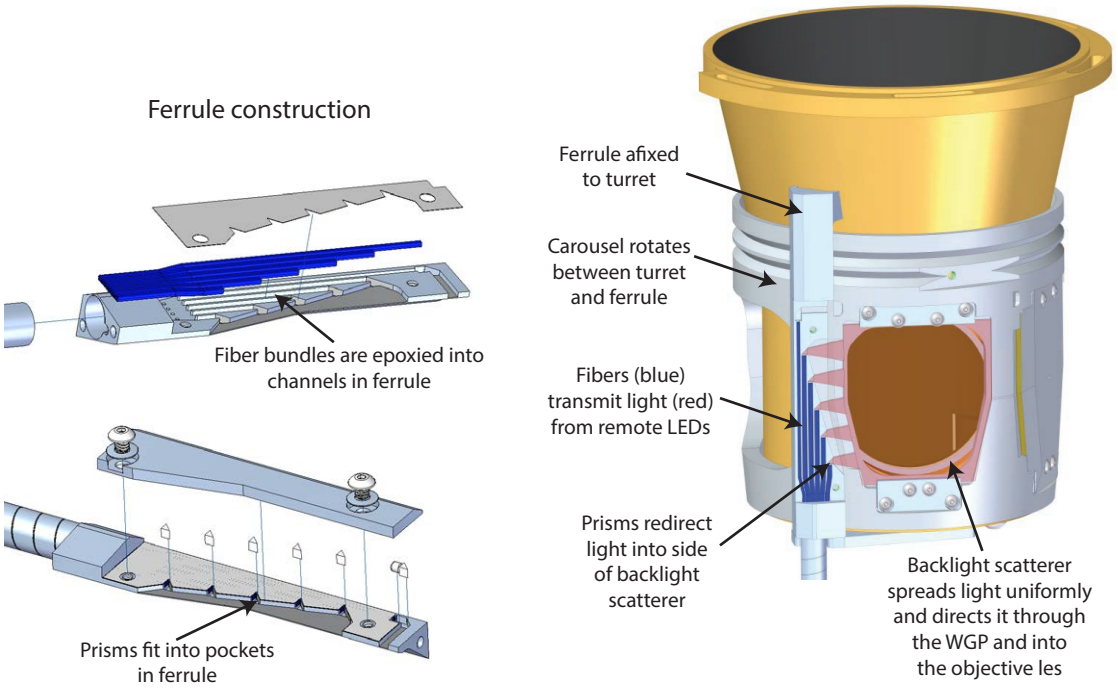

Figure 22: The ISC illumination system. The fibers are epoxied into a ferrule that also includes 2mm prisms that redirect the light into the side of the backlight scatterer placed behind the WGP. The scatterer then redirects the light into the objective lens in a uniform fashion.

different temperatures and found to be temperature independent, indicating the axial clearance was behaving according to expectations.

3.3 ILLUMINATION SYSTEM

A fiber optic-based system was developed to illuminate the WGPs after they are rotated in front of the diagnostic objective lens. This system transmits light from remote red LEDs[3] through 15m long fibers, through a 20mm inner diameter vacuum flange, to the MSE turret. The fiber terminates in a ferrule that redirects the light into the backlight scatterer placed behind the WGP, where it is scattered into the objective lens. The construction of the system is shown in Figure 22.

The fibers consist of five bundles, each with six fibers, with each bundle coupled to an LED. The fibers are epoxied into channels in the ferrule that lead to pockets containing 2mm prisms that redirect the light 90°. The surfaces of the ferrule are polished to help couple the light into the backlight scatterer. The Inconel ferrule is rigidly attached to the MSE turret, and the carousel rotates between the ferrule and the turret. The alignment is carefully arranged so that the light is properly directed into the side of the backlight scatterer.

3 Spectrum centered at 660nm, 20nm FWHM, Tholabs part M660L3 mounted LED, 640mW

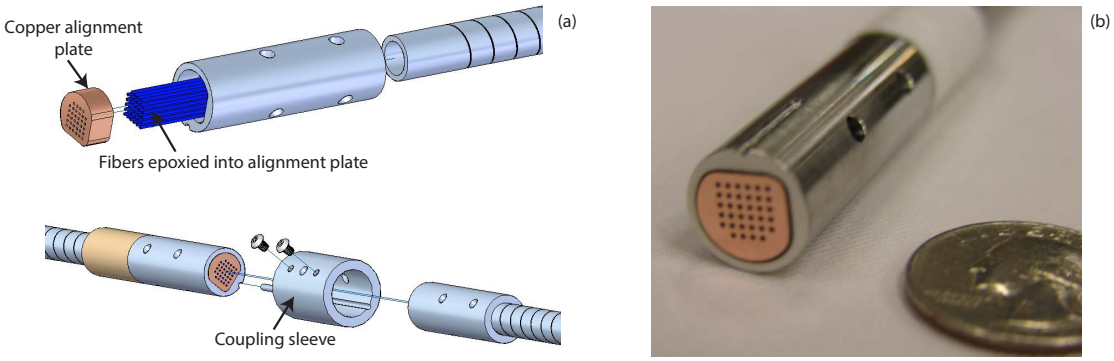

Figure 23: The fiber optic coupler used in the ISC system. Fibers are epoxied into different pieces of a copper alignment plate that was fabricated as a single piece. The alignment plate is keyed into coupler ends that are then mated together, reuniting the alignment plates and mating the fibers in butt joints.

One key innovation in the design of the illumination system is the manner in which the fibers are brought into the vessel. The small vacuum port combined with the requirement to tune the scattering on the bench required a break in the fibers inside the vacuum vessel and a small fiber optic connector. A novel design was developed to simultaneously connect the 34 fibers (5 bundles of 6 fibers for illumination and a bundle of 4 fibers for an alignment technique that was ultimately not used) using a single 20mm diameter coupler, shown in Figure 23. A copper alignment piece was fabricated with individual holes drilled for each of the fibers. Four alignment plates were made by subdividing this component perpendicular to the fiber direction, ensuring that the holes would align when the plates were brought back together. The fibers are epoxied into the alignment plates that are keyed and mounted in stainless steel coupling pieces. These pieces are then pin aligned together inside the vacuum vessel. When this assembly is completed, all the fibers aligned into butt joints. Transmission measurements indicate this is a reliable method to couple many fibers together with acceptable losses.

When the carousel is brought into proper alignment with the ferrule, light is coupled into the backlight scatterer across the $\sim$ 3mm gap between the ferrule and the edge of the backlight scatterer. The backlight scatterer is fabricated from a piece of glass in which the light travels inside via total internal reflection. The WGP-facing surface is sandblasted, presenting scattering centers that scatter some of the light out of the glass, through the WGP, and into the diagnostic. This mechanism works in a similar manner as a LCD monitor; light from a source on the side of the monitor enters the thin side of a medium that then, using scattering centers, directs the light out of the planar side. The process and photographs are shown in Figure 24. Various concepts were developed to efficiently scatter the light into the diagnostic objective lens, including gold coating the non-sandblasted side of the backlight scatter to create a mirror surface and placing reflec-

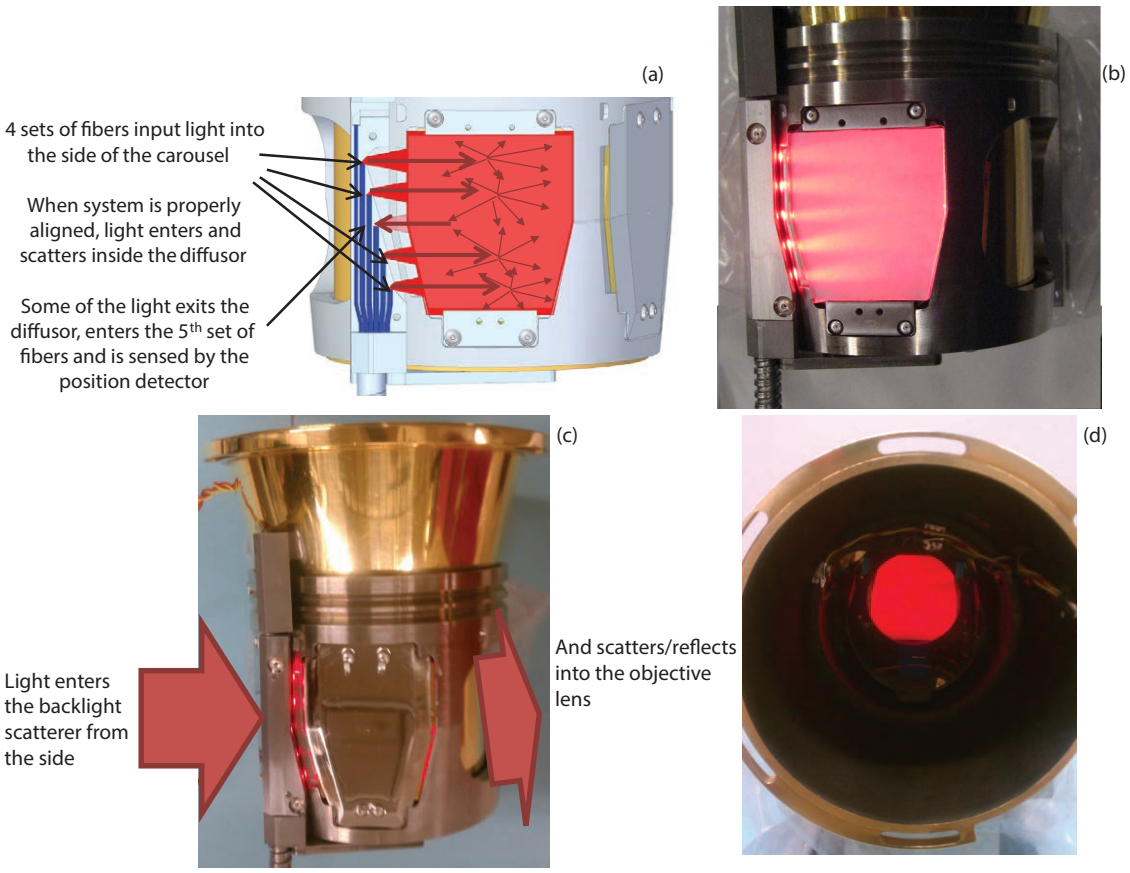

Figure 24: Scattering from inside the backlight scatterer is used to couple the light from the remote LEDs into the diagnostic objective lens. One bundle of fibers is used as both a source of light and a detector of scattering (a). An illuminated backlight scatterer with the mirror/clamp removed illustrates the concept (b). The fully assembled system seen from outside (c) and the illuminated WGP surface seen from "upstream" of the MSE turret via reflection from M1 (d).

tors around the edges of the backlight scatterer to create extra passes inside the medium. In practice, the scattering efficiency is low—only a small percentage of the light is directed into the objective lens. However, this is compensated by using high power LEDs.

The uniformity of the illumination is important. A flat field of illumination is desired to properly capture the diagnostic response. Significant effort was spent to produce uniform illumination from each backlight scatterer. The up-down uniformity is tuned by changing the coupling efficiency of the five different LEDs into the five fiber bundles. The uniformity in the horizontal direction is tuned by carefully prescribing the sandblasting and reflection surfaces on the backlight scatterer.

A procedure was developed to test the uniformity of the backlight scatterers and to tune the sandblasting on the bench. The MSE turret with the installed ISC is mounted to a computer-controlled camera observing the ISC uniformity from "upstream" of the MSE turret via the M1 mirror. A patch fiber, which is identical to the fiber installed in the tokamak and cell (but much shorter) is used to transport the

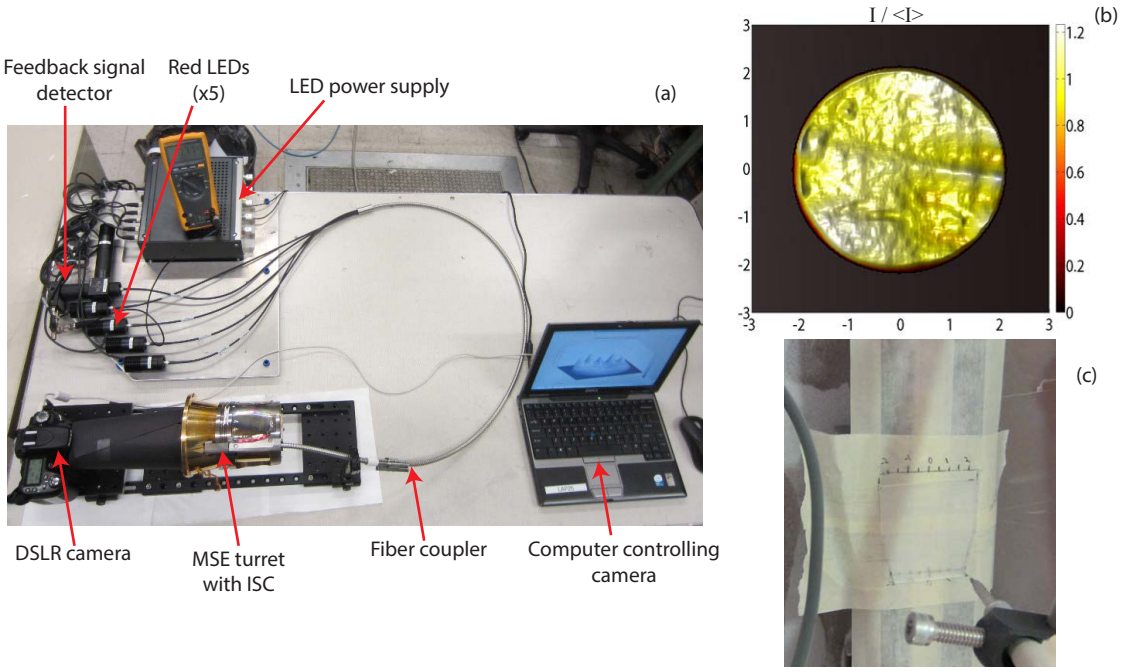

Figure 25: A technique was developed to tune the uniformity of the ISC illumination by varying the sandblasting of the backlight scatterers. The MSE turret with ISC system is mounted to a computer-controlled camera that photographs the ISC via the M1 mirror. A patch fiber is used to couple the light from the high power LEDs into the ferrule (a). The uniformity of the illumination is then calculated from the photographs (b). Necessary changes are made to the backlight scatterer using controlled sandblasting of the backlight scatterer (c).

light from the high power LEDs to the ferrule. Photographs are taken of the ISC and a map of its uniformity is calculated. Corrections to the backlight scatterer are then made by carefully sandblasting it to add more scattering centers using a custom sandblasting rig. The process is shown in Figure 25. This process is repeated until the desired uniformity is obtained for each backlight scatterer. In practice, the uniformity of the illumination measured as standard deviation divided by mean is 0.1 to 0.2. The spectrum of the individual LEDs was checked to confirm they are all very similar, thus the illumination field remains flat even when filtered with narrow bandpass filters. The backlight scatterer is not completely Lambertian, there is significantly more spatial uniformity than directional uniformity due to the fact that the light is input from one side. The implication is that different MSE sightlines observe different intensities but each observes a spatially uniform source, thus equally sampling the rays within a sightline.

In addition to the uniformity of the illumination, the polarization properties of the light from the ISC are also important. This was investigated using the polarization-sensitive camera detailed in Reference [2]. The camera was placed upstream of the MSE turret and imaged the ISC source via the M1 mirror and the objective lens. The results of this investigation are shown in Figure 26. The polarization of a single

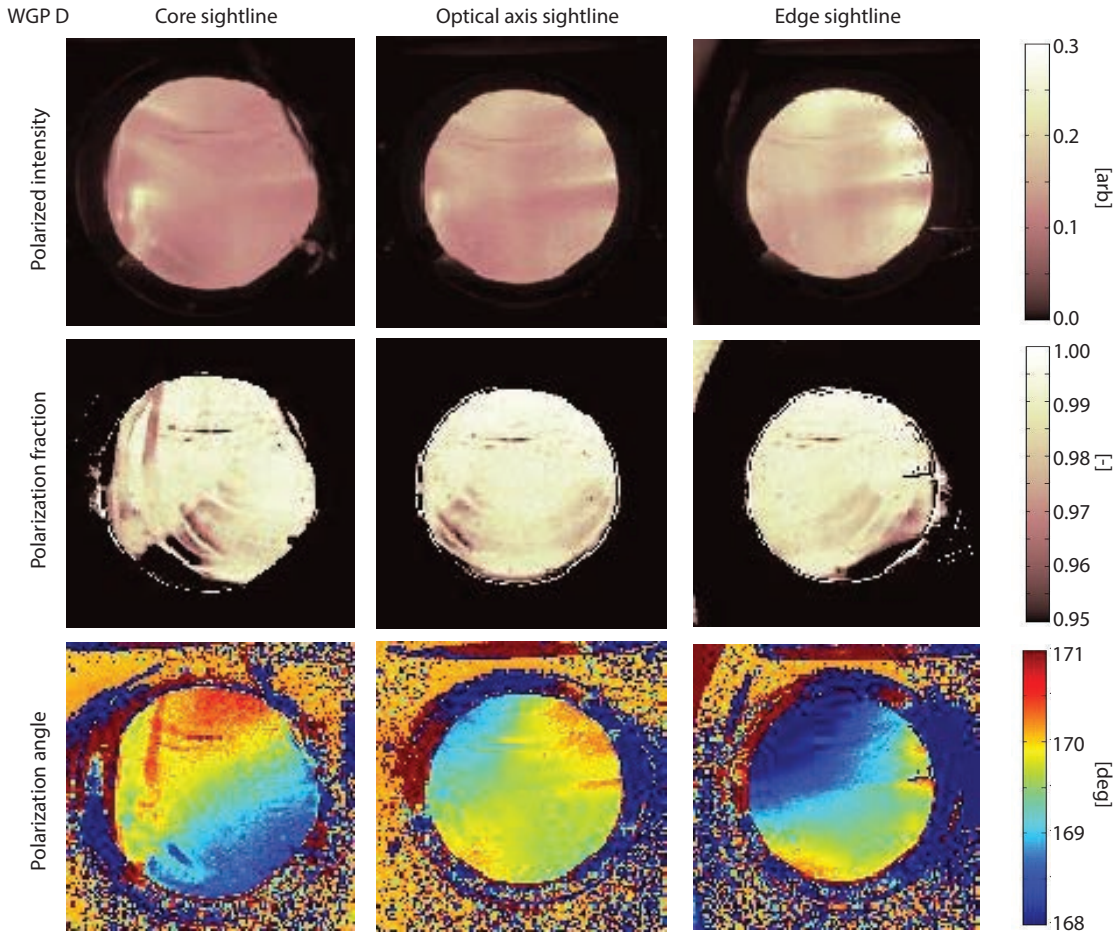

Figure 26: Photos of the ISC illumination taken with the polarization-sensitive camera. The camera was placed upstream of the MSE turret, viewing the ISC via the M1 mirror and the L1 lens. The polarized intensity (top row), polarization fraction (middle row), and polarization angle (bottom row) of WGP D is shown. The camera was moved to approximate the view of the ISC from a MSE sightline on the optical axis (center column), a core-viewing sightline (left column), and a edge-viewing sightline (right column). Note: the polarization angle is not referenced relative to the tokamak frame but is consistent among the columns.

WGP is shown, though the other other three have very similar properties. The view of the ISC from sightlines that view the tokamak core (left), on the MSE optical axis (center), and the tokamak edge (right) are shown. Note that the polarization angle from the ISC is fairly constant across the surface ($\sim 1°$ on the optical axis) for each view, with larger variability when viewed from off the optical axis. The polarization fraction is very high, > 0.95, and the polarized intensity is fairly uniform. This indicates the ISC system delivers high-quality polarized light into the diagnostic objective.

3.4 ACTUATION SYSTEM

The carousel is rotated around the turret using a cable-in-conduit system similar to the operation of a bicycle brake-cable. Two cables are

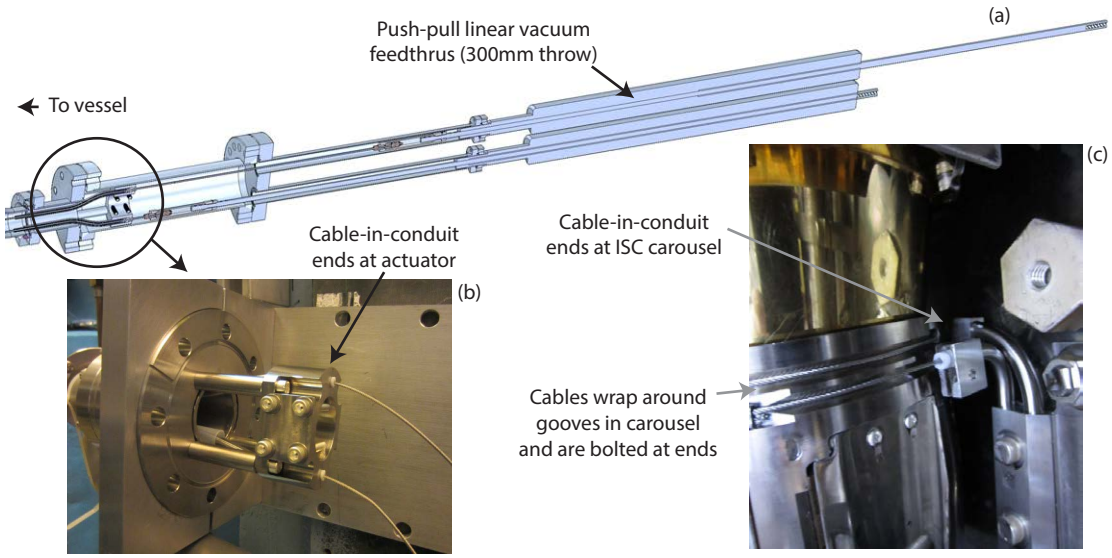

Figure 27: The ISC cable-in-conduit actuation system. Two cables wrap around and are attached to the top of the carousel (c). The cables enter Teflon-lined guide tubes that lead them out of the main vacuum vessel via a small port. The tubes then terminate in a secondary vacuum chamber (b) where the other end of the cables are attached to linear push-pull bellows-based vacuum feedthrus (a).

bolted to the top of the carousel and wrap around the circumference in grooves. The cables then each enter a stainless steel Teflon-sheaved tube. These two 3m long tubes curve along the vessel wall from the MSE turret location to the F-port flange, where they travel through a small vacuum tube-and-bellows system to the outside of the tokamak bio-shield. The guide tubes then terminate inside a larger vacuum assembly, upon which bellows-based push-pull linear vacuum feedthrus are mounted. Each cable end is attached to the vacuum end of each feedthru with a turnbuckle that allows the length of the cable to be adjusted and acts as an electrical break (the entire cable remains at the potential of the carousel). The cable-in-conduit system is shown in Figure 27. Moving the air-side of the vacuum feedthru therefore pulls the cable relative to the guide tube. This remotely applies torque to the carousel, rotating it, with the two cables rotating the carousel in opposite directions.

The positions of the linear push-pull vacuum feedthrus are controlled on the air-side using two 300mm long lead screw-based linear motors. These use stepper-motors wired anti-parallel—when one moves forward the other moves backwards the same amount. This ensures that the motors both work together to pull one cable while letting out the other cable to keep a constant amount of tension—and prevent binding—in the long, winding, cable-in-conduit path. The push-pull feedthrus are attached to the moving part of the motors using magnetic couplers with a maximum pull force of 100N, limiting the amount of tension that can be placed on the cable inside the vacuum. A strain gauge-based load cell is also attached to the push-

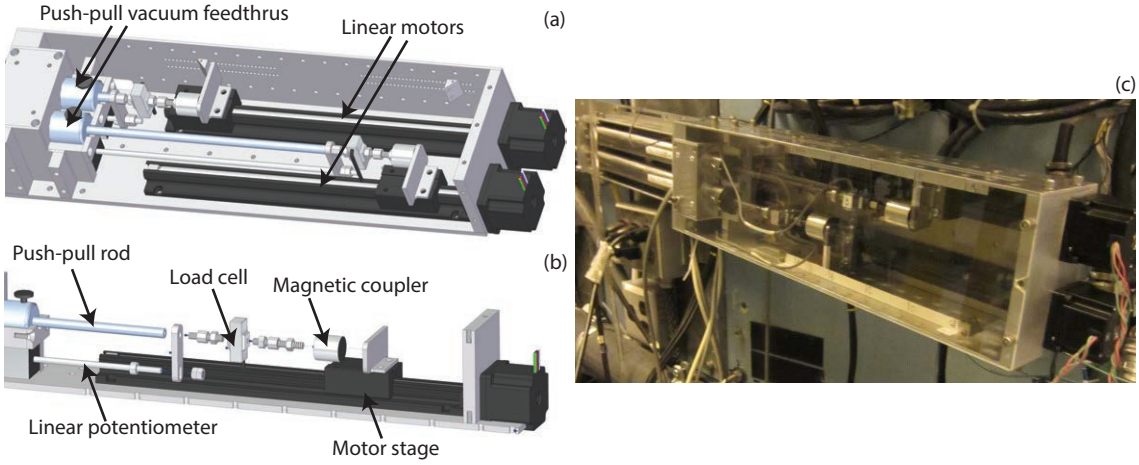

Figure 28: The ISC actuator system. Two linear motors act to push and pull the linear vacuum feedthrus (a). Each feedthrough is attached to the linear motor using a load-cell and a magnetic coupler to measure and limit the amount of force applied to the cable-in-conduit system, respectively. A high precision linear potentiometer is attached to each feedthru end to encode the position of the feedthru (b). The entire system, along with the vacuum hardware, is attached to the outside of the C-MOD bio-shield blocks (c).

pull end to measure the pull and push force that is being applied to each feedthru. Each feedhtru end is attached to a high precision linear potentiometer that accurately encodes the position of the feedthru. The position of the feedthrus can be very precisely measured and controlled to ~ 0.1mm, corresponding to $\sim 0.1°$ of rotation of the carousel. The external actuation system is shown in Figure 28.

3.5 OPERATION

Photographs of the assembled and installed ISC system are shown in Figure 29.

A non-contact method was desired to determine when the WGP is properly rotated in front of the objective lens by the actuator system. This is done optically by observing the backlight scatterer. The middle of the five fiber bundles used for illuminating the backlight scatterer has a both an LED and photodiode mounted on the air-side end of the fiber optics, separated by a half-silvered mirror. The LED remains off while the carousel is rotated by the actuator. When in proper alignment, light from the other four LEDs enters the backlight diffuser and some of it is reflected back toward the ferrule. This reflected light is coupled into the middle fiber bundle, transported out of the vessel, and is detected by the photodiode. The process is shown in Figure 24 panel A. This provides a sensitive means to determine when the WGP is in the proper position in front of the objective lens. The feedback signal as a function of the ISC vacuum feedthru position is shown in Figure 30. This system can locate the rotation of the carousel about the turret to $< 1°$.

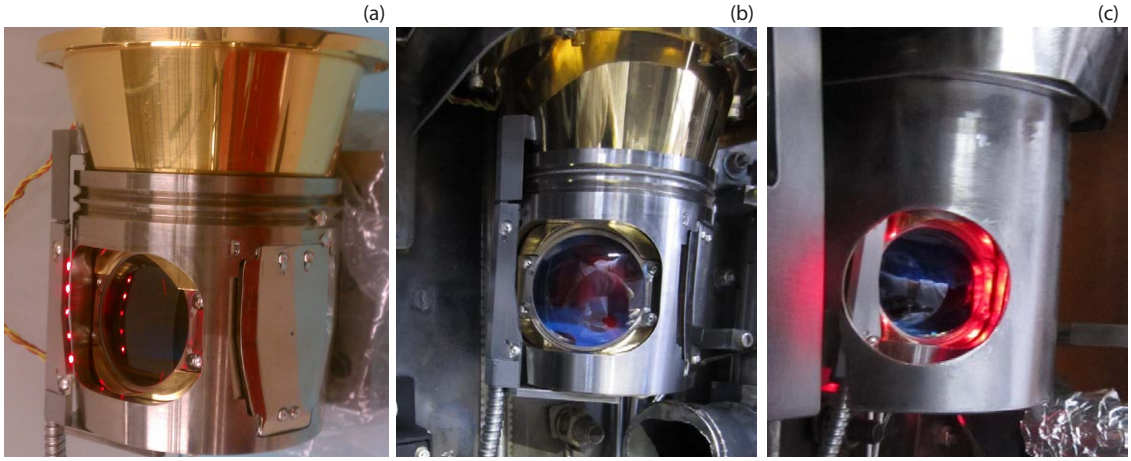

Figure 29: Photographs of the ISC system assembled on the bench (a), installed on the MSE system (b), and with the heat shield installed (c).

Figure 30: The reflected signal from the backlight scatterer measured by the middle fiber bundle indicating when each of the four WGPs is in the proper position in front of the MSE objective lens (a). The position of the vacuum feedthru as measured by the potentiometer (b).

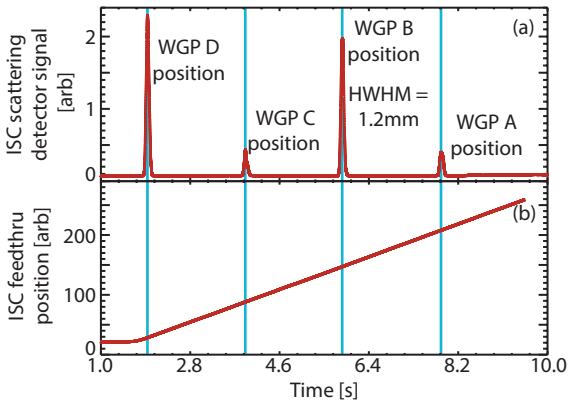

The actuation and illumination system is computer controlled by a MATLAB routine that interfaces with the MDSPLUS database and is triggered by the C-MOD shot cycle. This computer control activates the linear motors, controlling their position, velocity, and acceleration to move the carousel to the desired location using signals from the scattering feedback detector and the linear potentiometers. It is found that the proper alignment of the carousel occurs at a very repeatable position of the vacuum feedthru. The system is therefore controlled in a feed-forward manner, though feed-back control using the scattering sensor is possible. Care is taken to always approach the desired position from the same direction to eliminate any errors due to slop in the cable-in-conduit system. Tests show that this positioning methodology is capable of positioning the rotation of the carousel to 0.5°.

The ISC system is used immediately after a plasma discharge[4]. The MSE digitizers run for 11.5s to record the data from the ISC system in the same data file as the data from the plasma. The fast actuation of the system serves two purposes; first, the calibration data is taken close in time to the plasma data and, second, the use of a single data file simplifies bookkeeping and analysis. The signals from the ISC scattering detector, the actuator linear potentiometers, and the load cells are recorded on the same digitizer as the MSE signals.

A typical shot cycle is shown in Figure 31. The scattering detector signal is shown in panel A and the feedthru position is shown in panel B. The plasma discharge occurs from 0 to 2s, indicated by the red-shaded region. The actuator starts to move the carousel once the plasma has ended and the toroidal field has ramped down (blue trace in panel B). The system pauses at the peak of the scattering detector signal for each carousel position, at which point the LED that shares the scattering feedback fiber is illuminated, saturating the detector. The actuator moves the carousel to the next position after a brief $\sim$ 0.5s pause for measurement, shown in blue shading. The polarized light intensity and angle measured by a MSE sightline are shown in panels C and D, respectively. The polarized light intensity peaks and the fluctuations in the polarization angle decrease when the ISC is in position. The partially polarized plasma emission is also apparent along with a single DNB pulse, highlighted in green. The intensity of the polarized light from the ISC is significantly brighter than that from the beam for this discharge with this ISC configuration (later iterations decreased the ISC brightness to increase uniformity). Three of the measured polarization angles of the WGPS are near the polarization angle from the DNB while the fourth angle is $\sim 90°$ separated to account for the character of systematic errors which are either modulo $\pi/2$ or modulo $\pi/4$. The polarization angle during one of the ISC measurement is shown with an expanded time scale in panel E. Note

4 The system could be used prior to the discharge but current limitations of the C-MOD timing system prevent this from being done with accurate timing.

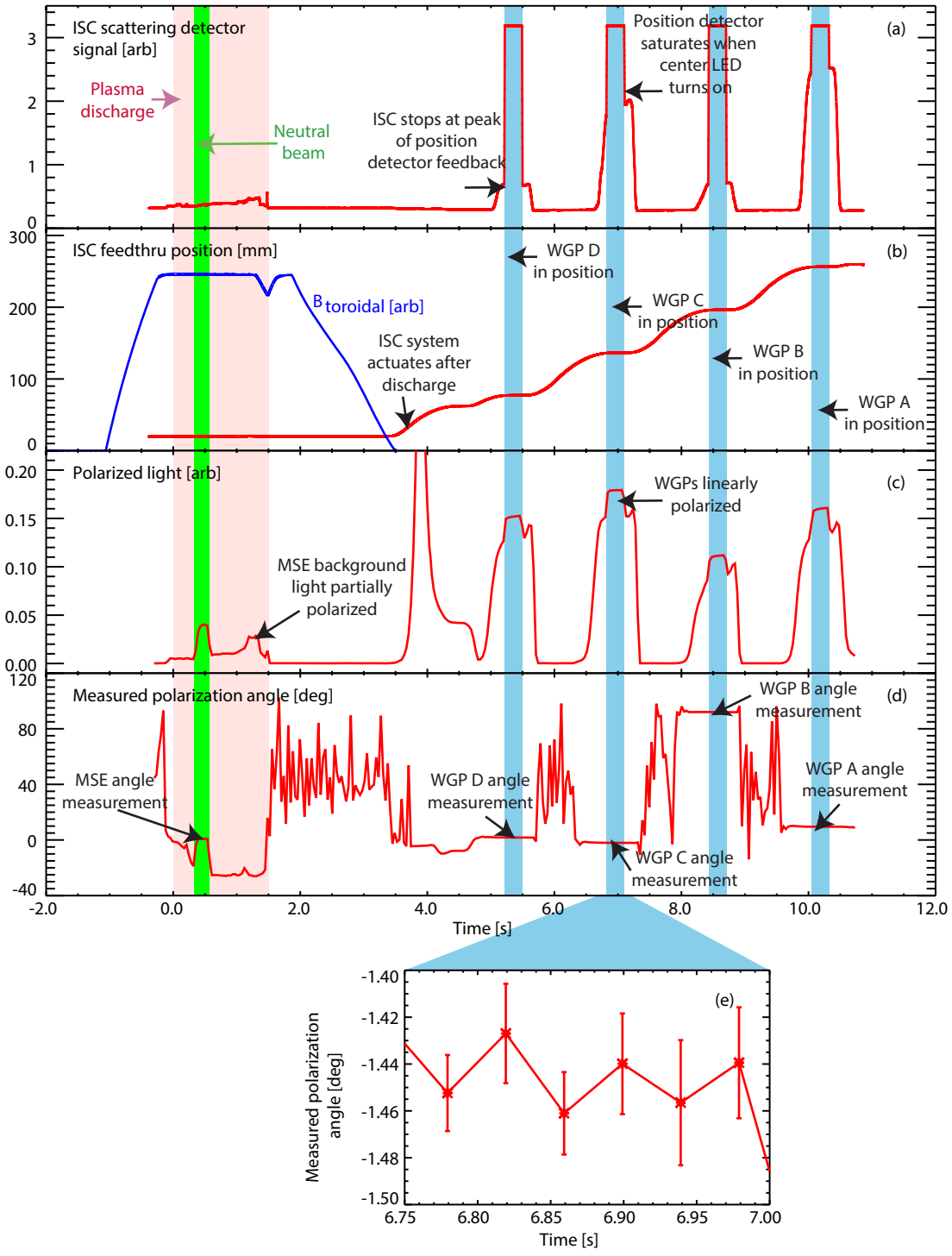

Figure 31: Operational traces from the ISC. The signal from the ISC scattering detector showing when the carousel is in the proper position, at which point the LED that shares the detector's fiber is activated, saturating the detector (a). The position of an ISC linear feedthru, showing the system moving after the tokamak magnetic field is ramped down and stopping at each carousel position (b). The polarized light intensity and polarization angle from a MSE sightline (c) and (d), respectively. The partially-polarized plasma emission is apparent (red shading) along with the polarized light from a single beam pulse (green shading). A zoom-in on the polarization angle is shown (e).

the very constant polarization angle with small polarization angle uncertainty. The polarization angle during the four measurement times is averaged and the standard error is calculated. This information is then used to determine the polarization calibration of the diagnostic.

The ISC is placed in a calibration position with a polarizer rotated in front of the diagnostic objective lens when the diagnostic is not operating (such as overnight between rundays). A single carousel position can be held in front of the lens and shots taken at regular intervals to track the diagnostic response over a specified time period. The ISC can also be slowly rotated in front of the objective lens to determine how sensitive the system is to the proper placement of the carousel in front of the lens; it is not very sensitive, achieving a 1° placement accuracy achieves a $< 0.1^\circ$ accuracy in polarization angle, though the ISC is substantially more reproducible. This slow rotation also scans through an order of magnitude change in polarized light intensity that can be useful for determining photo statistical scalings. The system can also act very quickly, placing the first carousel position in front of the diagnostic lens within 1s of the end of the discharge, though this places stress on the actuation components, and is typically not needed. The ability to precisely rotate the carousel can also be used to aperture the diagnostic lens with the edge of the carousel objective opening. This has been used to decrease the aperture broadening during MSE-LR and MSE-LR spectral experiments. Other sources of light can also be used in place of the red LEDs to calibrate the gains of the different wavelength channels in the MSE-MSLP system.

3.6 REPEATABILITY

The repeatability of the ISC system is very important to the calibration strategy. The entire technique relies on the ISC system's ability to repeatedly input the same polarization into the diagnostic despite changes to the diagnostic environment. To test its repeatability, the ISC system is cycled repeatedly during quiescent environmental conditions when nothing is expected to be changing. The standard deviation across the cycles can then be calculated for each MSE sightline for each WGP position. Figure 32 shows the results for a set of 15 cycles and 19 cycles after the initial installation of the ISC and after substantial use, respectively. Note that the standard deviation of these measured angles are $< 0.05^\circ$ for all sightlines for all four WGP positions. The average standard error of the individual WGP angle measurements, representing the uncertainty due to photon statistics, is shown as the dashed line. Note that the variability in the measured ISC angles is not significantly greater than the error in an individual measurement. The reproducibility is found to be better than the requirement irrespective of whether the tokamak is under vacuum or at atmospheric pressure. The ISC system has been cycled > 8000

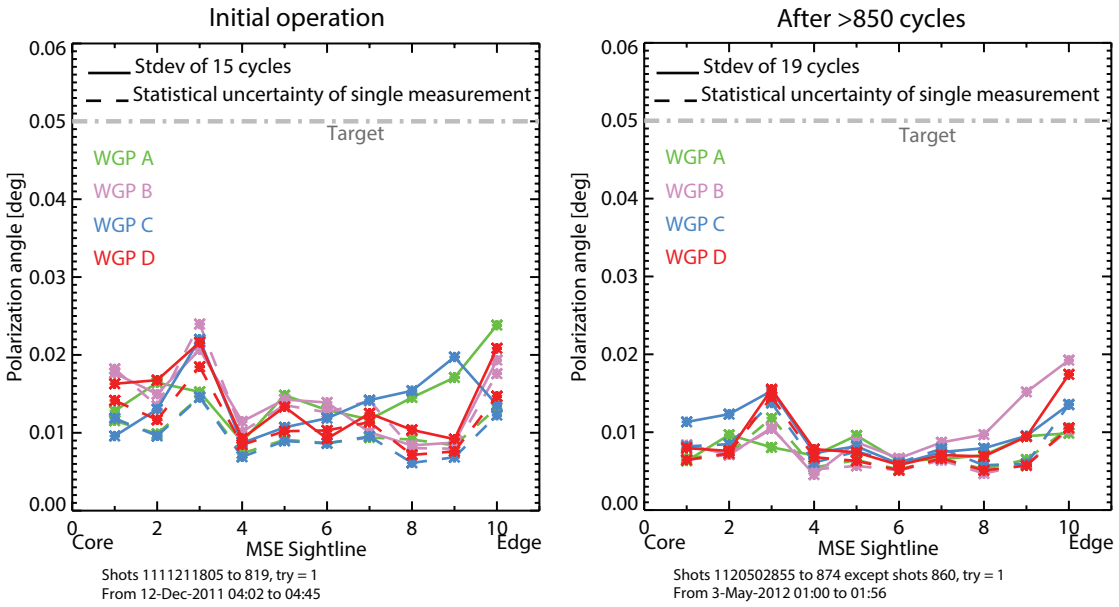

Figure 32: The ISC reproducibility after initial operation (left) and after a significant number of cycles (right). The standard deviation of the measured angle from a number of consecutive ISC cycles is shown for each MSE sightline for each ISC WGP. The statistical uncertainty in the individual measurements (calculated as standard error of the ~ 0.5s long measurement period) is indicated with the dashed line for comparison. The target reproducibility is also shown.

cycles to date and shows no degradation of its reproducibility. This data indicates that the ISC system is extremely reproducible, always inputting the same polarization into the diagnostic.

The ISC system can be used to monitor the diagnostic condition on a fast time scale for long periods of time, simultaneously sampling all the MSE sightlines. The capability to monitor the diagnostic performance online is very important for determining the cause of the diagnostic response changes. A very mundane example is shown in Figure 33 where the ISC system is used to monitor the diagnostic response over a weekend. The ISC system was used to input a constant angle into the diagnostic, taking data every 12 minutes during this period. The temperature of the invessel components are shown (a) along with the temperature of the vacuum window (b). Contours of the DOCP and the change in measured angle (referenced to the in-vessel calibration period) are shown in (c) and (d), respectively. Note that the polarization angle has changed from the invessel calibration period (presumably due to heating) but the circular polarization is low and both quantities are very stable as function of time.

3.7 PICKING THE POLARIZATION ANGLES

In addition to calibrating the diagnostic response to allow for accurate interpretation of plasma data, the ISC system is designed to provide data to identify the underlying cause of the time-varying diagnostic

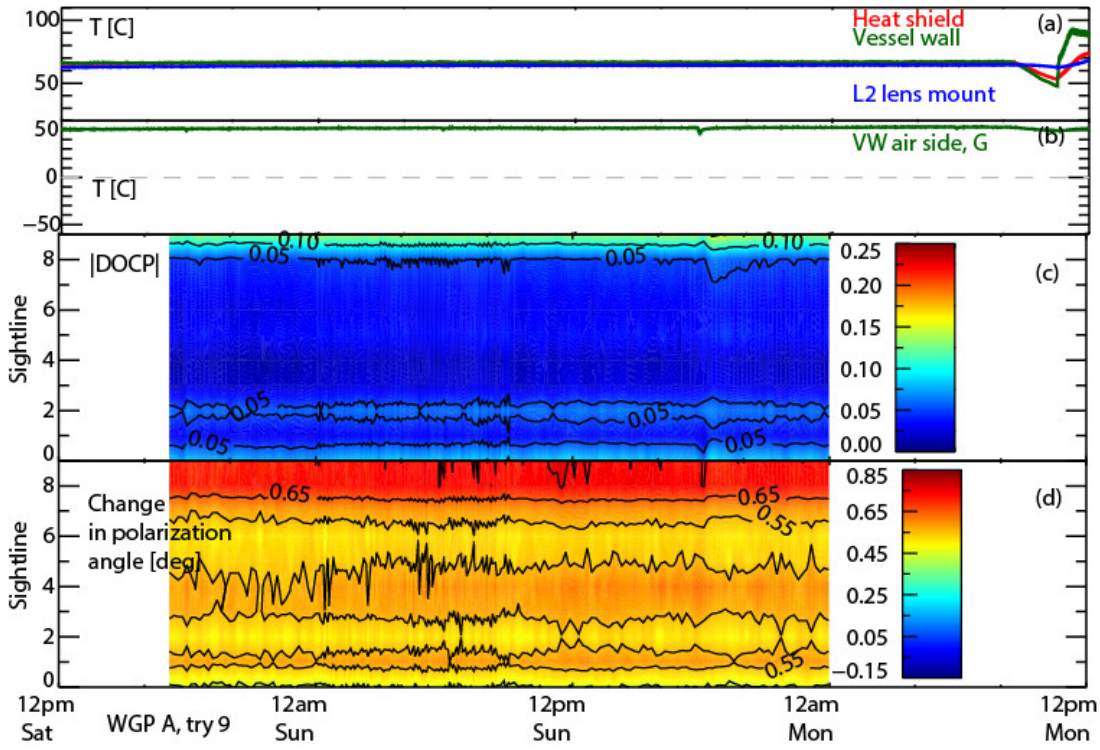

Figure 33: The ISC is used to monitor changes in the diagnostic response on multiple timescales. Here the diagnostic response is monitored across 30 hours when the tokamak is not operating but is under vacuum and at typical operating temperatures. The temperatures inside the vessel (a) and at the vacuum window (b) are constant. The ISC monitors the diagnostic every 12 minutes. The DOCP is shown to be low and constant and the measured $-\frac{1}{2}\tan^{-1}\left(\frac{I_{2\omega 1}}{I_{2\omega 2}}\right)$ is also constant, though differs from that observed during the previous maintenance period by $\sim 0.6°$.

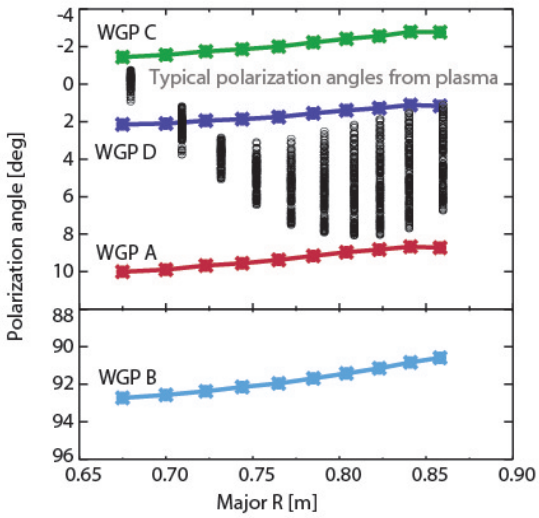

Figure 34: The ISC system's WGP angles as a function of sightline. Typical polarization angles from the neutral beam are superimposed for reference. Three angles (WGP A, D, and C) are used to obtain the diagnostic response in the polarization angle region of interest. Two WGP's produce angles that are very nearly orthogonal (B and D), allowing the ISC to determine if the character of any diagnostic response changes are of the form $\cos(2\theta_{pol})$ or $\cos(4\theta_{pol})$. The polarization angles from the plasma are taken from Ref [1].

response. This data is used to evaluate strategies to minimize those changes.

The polarization angles from the four different WGPs are shown superimposed on polarization measurements from the plasma in Figure 34. Three of the four ISC polarization angles are chosen to span the measurement range typically observed by the MSE system viewing the π emission from the beam. This allows the diagnostic response to be interpolated over the range of angles that is important for physics operations—at no point during the operation of the tokamak does the polarization response need to be extrapolated from the ISC measurements.

The fourth polarization angle is chosen to be orthogonal to the middle of the other three angles. As previously discussed, polarization aberrations usually have a $\sin(4(\theta_{pol} - \psi))$ or $\sin(2(\theta_{pol} - \psi))$ character. Analytic derivations and extensive experience with the in-vessel robotic calibration system both show that there are not other dependences (e.g., $\sin(6(\theta_{pol} - \psi))$). The two orthogonal WGP angles can therefore determine which of these terms likely describes the measured diagnostic response change. If the two nominally orthogonal angles drift closer or further apart then the diagnostic response change has a $\sin(2\theta_{pol} - \psi)$ character, indicative of changes in diattenuation or a change in the axis of the diattenuator (which is unlikely since the mirror orientations are firmly-fixed).

If the two orthogonal angles change in the same direction while remaining orthogonal, then the diagnostic response change has a $\sin(4(\theta_{pol} - \psi))$ character. A change in the offset term is also possible due to changes in the WGP orientation, warping of the MSE canister, or changes in the angle between the two PEMs. These mechanical changes are not possible due to the rigid design of the system and have been shown to not occur. A $\sin(4(\theta_{pol} - \psi))$ character is indicative of either retardance or errors in the PEM-based polarimeter

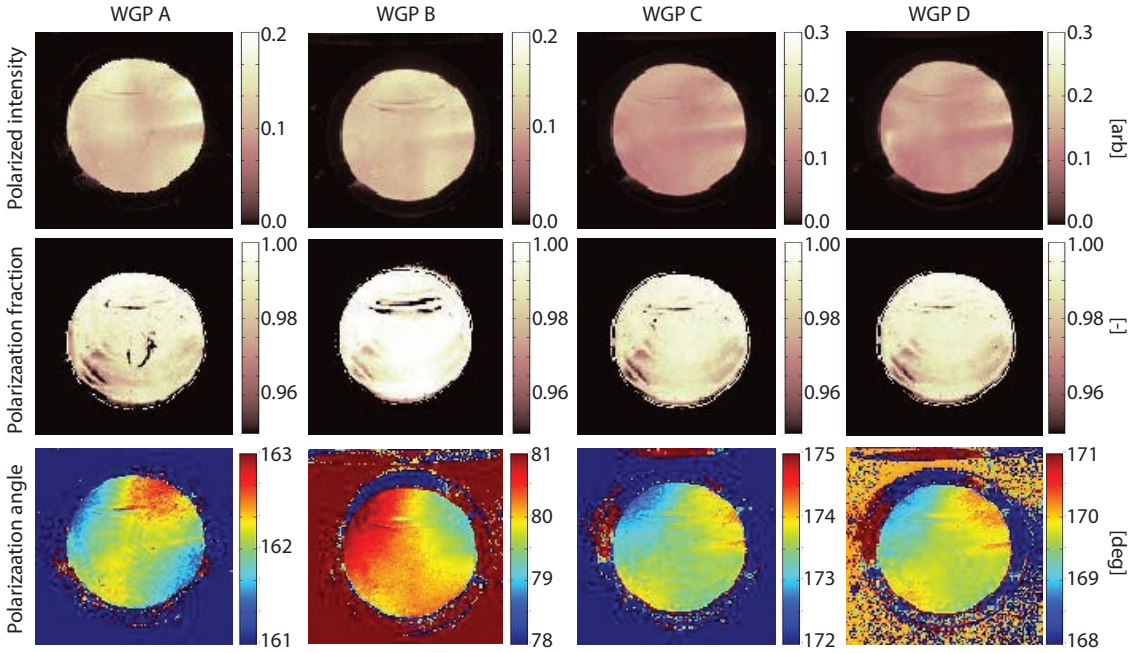

Figure 35: Polarized photos of the ISC illumination taken with the polarization-sensitive camera described in Reference [2]. The four WGP and illumination sources are shown in the columns. The polarized intensity (top), linear polarization fraction (middle), and polarization angle (bottom) are shown. These photos are taken from "upstream" of the ISC source after the L1 lens and M1 mirror. These photos are of the ISC system prior to the FY14 campaign, after the rebuilding of the illumination sources.

and/or detector operation. The changes in DOCP of the two orthogonal angles can then be used to determine which type of these changes is at fault. If the retardance changes, then the DOCP of the two orthogonal light sources will change by an equal and opposite amount. This could be caused by either changes in the magnitude of the retardance or a change in orientation of the fast axis of the retarder. An observation of no change in the DOCP of the orthogonal angles even as their measured polarization angles change (in the same direction) would indicate the a problem in the PEM-based polarimeter or detector system.

This orthogonal angle also provides the ability to calibrate the diagnostic response for a MSE σ measurement. Knowing the character of the response change can allow an accurate calibration using only one angle in the vicinity of the MSE σ light. If the two orthogonal angles change the same amount due to a $\sin(4(\theta_{pol} - \psi))$ error then the other two angles near in angle to the MSE π light can be used to infer the change in angle $\pi/2$ away from each one.

Photographs were taken of the ISC using the polarization camera discussed in Reference [2] to determine the polarization properties of the illumination from the ISC[5]. These photos are shown in Figure 35 (see Reference [2] for details of the experimental setup). The photos show the ISC illumination system as it would be observed from the

5 This was done after the rebuild of the system for the FY14 campaign.

MSE sightline on the optical axis from "upstream" of the MSE turret. The four different WGP and illumination sources are displayed in the four columns. The first row shows the polarized intensity from the source, the second row shows the polarization fraction and the third row shows the polarization angle. Note that the polarization angle is not referenced to any particular coordinate system and is shown only to judge uniformity and WGP-to-WGP changes. The sources fill the entire aperture of the lens with polarized light with fairly uniform intensity, though some striation is apparent. The polarization fraction of the light is very high (DOLP > 0.95) for most of the aperture[6]. The polarization angle has $\pm 0.5 - 1^\circ$ variation across the illumination surface.

The ISC system is primarily used as a calibration "transfer" mechanism, providing fiducial polarization angles into the diagnostic. Since the WGPs are mechanically stable relative to the vessel, they always input the same polarization angle into the diagnostic[7] relative to gravity, $\theta_{pol}^{WGP\,X}$. This polarization angle is determined during maintenance periods using the invessel robotic calibration system. The invessel robotic calibration system cycles through ~ 36 input polarization angles and the result is fit with Equation 6 to determine the calibration coefficients. The ISC is actuated immediately following this calibration and the $-\frac{1}{2}\tan^{-1}\left(\frac{I_{2\omega 1}}{I_{2\omega 2}}\right)$ is recorded. The calibration fit equation is then used to determine the polarization angle of the WGP with respect to gravity, $\theta_{pol}^{WGP\,X}$. In this manner the calibration is transfered from the invessel robotic calibration system to the ISC using the MSE diagnostic as an intermediary. This process can be done with high precision in the stable invessel environment.

The ISC was also used to monitor the changes due to birefringence when the periscope was heated. Figure 36 shows polarization changes due to heating of the L2 lens. The ISC was actuated during the heating to monitor changes. It is clear that the four ISC angles change in the same direction and with similar magnitude changes while the two orthogonal angles show opposite changes in DOCP. This behavior is consistent with birefringence. Note that the change in measured angle is different across the three WGP angles that are clustered together. Figure 37 shows a similar experiment in which the vacuum window was heated. Again, the two orthogonal input angles (blue solid and dashed) show the same change in angle and opposite changes in DOCP, consistent with birefringence. The largest changes in angle and changes in DOCP occur when the heating is turned on or off.

The ability of the ISC illuminate all the MSE sightlines and with four different input angles allows the diagnostic response to be in-

6 There is a horizontal scratch apparent in the polarization fraction across each WGP from damage during operation.

7 This assumes that the MSE periscope on which the ISC is mounted stays mechanically stable relative to the machine throughout the campaign. This is indeed the case.

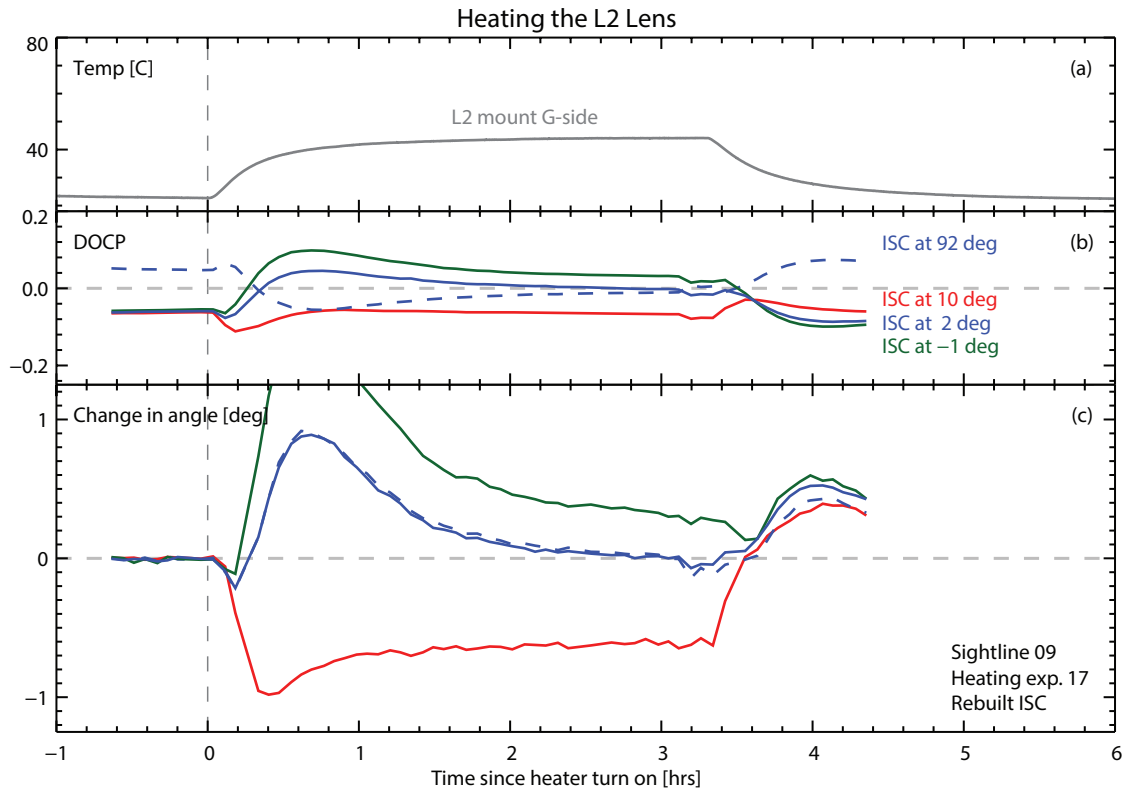

Figure 36: Measurements of the changing DOCP (b) and polarization angle (c) using the ISC while heating the L2 lens (a). Results from the four different ISC input angles are shown. The orthogonal angle (WGP B) is shown as dashed blue and its companion angle (WGP D) is shown as the solid blue line.

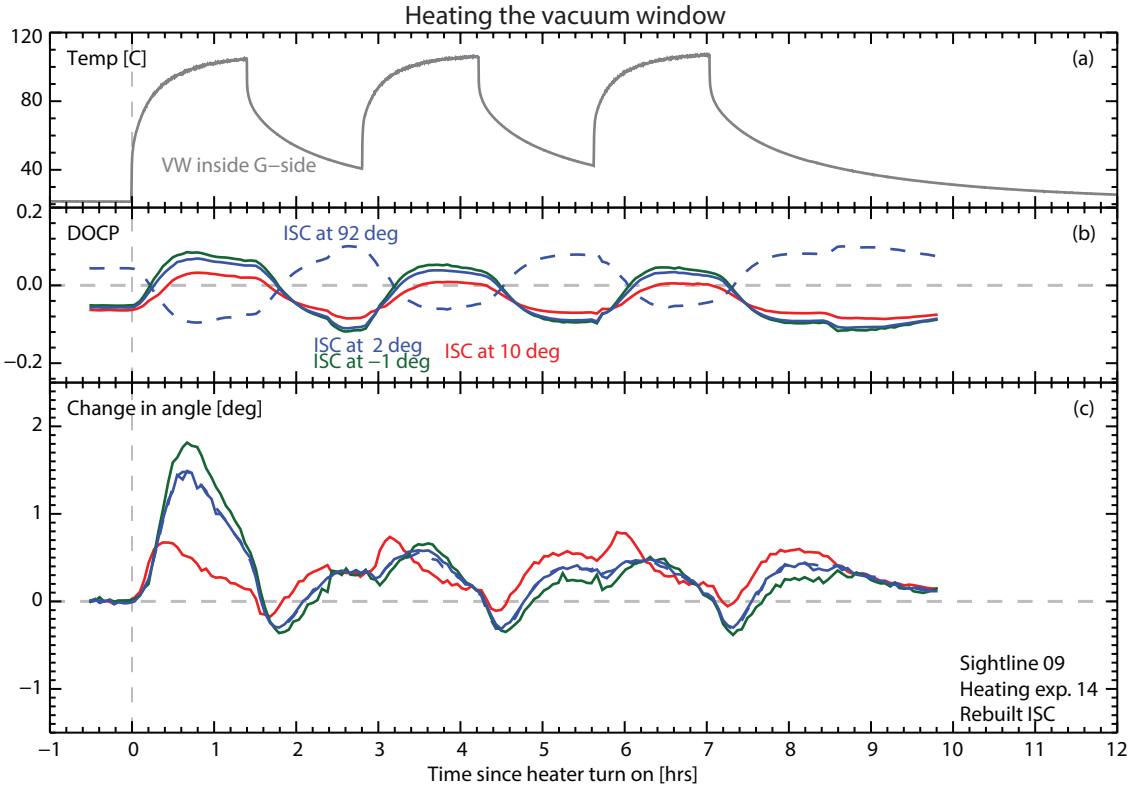

Figure 37: Measurements of the changing DOCP (b) and polarization angle (c) using the ISC while heating the vacuum window (a). Results from the four different ISC input angles are shown. The orthogonal angle (WGP B) is shown as dashed blue and its companion angle (WGP D) is shown as the solid blue line.

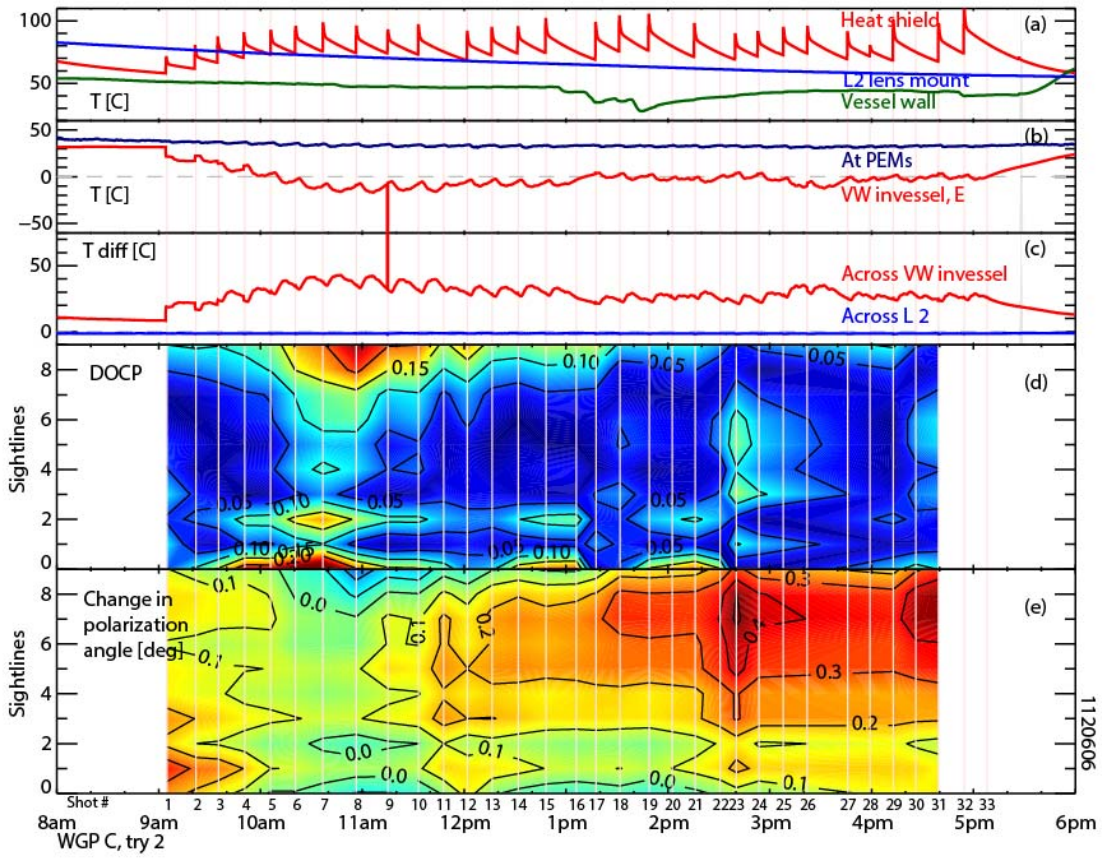

Figure 38: The ISC is used to measure the diagnostic response for all sightlines across a runday. The temperature of various internal (a) and external (b) components is shown along with the temperature difference across the L2 lens mount and the vacuum window (c). Contours of DOCP (d) and change in polarization angle (e) are shown for one input ISC polarization angle.

terrogated in detail at any point during the campaign. An example is shown in Figure 38. The DOCP (d) and change in polarization angle (e) is shown across the runday for all sightlines. Both quantities change at approximately 10:30am across many of the sightlines and then again at 2:30pm. The changes are typically worse at the edges of the field of view. For this runday there is not a identifiable cause of the birefringence as the DOCP does not follow changes in any particular temperature trace. The change in polarization angle is $< 1°$ though larger changes can occur. Generally, the diagnostic changes are not reproducible day-to-day.

BIBLIOGRAPHY

[1] J. Ko. *Current profile measurements using Motional Stark Effect on Alcator C-Mod*. PhD, Massachusetts Institute of Technology, 2009.

[2] R. Mumgaard. Development of a Polarization Camera. Technical Report PSFC/RR-15-8, MIT, May 2015.

4

THERMAL CONTROL OF THE MSE PERISCOPE

Extensive experimental evidence indicated that the harsh thermal environment inside and near the tokamak can create thermal stress-induced birefringence in the ten transmissive optical elements positioned optically upstream of the PEMs [1].

Thermal stress-induced birefringence occurs due to thermal gradients inside the optical elements, which create stress in the glass due to differential thermal expansion. Notably, stress can arise in locations other than where the thermal gradient occurs because of the continuous nature of the solid body. Conduction or radiation between the element and its mount and environment can cause steady-state thermal gradients resulting in stress. Thermal stress can also occur due to thermal conduction from spatially uniform thermal transients in elements with finite thermal capacitance as "waves" of temperature superimpose on themselves in the element. To minimize stress-induced birefringence in a transmissive element, the element must be as thermally isolated from temporally changing sources and sinks of heat as possible. Therefore, a primary goal in a polarization system with transmissive elements must be to surround the elements with both a spatially and temporally constant temperature environment. In the absence of this, the elements should be surrounded with a spatially uniform temperature environment that only changes slowly in time.

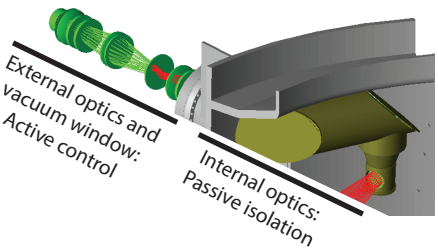

Figure 39: Thermal isolation scheme.

The decision was made to thermally control the entire MSE optical periscope, minimizing thermal gradients and transients in all transmissive elements from the objective lens to the PEMs. Studies were undertaken to determine the most feasible and effective techniques to thermally control different parts of the periscope. The internal periscope operates in vacuum, eliminating convection, leaving only conduction and radiation as the dominate thermal transfer mechanisms. Both of these mechanisms can be substantially reduced using passive designs. Therefore, it was decided to thermally isolate the internal periscope from its surroundings using a radiative heat shield, a low-conduction periscope mount, and a low-conduction lens mount. This strategy was intended to provide a slowly-changing but spatially uniform thermal environment for the five internal lenses. The external periscope and vacuum window (VW) are in highly transient thermal environments that include convection. For this reason, the tem-

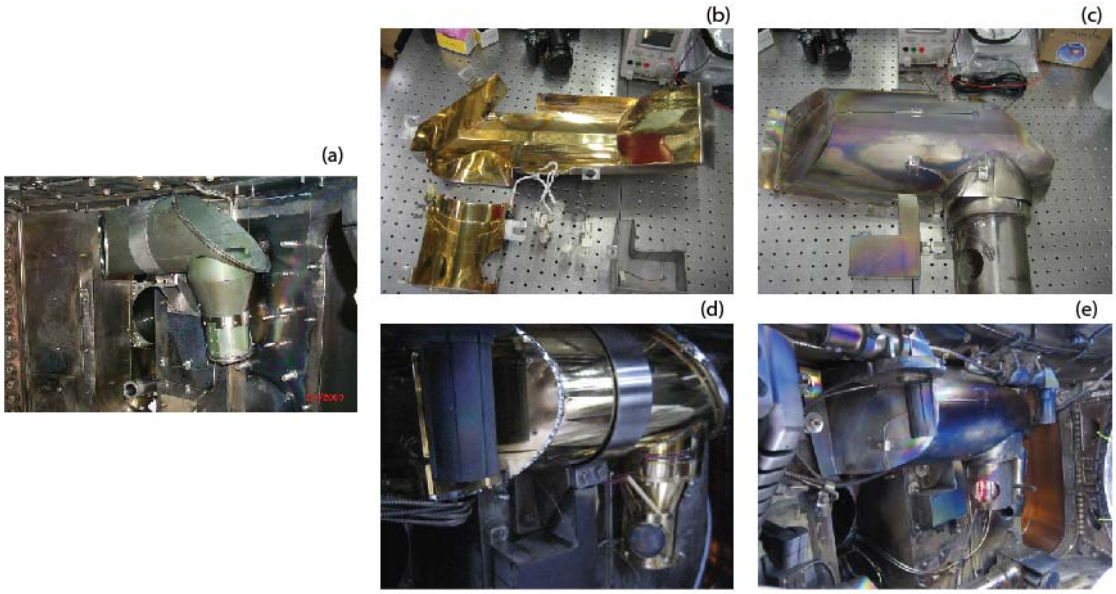

Figure 40: The periscope prior to major modification and gold-plating (a). The interior and exterior of the gold-plated heat shields (b) and (c), respectively. The gold-plated periscope mounted in the vessel (d) and with the heat shield installed (e).

perature of these size optical elements were controlled actively using water circulation, insulation, and hot air blowers. The schematic for thermal-control is shown in Figure 39.

4.1 RADIATIVE HEAT SHIELDS

A low-emissivity periscope coating and low-emissivity heat shields to cover and thermally isolate the internal periscope from the plasma and the vacuum vessel were conceptualized prior to this thesis [1]. As part of this thesis, two heat shields were developed, installed, and evaluated, one covering the "canister" portion of the periscope, and one covering the "turret" portion of the periscope. The heat shields fit tightly around the periscope, but do not contact the periscope—instead maintaining clearances of $1-3$cm. The shields cover the entirety of the plasma-facing parts of the periscope except the diagnostic objective lens and a small portion near the F-port vacuum flange. The ISC system also resides within the turret heat shield. The heat shields are constructed of high strength 1.5mm thick Inconel. The shields are fabricated from various shapes bent and welded to form a thin membrane. The shields' internal surfaces are polished to $2-4$microns and gold-plated, while the external surfaces remain unfinished.

The canister and turret shields are mounted to the vessel wall at 6 and 3 points respectively. All but one of the mounts on each shield is electrically isolated to prevent eddy currents from flowing from the wall through the shields. The shields act as free-standing membranes and, therefore, their mechanical design was dominated by the

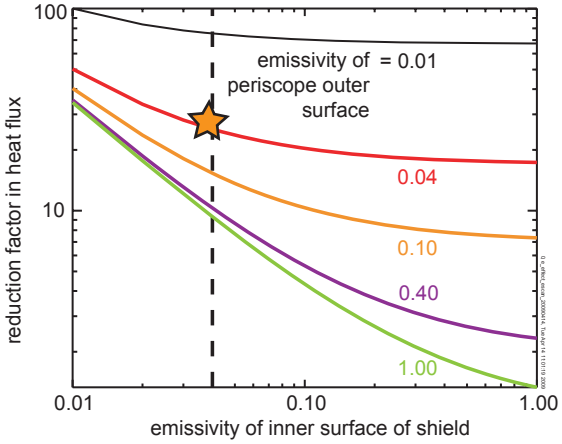

Figure 41: The reduction in heat flux to the periscope from a low-emissivity heat shield and low-emissivity coating of the periscope exterior. The achieve result is indicated with a star. Adapted from [1].

mitigation of disruption forces (many design iterations were undertaken by PPPL personnel to provide a shield that could withstand the large forces inside C-MOD without significant deformation). The close-fitting shields were warped from welding during fabrication, thus many modifications were required during installation to obtain the proper mounting configuration. The shields are instrumented with several thermocouples to monitor their thermal performance.

The exterior of the stainless steel invessel MSE periscope was also polished and gold-plated to provide a low-emissivity surface for additional thermal isolation. These surfaces face the interior of the heat shield and the vessel wall immediately next to the periscope, which remains unfinished stainless steel. The interior of the periscope was coated in black to prevent stray reflections. Photographs of the various components are shown in Figure 40.

The purpose of the heat shields is to absorb the radiation from the plasma, heat up, and then re-radiate the energy to the rest of the vessel between discharges. The low emissivity of the heat shields' interior and the periscope's exterior prevent this energy from being transfered to the periscope inside of the shields. The periscope is thus isolated from the periodic high energy flux from the plasma and from the rest of the interior of the vessel that is heated by the plasma. The low-emissivity coating on the periscope and low-conduction support mounts (discussed later) greatly decrease the heat transfer to and from the periscope. This leaves the periscope as an unforced thermal body in thermodynamic equilibrium with itself; the periscope's temperature changes slowly and uniformly, preventing thermal stresses from arising in the optical elements within the periscope.

Test coupons of stainless steel and Inconel 718 were polished and gold-plated using the same techniques by the same fabricators that polished and plated the actual MSE components. The emissivity (in the infrared) of these coupons was measured, yielding $0.02 - 0.04$ for the polished regions and $0.3 - 0.38$ for the unpolished regions.

Table 3: The change in thermal performance across a run-day when operating with and and without a low-conduction supporting mount.

Measurement	w/ low-cond. support	w/o low-cond. support
Difference across L2 mount	0.3°C	> 10°C
Difference across periscope	2°C	7°C
Periscope time constant	8hr	8hr
Periscope temp. slew rate	1.7°C/hr	2.0°C/hr

Assuming 95 percent of the periscope's outer surface and the shields' inner surface was properly polished leads to an average emissivity of $\sim$ 0.04. According to thermal calculations performed by Ko [1], shown in Figure 41, the heat shields should reduce the heat flux to the periscope from the plasma and vessel by a factor of $\sim$ 30. Since the wall of the vessel remained unfinished (i.e., at a higher emissivity of 0.3-1), the heat flux from the periscope to the vessel wall adjacent to the periscope is reduced by only a factor of $\sim$ 10.

The shields, with slight modifications, have survived five campaigns and show no major signs of damage due to over-heating. Visual inspection and swabbing of the internal gold-coating shows no deposition on these sensitive surfaces due to boronization or plasma deposition, though some slight arcing is apparent in low-clearance regions. Thermocouple measurements show that the shields' performance has not appreciably degraded since they have been installed.

4.2 LOW-CONDUCTIVITY PERISCOPE SUPPORT

The internal periscope has two high-strength mounts which support it from the vessel wall, one midway along the canister and the other at F-port near the vacuum window. The mount at the vacuum window is thermally tied to the F-port flange, which is under active control (discussed later). However, the support mount at the middle of the periscope provides a thermal conduction path to the vessel wall.

The importance of this connection to the periscope thermal behavior was indicated by a set of experiments conducted over two campaigns. This connection point was inadvertently loosened for a single campaign immediately following the installation of the heat shield. The connection point was tightened to provide proper periscope support after the error was discovered during the next manned-access. Thermocouple measurements during the subsequent campaign indicated a decrease in thermal isolation of the periscope by a factor of $\sim$ 10. In this configuration, the periscope temperatures were more closely tied to the vacuum vessel wall temperatures and larger thermal gradients across the lens mount resulted. Table 3 shows the

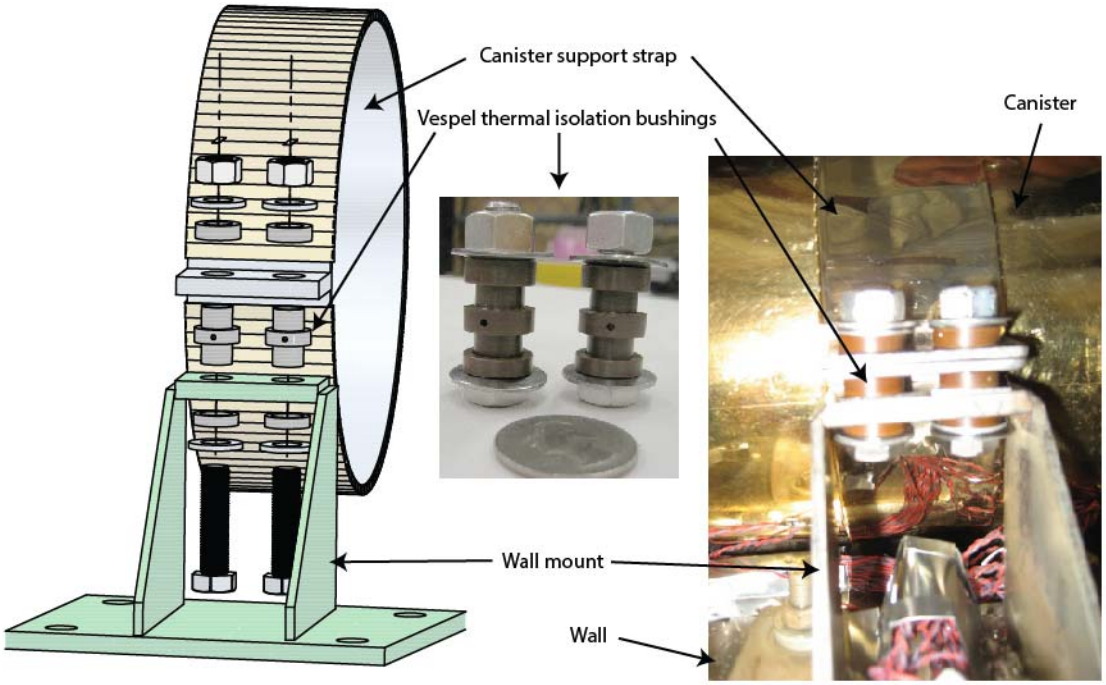

Figure 42: The low-thermal conduction canister support mount. The canister support strap is thermally isolated from the wall mount using Vespel thermal isolation bushings that separate the bolt from both the mount and the strap.

change from having an unconnected support to a connected support during a typical campaign run-day. A follow-up test was conducted at the end of this campaign; the vessel was entered and the connection was loosened, the vessel was pumped down, and then the vessel was baked. This test showed that excellent thermal isolation was recovered with a loosened connection, confirming that conduction through the connection significantly degraded the thermal isolation provided by the heat shields. A low-conduction, high-strength mount was designed and implemented following this discovery.

The low-conduction connection is shown in Figure 42. This connection replaced the stainless steel connection point at the canister support with a system of Vespel bushings. Vespel, a low-outgassing engineered plastic, has a low thermal conductivity of $< 0.5 \mathrm{W/m^{\circ}C}$ (compared to $\sim 15 \mathrm{W/m^{\circ}C}$ for stainless steel) and high mechanical strength. The bushings isolate the wall mount from the strap and the bolts from either piece. Installation of the bushings resulted in the thermal isolation being restored to the level when the support strap was not tightened, indicating the conduction path had been eliminated.

4.3 LOW-CONDUCTIVITY LENS MOUNT

The low-emissivity heat shield and low-conductivity periscope mount significantly improved the thermal environment inside the internal periscope. However, modeling indicated further thermal isolation was likely required for one internal lens in particular. The L2 doublet consists of the second and third lenses in the optical system. The MSE sightlines are nearly in focus at these lenses. Since all the rays within a sightline sample nearly the same glass volume, any stress-induced birefringence results in gross changes to the polarization response for that sightline. Analytical and empirical investigation by Ko [1] indicated that a further reduction in conduction between the L2 lens and its mount was required to stabilize the thermal-stress induced birefringence. The mounting system for this lens was redesigned to decrease the conduction from the mount to the lens by the desired factor >10.

The challenges for such an optical mount inside the vessel are:

1. Hold the lenses in a known, fixed position in the optical train
2. Cushion the lens against disruptions, returning the lens to the same position afterwards
3. Provide a low-thermal conduction pathway between the glass and the lens mount
4. Prevent excess fixed mechanical force from being exerted on the lens

Several design iterations led to a solution that fit the requirements and could be implemented in the tight spatial constraints. Each lens is positioned and cushioned with three Viton O-rings that run around the circumference of the lens at its edge, one on the top, one on the bottom, and one on the side. However, the O-rings are not in contact around the entire periphery of the lens. At eight small sections, the "gland", or channel in which the O-ring resides, is appropriately sized to support the lens, but for the rest of the periphery, the gland is significantly oversized. There is sufficient clamping pressure at these eight positions equally spaced around the lens to accurately and reproducibly locate the lens in the mount. In normal operation, the lens is mechanically supported only at these locations. The oversized channel at the rest of the periphery means the O-ring is only in incidental contact with either the lens or the mount. This configuration was termed the "sausage O-ring" concept since, when installed, the O-ring is pinched at small, regularly spaced intervals similar to a string of sausages. During a disruption, when the lens is accelerated toward the mount, the O-ring is easily compressed at the small channels. The lens then compresses the O-ring everywhere, at which point the O-ring fills the larger channels, cushioning the lens before it

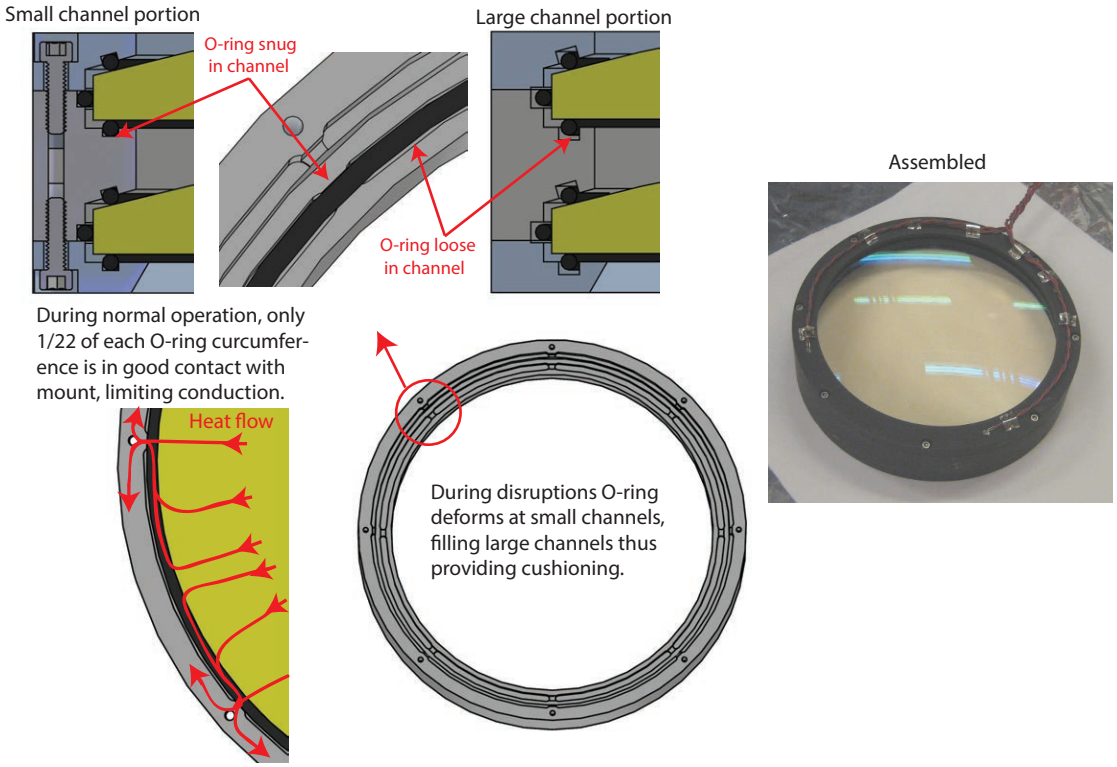

Figure 43: The low thermal-conductivity "sausage O-ring" lens mount uses three Viton O-rings to hold each lens and cushion it against disruptions. The channels, or "glands", that contain the O-rings are oversized except at eight small sections. The O-ring is only in incidental contact with the lens and/or mount in the large channel portion of the mount, limiting thermal conduction.

can make contact with the metal mount. During this time the lens is supported by a much larger section of O-ring, distributing the force. After the disruption, the lens returns to being supported by the eight smaller support points. In this way, the sausage O-ring acts similar to a progressive spring; the spring constant is low in normal operation, but then gets much firmer when the O-ring is compressed into its over-sized gland during a disruption.

The configuration is shown in Figure 43. In a typical O-ring mounting system, the O-ring is tightly compressed between the lens and the mount around the entire circumference. Therefore, the thermal conduction path between the lens and the mount goes through the O-ring and is radial and uniform at all points around the circumference. Furthermore, the O-ring is tightly compressed around its entire length, providing a better conduction path due to decreased thermal contact resistance. In the sausage O-ring mounting system, the geometry is such that the eight snug gland locations only account for only $\frac{1}{22}$ of the circumference of the lens. The conduction path then has an azimuthal component; heat must travel to the small supporting portions where the O-ring is in contact with both the lens and the mount. This has the effect of decreasing the thermal conduction between the

mount and the lens by a factor similar to the reduction in contact area.

Additionally, the size of the O-ring glands are carefully specified so the lens is normally held with minimal contact pressure, increasing the thermal contact resistance. The calculated thermal conduction resistance between the mount and the lens is a factor of 10 to 30 higher in the sausage O-ring design than the constant-contact O-ring design previously used for this lens mount, although this has not be confirmed experimentally. The radiation environment that the L2 lens observes inside the MSE periscope consists primarily of the M2 mirror, the M1 mirror, and the MSE turret. These elements are all within the radiative heat shield, hence they present a slowly changing, uniform thermal environment that prevents radiative forcing of the lens temperature.

Various iterations of the sausage O-ring design were tested using a fixture designed to simulate a disruption. A flat piece of glass was substituted for the lens in a lens mount with the proposed O-ring geometry. The lens mount was repeatedly dropped from chest height along guide rails, impacting a heavy steel baseplate. An accelerometer was mounted on the lens mount to measure the acceleration at the point of impact. The final sausage O-ring design was tested to over 200 g's without fracture of the glass, giving confidence that this design could survive a C-Mod disruption.

The L2 lens doublet mount is made of Inconel 718, a high-strength nickel alloy. The strength of the mount is intended to prevent mechanical forces from the MSE periscope from being transmitted to the lens. The mount is black passivated to prevent stray reflections. There are four thermocouples welded to the mount at equally spaced intervals to measure the thermal gradients around and across the mount. The mount is then attached to the MSE canister using interference-fit pins.

4.4 ACTIVE CONTROL OF THE VACUUM WINDOW AND EXTERNAL OPTICS

Previous work [1] highlighted the importance of the thermal stress-induced birefingence in the internal periscope and indicated that the external periscope and vacuum window were not a significant source of birefringence. The internal periscope was therefore thermally controlled first using the previously described passive-controlled system.

Experience indicated that the vacuum window and external optics were a significant source of additional thermal stress-induced birefringence. The active thermal control system on these elements has two goals: first, to minimize any thermal spatial gradients by creating a uniform thermal environment around each optical element and, second, to minimize and slow any thermal transients around the the optical elements.

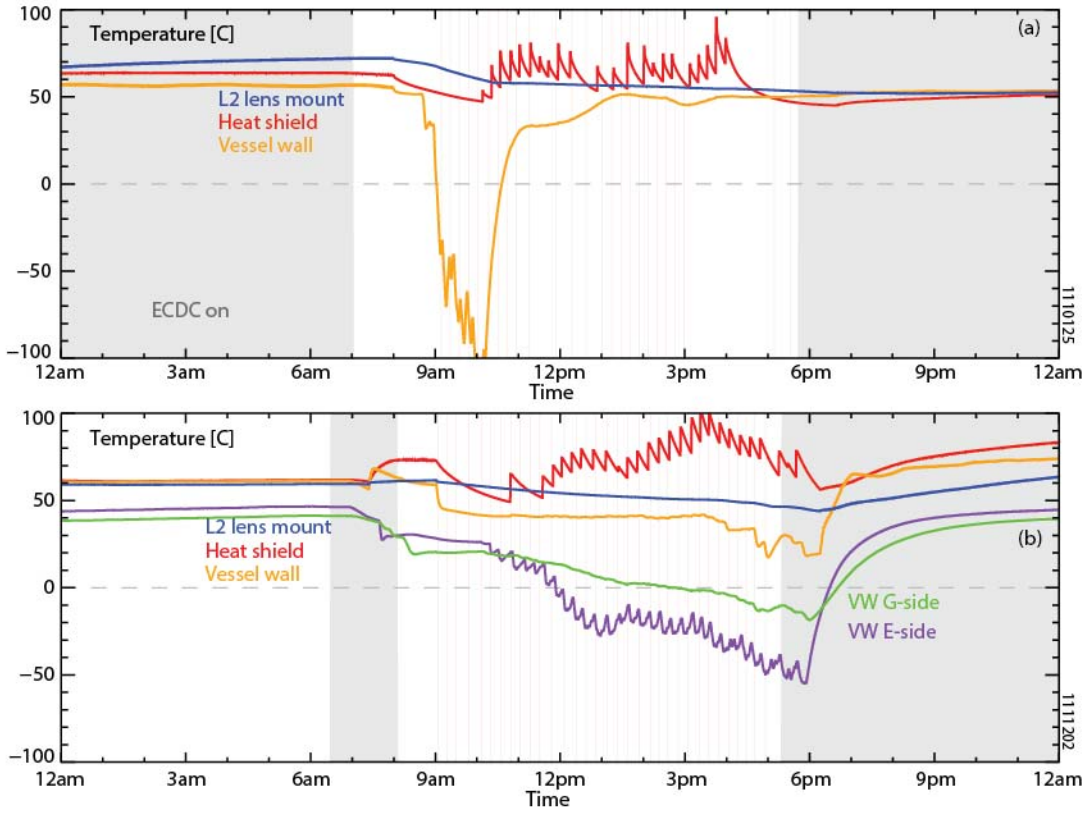

Figure 44: Two examples of large vessel cooling events. The temperature of the vessel wall near the MSE periscope cools over 150°C very rapidly over the course of an hour while the heat shield and thermally isolated periscope maintain their temperatures (a). The vacuum window flange cools by ~ 100°C throughout a runday while developing a large temperature gradient (b).

The vacuum window and external periscope operate in a harsh thermal environment due to the particulars of the C-MOD's construction and operation. The cryogenically-cooled toroidal field magnets are within 10cm of parts of the vacuum window and are cooled with liquid nitrogen immediately after each plasma discharge. This cooling can last up to 15 minutes. During this time, the air temperature inside the port area can decrease by > 50°C. The intensity of the cooling can bring the temperature of the port flange containing the vacuum window down to -120°C. This cooling routinely causes large chunks of ice to develop inside the port areas from water vapor that condenses on the cold port flanges. Many small space heaters with blowers are used to circulate warm air into the port areas to mitigate this icing. Unlike many cryogenic tokamaks, a thin flexible membrane connects the vacuum vessel to the rigid cryostat at each port opening, retaining the liquid and gaseous nitrogen inside the cryostat. This membrane is kept above atmospheric pressure causing the membrane to envelope the various diagnostics that exit the port. Thus the external MSE periscope comes in contact not only with the port flange, but also with the cooled cryostat membrane.

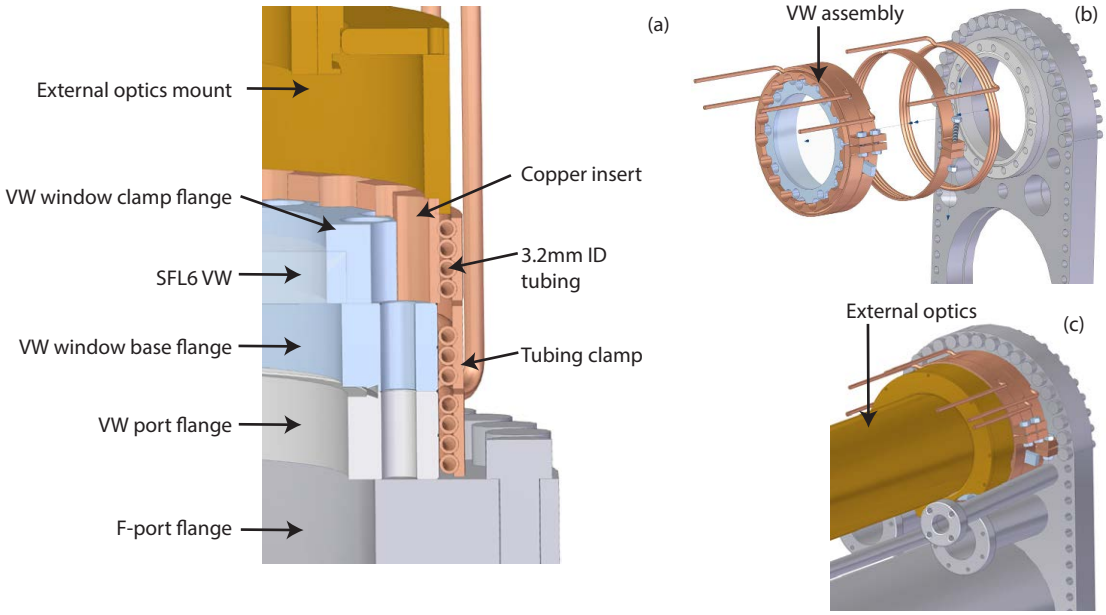

Figure 45: The design of the thermal control hardware for the external optics. A section view of the vacuum window "stack" wrapped with tubing (a). The stack assembled onto F-port (b) and with the external periscope installed (c).

Because the cooling is predominately through the use of liquid nitrogen, the temperature of the port can change very quickly—by $> 50°C$ a minute. The various sections of the vacuum vessel are equipped with electrical resistance heaters, but these cannot compensate for this large, localized cooling. An example of a large cooling event measured at the F-port flange near the MSE vacuum window is shown in Figure 44. The coarse nature of the magnet cooling system means that many times some locations will become much colder than others. The magnet to the E-side of the MSE port appears to have a leak in the nitrogen cooling lines, reaching temperatures $> 50°C$ colder than the G-side of the port at times, creating large thermal gradients.

The vacuum window is, by design, mechanically well-connected to the vacuum vessel. The large thermal transients and gradients around the port flange are therefore transmitted to the vacuum window itself via conduction. Various schemes were explored to thermally isolate the vacuum window from the F-port flange using intermediary structures such as bellows or low-thermal conduction materials. However, these schemes would require refitting of the delicate vacuum window in its mount and possibly changing the location of the window in the optical path. Instead, a solution was devised to thermally connect the vacuum window to another thermal body in a way that can dominate the conduction from the F-port flange. This system consists of circulating fluid from a thermally-controlled reservoir around the periphery of the vacuum window mounting flanges.

This implementation is shown in Figure 45. The vacuum window "Stack" consists of four pieces. The SFL6 vacuum window is clamped with Viton seals between a window clamp flange and a window base flange. The window base flange has a con-flat knife edge that allows it to seal to standard vacuum hardware. The assembled vacuum window is then bolted to the vacuum window port flange, which is permanently welded to the large oval F-port flange. The mount for the external periscope fits over the vacuum window stack.

Thin-wall 3.2mm inner diameter copper tubing is wrapped around each of the three metal elements in the vacuum window stack and clamped in place using custom copper band clamps. The size of the tubing was dictated by space constraints from other flanges and tubes near the MSE vacuum window. The soft copper tubing deforms against the vacuum stack elements to make good thermal contact. Each of the the three stack elements has three loops of tubing surrounding it. Fluid is circulated at a high Renyolds number through the tubing. The fluid-filled tubing alleviates thermal gradients around the circumference of the vacuum window stack; the flowing fluid thermally "short-circuits" the stack around its periphery. The fluid is recirculated from a reservoir that is held at a constant elevated temperature. The conduction into the tubing and convection to the fluid is strong enough to compete against the conduction into the stack from the F-port flange, thus the system stabilizes the temperature of the stack against thermal fluctuations from the magnet cooling.

Thermal simulations were conducted in the multi-physics software COMSOL to determine the effectiveness of this approach. A thermal model of the geometry of the vacuum window stack and the F-port flange around the MSE area was created, including contact resistance between the window and its mount. A high-fidelity model that included the copper tubing was compared to a reduced model with a scaled uniform heat transfer coefficient at the periphery of the vacuum window stack. The comparison showed good agreement between the two cases, thus the reduced model with a uniform heat transfer coefficient around the periphery of the vacuum window stack was used for further investigation. A $\pm 5°C$ temperature difference was applied across the F-port flange and the maximum thermal gradient in the vacuum window was calculated as a function of the heat transfer coefficient in the tubing. The steady-state solution of the vacuum window stack under these assumptions is shown in Figure 46. A heat transfer coefficient in the tubing of $5000 W/m^2 K$ was chosen as the design point. This value is sufficient to decrease thermal gradients, while higher heat transfer coefficients produce diminishing returns as conduction within the vacuum window stack becomes the limiting factor.

Time-dependent simulations were conducted to determine how well the system damps thermal transients with the design point heat trans-

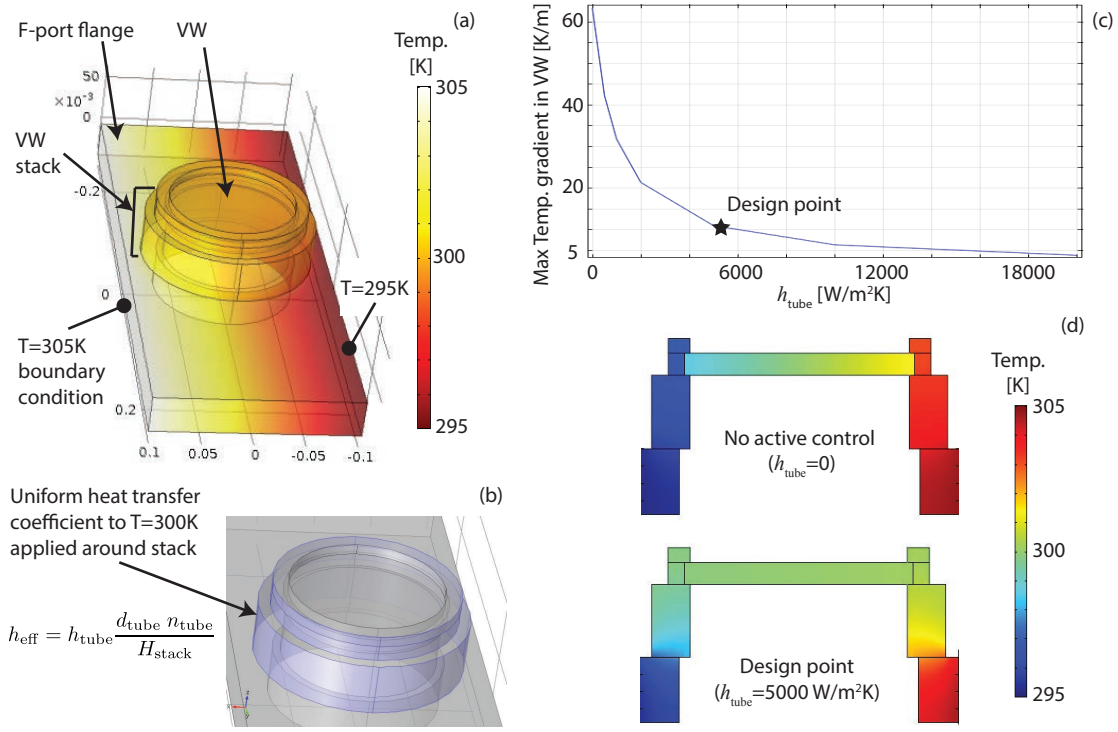

Figure 46: The model setup and results from COMSOL for the active cooling of the vacuum window. A reduced model of the area around the vacuum window including the window, the flanges comprising the vacuum window stack, and a slab representing the 37mm thick F-port flange was used. A $\pm 5°$C temperature gradient is imposed by setting the sides of the flange to a fixed temperature boundary condition (a). An effective heat transfer coefficient (scaled from the heat transfer in the tubing, the height of the stack, and the number and diameter of the tubes) is applied to the periphery of the vacuum window stack with the fluid temperature being the mean of the two boundary conditions (b). The maximum thermal gradient in the vacuum window is calculated as the heat transfer coefficient in the tubing is scanned (c). Slices through the vacuum window stack and flange are shown for the case with no active control and for the design point heat transfer coefficient (d).

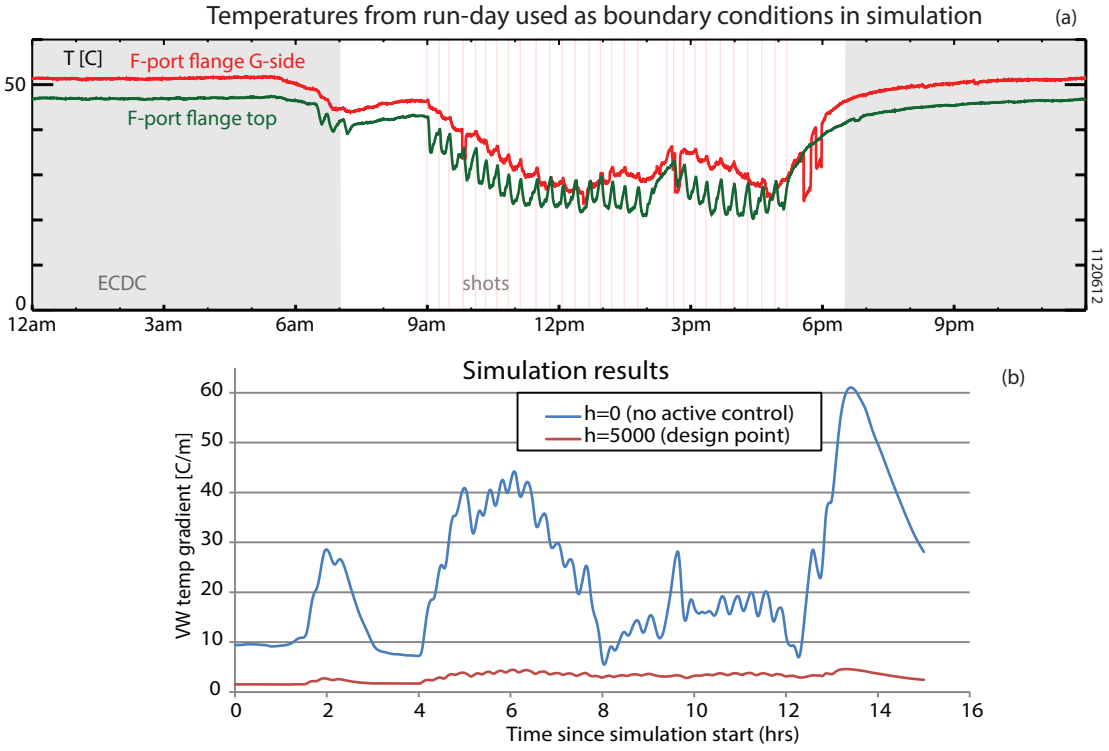

Figure 47: Measurements of the F-port flange temperature from a typical runday (a) were used as boundary conditions for each side of the F-port flange in the COMSOL simulation. The volume-averaged temperature gradient in the vacuum window was calculated for the situation with no active thermal control (blue) and with the design point active control (red) as a function of time (b).

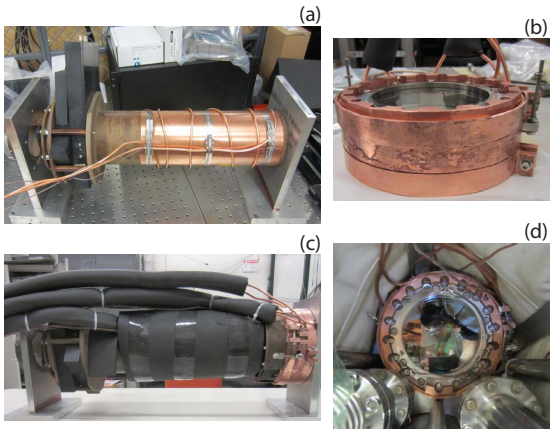

Figure 48: Photographs of the active thermal control system for the external periscope. The external periscope is wrapped in copper and tubing (a). The vacuum window stack assembled with the three fluid circuits, each with three loops of tubing, clamped around the periphery of the flanges (b). The entire vacuum window and external optics assembled on the bench (c). The vacuum window stack with thermal system installed on F-port.

fer coefficient identified from steady-state simulations. Actual temperature time-histories of each side of the F-port flange during a runday were used as boundary conditions on each side of the F-port flange in the model. The simulation was run with both the design point heat transfer coefficient and without heat transfer around the vacuum window periphery to mimic the current implementation and the planned implementation, respectively. The volume-averaged temperature gradient in the vacuum window was extracted at each time point. The results of this analysis are shown in Figure 47. The simulations predicted the active cooling system would reduce the average temperature gradient in the vacuum window by an order of magnitude and dampen temperature transients due to the cooling of the magnets.

Photographs of the system installed on C-MOD are shown in Figure 48. The external MSE periscope operates in air where convection is dominate, causing these elements to respond to the changes in port air temperature and to the temperature of the cryostat membrane. To thermally control the external periscope, it is surrounded in copper sheathing and wrapped with copper tubing with fluid flow as shown in panel A. The three-element vacuum window stack with tubing and band clamps assembled on the bench is shown in panel B. The external periscope and the supply and return tubing is wrapped in insulation as shown in panel C, which includes all the elements of the vacuum window and external periscope assembled on the bench. The vacuum window stack installed on F-port is shown in panel D.

Tests with freezing water in the tubing showed that the tubing would not burst, therefore water could be used in the system, simplifying its design. The de-ionized water is supplied to the coils at 65°C from a closed loop circulating system shown in Figure 49. The water is circulated from a 30 liter insulated tank to provide a large thermal capacitance to slow any of thermal transients imposed on the system. A heater with a thermal controller is incorporated to keep the tank of water at a constant temperature within 0.5°C. A centrifugal pump supplies water at 650kPa with a total flow rate of $9^{L}/_{min}$. The system

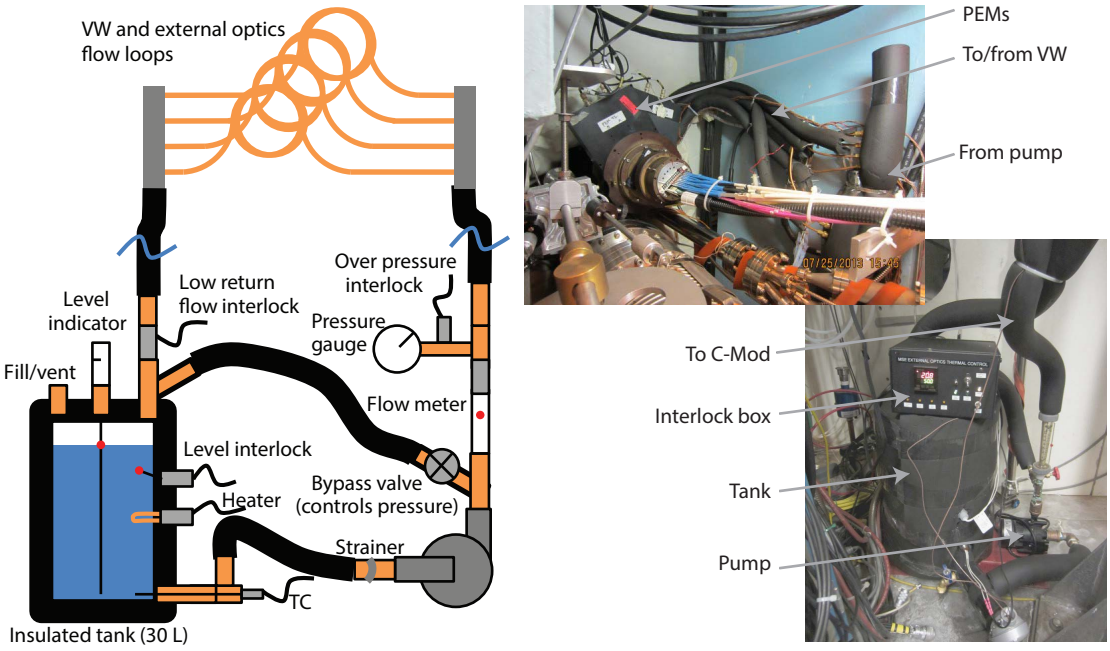

Figure 49: Schematic of the fluid supply system for the active thermal control (left). Photographs of the supply lines to the external periscope (right top) and the tank and pump (right bottom).

was designed to supply the required Reynold's number (32,000, resulting in fully turbulent flow) to provide a factor of safety of > 3 for the design point heat transfer coefficient inside the tubing. The water is transported 5m via insulated piping to a manifold at the port area, which distributes the water in four parallel insulated branches, one for each of the three elements of the vacuum window stack and one for the external periscope. The water is then returned to the tank via another insulated manifold and pipe. The system includes interlocks for over-pressure, insufficient return flow, and low water level.

In addition to the recirculating water system, hot air blowers are also used to regulate the temperature inside the port and to provide heating on the periphery of the F-port flange to counteract the magnet cooling the flange. Three blowers with attached space heaters are used to blow air at $\sim 65°C$ deep into the port via 50mm diameter tubing. For to the FY15 campaign, the air was directed into sandwiched corrugated plastic panels to better direct and distribute this air at the F-port flange. These panels sit between the external optics and the cryostat membrane to effectively envelope the external optics in hot air instead of the cold membrane.

4.5 THERMOCOUPLE MONITORING

The thermal environment is monitored to determine the effectiveness of the thermal-control scheme. The important parameters to measure are the temperature slew-rates, the temperature gradients across

the transmissive optics, and the temperature differences between the heat shields and the components inside them. A new thermocouple-based high-precision thermal monitoring system was designed and installed prior to the FY09 campaign. A vacuum feed-through and internal patch-panel enabled 20 type-K thermocouple measurements to be installed inside the vacuum vessel. The thermocouples are welded onto the periscope, lens mount, heat shields, vessel wall, and F-port flange to obtain accurate temperature measurements. An external patch panel enables 12 additional thermocouples to be mounted outside the vacuum on the external optics and vacuum window. All of the thermocouples use high-precision thermocouple wire throughout their wire runs. Table 4 lists the current thermocouple installation locations.

Table 4: Current thermocouple locations

Component	# of TCs
L2 mount	4
Canister	3
Heat shields	5
Vessel wall	2
VW interior	4
VW exterior	3
F-port flange	3
External optics	4
Water tank	1

The data from the 32 thermocouples is logged by a dedicated data-acquisition system. All the thermocouples are simultaneously sampled with 24-bit resolution and each thermocouple channel is cold-junction-compensated to enable absolute temperature measurements with an accuracy of $\pm 0.16°C$. This system continuously records the data at rates up to 10Hz—though typically 0.1Hz is used—and the data is stored in the MDSPLUS database. Since its installation, the system has logged $>$ 1.5GB of temperature data. The fast time-response and high accuracy of the system allows for an investigation of how energy is transfered among the different components of the MSE system, and the data has been used by others to benchmark thermal models of the interior of C-MOD. Software programs have been developed to retrieve the desired data from the MDSPLUS tree to correlate changes in polarization calibration to the temperature time-histories of the MSE components.

4.6 THERMAL PERFORMANCE

The goals for the thermal control system were determined empirically by Ko [1] using various heating tests. These specifications were for the thermal control of the L2 lens doublet that, at the time of the tests, was thought to be the only element experiencing significant thermal stress-birefringence. The specifications are elaborated in Table 5. The key parameters identified are the temperature difference across the L2 lens doublet, the temperature slew rate of this element, and the thermal time constant of the periscope.

The temperatures of the internal components across a typical run-day are shown in Figure 50. The measurements prior to the installation of the thermal control system are shown in panel A. Unfortunately, the extensive thermal monitoring system was not installed at that time. Two other thermocouples installed on the MSE periscope

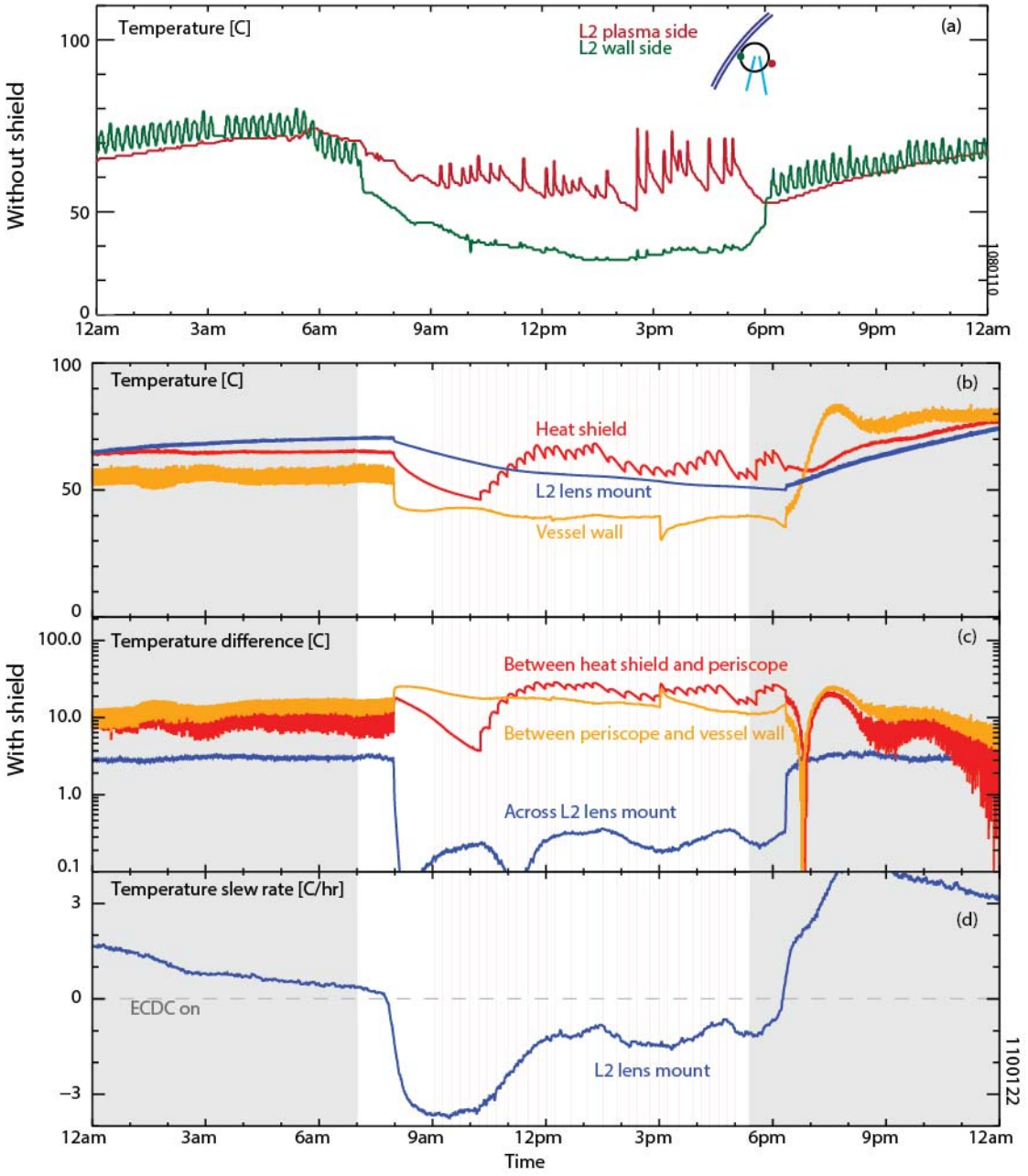

Figure 50: Temperature measurements at two locations on the internal periscope near the L2 doublet prior to the installation of the thermal isolation systems (a). The location of the measurements on the periscope are shown in the inset figure. Temperature measurements of the heat shield, L2 lens mount, and the vessel wall near L2 across 24 hours during a typical C-MOD runday after the installation of the thermal isolation system (a). The temperature differences measured between the shield and the periscope, the periscope and the wall, and across the L2 lens mount (b). The slew rate of the L2 lens mount temperature (c).

near the L2 doublet are displayed, one on the plasma-facing side (red), and one on the wall-facing side (green). Note that the plasma-facing side of the canister experiences heating from the plasma discharges, resulting in rapid changes in the temperature on this side of the periscope. The temperature difference across the periscope is 20°C most of the runday. Additionally, the periscope changes temperature quickly before the run at 7am and heats up quickly after the run at 6pm.

Shown in the lower panels is the thermal response after the passive thermal isolation was installed. Periods of electron cyclotron discharge cleaning (ECDC) are shown as gray shaded regions and the times of plasma discharges are indicated by vertical lines. The temperatures of various components are shown in panel B. The heat shield is heated by ECDC overnight and then starts to radiatively cool at 7am when ECDC ceases. Plasma discharges then heat the shield during the runday, causing it to ratchet up in temperature. Each individual plasma discharge causes a spike in temperature followed by an exponential decay. The vessel wall heaters are turned down from their overnight bake at 7am, and the vessel cools slowly. The vessel stays at constant temperature most of the runday and then resumes baking immediately after the runday ends.

The thermal isolation of the periscope is effective, creating a long time constant, $\sim$ 8hr, for the periscope to change temperature. This time constant is similar to that predicted for the system during the design stage. The periscope slowly heats up overnight, absorbing heat from the wall and heat shield. Then, after the heaters and ECDC are shut down, the periscope slowly cools throughout the runday. The heating from the plasma is not measurable on the periscope. Once the runday is over, the periscope begins to slowly heat up during ECDC and the cycle repeats. There are never any large or rapid temperature changes in the periscope.

The temperature differences between various invessel elements are shown in panel C. The temperature difference between the shield and the periscope can reach > 50°C immediately after plasma pulses. The periscope also maintains a temperature difference of up to 30°C between itself and the wall. Meanwhile, the temperature difference across the L2 lens mount is less than 0.5°C; this element does not have external gradients imposed on it. The temperature slew rate of the periscope is shown in panel D.

The specifications for the thermal isolation of the invessel periscope are shown in Table 5 along with the values prior to and after the installation of the isolation system. The system nearly achieves all of its design goals and improves on the un-isolated installation by factors of 5 to 80. These measurements show that the internal periscope is well-isolated from the wall and plasma, slowly changing in temperature as a solid body, thus preventing thermal stress-induced birefringence in

Table 5: Specifications and measurements of the thermal isolation performance.

Quantity	Specification	prior to isolation	w/ isolation
Difference across L2 mount	$< 0.3°C$	$> 20°C$	$0.3°C$
Periscope time constant	$> 8hr$	$0.3hr$	$7.9hr$
Periscope temp slew rate	$< 1.3°C/hr$	$10°C/hr$	$1.7°C/hr$

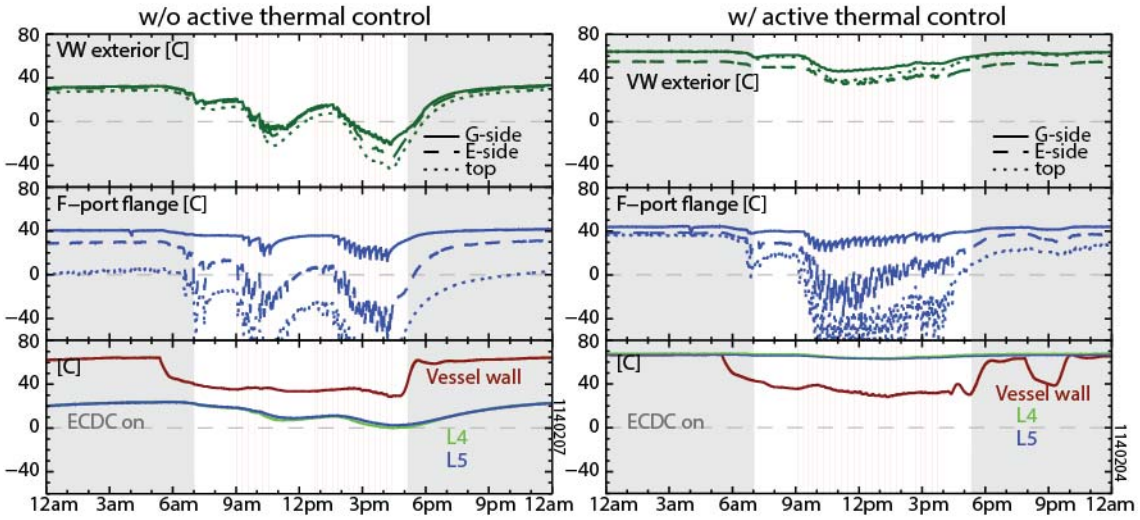

Figure 51: Thermal performance of the active thermal control system on the vacuum window and external periscope. The temperatures are shown with the active system off (left) and on (right).

the internal optics. The low-conduction L2 mounts further decrease any thermal forcing on this important optical element, an effect not included in this analysis.

Figure 51 shows the thermal performance of the active system installed on the vacuum window and external periscope. The system was disabled for a runday (unfortunately causing icing leading to a vacuum leak) to compare performance with (right) and without (left) the active system. The measurements on the top of the vacuum window stack at three locations are shown in the top panel, the measurements at three locations on the exterior of the F-port flange are shown in the middle panel, and the measurements of the vessel wall near MSE and the external optics are shown in the bottom panel. Periods of ECDC are indicated by gray shaded regions and the times of plasma discharges are indicated by vertical lines.

The F-port flange temperatures decrease substantially due to repetitive magnetic cooling during the runday. This decrease is not reproducible day-to-day due to the different cooling needs and leads to large, $> 100°C/m$ thermal gradients in the flange. In the case without active control enabled, this leads to large temperature changes—$>$ 60°C in the vacuum stack—along with large temperature gradients.

The external optics (L4 and L5) also become 20°C colder. In the configuration with the active control enabled, the vacuum window stack undergoes significantly smaller thermal transients, despite the large changes in the F-port flange, though gradients still develop. The external optics remain at a fairly constant temperature. Improvements to the blower system for the FY15 campaign should further enhance the ability to control the vacuum window and external optics temperature by adding heating capability to the F-port flange itself with new blowers and an air distribution system.

BIBLIOGRAPHY

[1] J. Ko. *Current profile measurements using Motional Stark Effect on Alcator C-Mod*. PhD, Massachusetts Institute of Technology, 2009.

5

DEVELOPMENT OF A HIGH THROUGHPUT POLYCHROMATOR

Previous work on MSE determined that partially-polarized background is quasi-broadband in the MSE wavelengths and have described the concept of wavelength-interpolation. A proof-of-principle experiment demonstrated that the polarization properties of the background light are constant as a function of wavelength in the neighborhood of wavelengths used by the MSE diagnostic. The next step is to build an instrument capable of replacing the current MSE detector system with one that can measure the polarization at multiple wavelengths on the same sightline simultaneously. The requirements for such a multi-spectral MSE detector system are:

1. The system should be able to detect three or more different wavelengths on the same sightline, two for proxy measurements, and one or more for MSE measurements.
2. The system should have good spectral selectivity (i.e., it should be able to select a bandpass of $\sim$ 0.5nm FWHM with transmission $>$ 50 percent).
3. The system should discriminate between very closely spaced, and possibly overlapping, spectral regions.
4. The wavelength range for the MSE measurement should be tunable $\pm >$ 0.2nm to allow for changes in beam energy and tokamak magnetic field.
5. The system should have adequate blocking of the bright D_α line (>OD5).
6. The detection system should be compatible with the existing MSE analysis workflow, which uses the PEM harmonics to determine the Stokes vectors.
7. The detector for each wavelength, therefore should be an APD to obtain the required sensitivity and response time to decode the PEM harmonics.
8. The system should be optically fast, allowing the full étendue of the MSE sightline ($\sim$ 9mm^2 sr) to be passed to each detector.
9. The system should be non-vignetting so that the identical bundle of rays are measured by each detector.
10. The system should have high transmission, preferably $>$ 80 percent, between any two wavelength regions.
11. The system will be located in the diagnostic lab, replacing the existing MSE detectors.

12. The system should be compatible with the existing MSE fiber bundles and should not require changes to the upstream optics.
13. The system should be easy to construct and maintain since each sightline requires its own multi-spectral detector.
14. The system should be relatively inexpensive to build, costing no more than twice the cost of the existing single wavelength detector and filter setup.

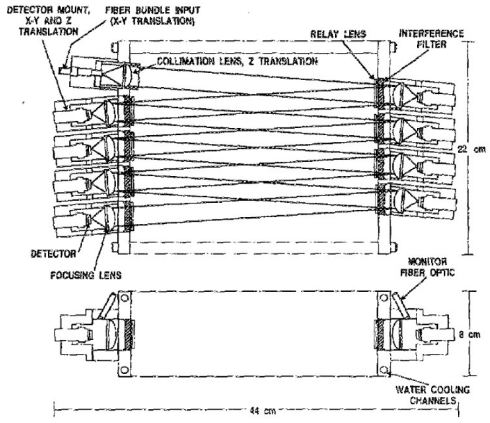

Figure 52: The basic layout for a Thomson scattering polychromator developed for DIII-D and utilized on many experiments. From [1].

Various instrument concepts for spectrally splitting the light were considered. Dispersion-based systems were ruled out due to the need for a such a large étendue, the need to use APD detectors, and the flexibility required to tune the spectral positions. Half-silvered mirrors which were ruled out because of their in-efficient use of photons—they loose a substantial amount of light with each additional spectral bin. Dichroic mirror or beamsplitter-based geometries were ruled out due to their inability to split closely spaced spectral regions. Collecting the light reflected by the filter and using fibers to transfer it to other filters was ruled out because this would have significant vignetting.

The chosen instrument is an interference filter-based "polychromator." This concept, loosely adapted from Thomson scattering systems, uses matched relay lenses and field mirrors to sequentially re-image light from fiber optics placed at an input port through narrow-bandpass interference filters placed within a slightly skewed ($< 5°$) optical cavity. Light within each interference filter passband passes through the filter and is imaged onto a plane at an output port where the APD detector is placed. Light outside each filter passband is reflected from the filter and is re-imaged onto the next interference filter. This is repeated for as many interference filters/detectors as desired by extending the skewed cavity. In this manner, the optical system efficiently transfers the image of the fiber onto each APD with carefully controlled spectral filtering.

Interference filter-based polychromators are often used when large light throughput is needed for measurements in a limited number of spectral bins. In a filter-based polychromator, the input light is sequentially cascaded off of a set of interference filters; each filter passes a chosen wavelength band onto a detector and reflects the remaining light. In fusion research, filter-based polychromators are often used to measure the electron temperature and density in Thomson scattering diagnostics. The typical design has $4-7$ wavelength bins spanning from 700nm to 1064nm with a filter widths varying from $1-3$nm to 50nm. The same basic layout first used on DIII-D [1] has been used on FTU [2], C-MOD [3], HT-7 [4] and HL-2A [5] for many years. This

layout is shown in Figure 52. There is a substantial experience base with the design and operation of these systems that can be utilized for the design of a MSE polychromator.

However, the requirements for a polychromator for MSE-MSLP differ significantly from those designed for Thomson scattering diagnostics for a variety of reasons, each of which leads to a more challenging polychromator design:

- A $5-10\times$ larger étendue is required to obtain acceptable signal from the beam, which requires a much larger physical optical system.
- The filter bandpass must be much narrower to isolate the MSE light; $<$ 0.8nm at 660nm ($\frac{\lambda}{\Delta\lambda} = 825$) vs 3nm at 1064nm to 50nm at 800nm ($\frac{\lambda}{\Delta\lambda} = 354$ to 14).
- As to be discussed, the filter requirements lead to a smaller angle of incidence on the filter (3° vs 5°).
- The filter requirements also lead to a smaller cone angle of the light for similar reasons.
- The filters require a mechanism to tune their center wavelength to match the beam emission.
- The detectors must have higher gain to amplify the very small signals.
- Temporal or spatial multiplexing cannot be used since each sightline has different filtering requirements. Each sightline requires its own polychromator.

5.1 OPTICAL LAYOUT

A study of different polychromator optical layouts was conducted. It was decided that the traditional Thomson layout was inadequate for MSE. An imaging "field mirror-relay lens" system was developed that allows for a large étendue with little vignetting while providing a small angle of incidence on the filters. This system is similar in concept to the "field lens" design proposed for W7-X [6] Thomson system, except the field mirror replaces the field lens, folding the system back on itself so all the filters and detectors are located on the same side of the polychromator. In this way it is similar to the Thomson polychromator used for the C-MOD edge system [7], though with significantly larger field mirrors. The layout is illustrated in Figure 53. The optical design of this field mirror-relay lens imaging polychromator layout is discussed in this section.

The input port of the polychromator, where the MSE fibers are placed, is imaged by the objective lens onto the first field mirror at the far end of the cavity. The concave field mirror, operated off-axis at cavity angle θ, has a focal length that is twice the distance between

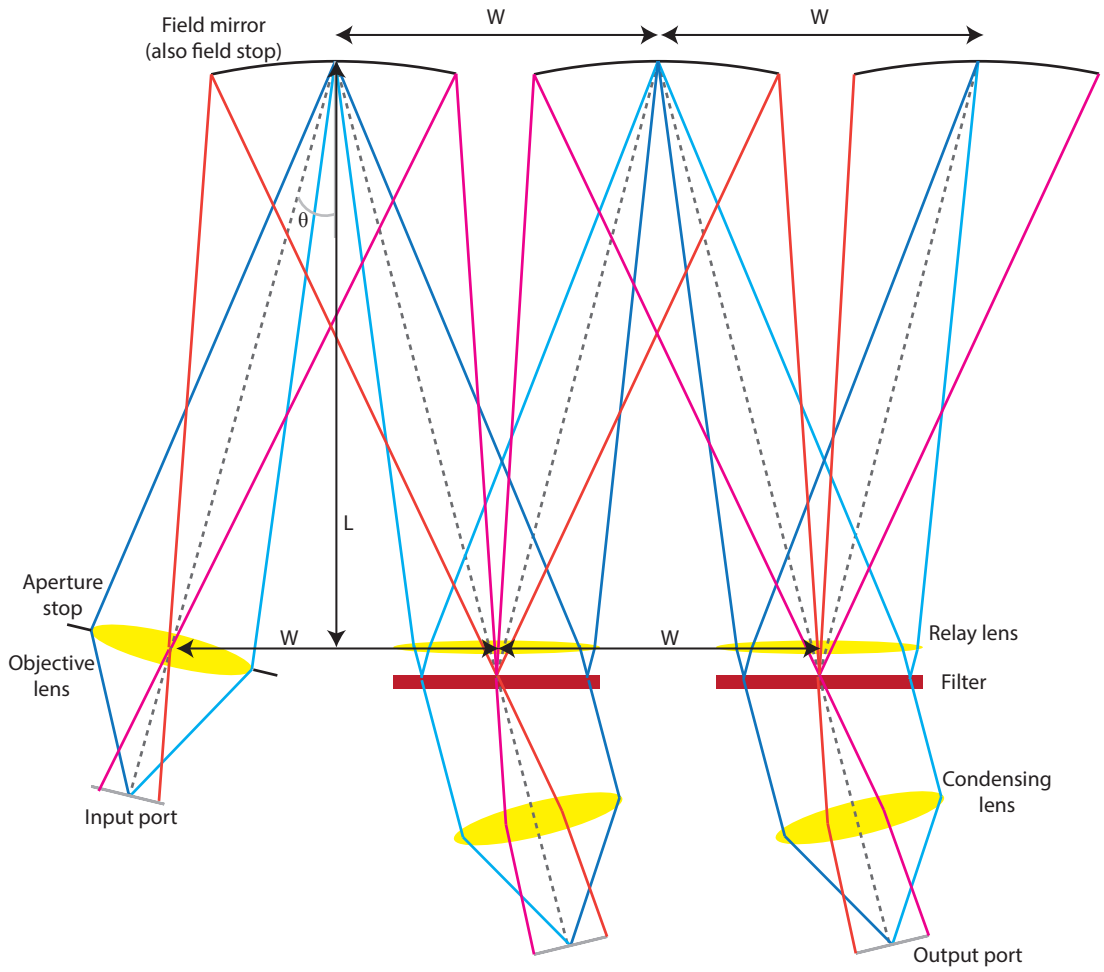

Figure 53: Schematic of a field-mirror relay-lens imaging polychromator. The image of the input port is transfered to each output port via a system of field mirrors, relay lenses, filters, and condensing lenses. The optical axis with a cavity angle of θ is shown in dashed gray, the chief rays are in shades of blue, and the marginal rays are in shades of red. The important physical dimensions are the cavity length L and the cavity width *W*. Note that the light configuration on the third field mirror is identical to that on the first field mirror, thus the cavity repeats and can be extended indefinitely.

the mirror and the objective lens. Thus, the mirror reconverges the light, imaging the objective lens back toward itself but displaced laterally. A relay lens is placed at twice the focal length of the field mirror—coinciding with this displaced image of the objective lens. The focal length of the relay lens is the same as the distance between the lens and field mirror and thus the relay lens collimates the light from the mirror. This collimated light is then incident on the filter, which is placed immediately behind the relay lens.

The collimated light outside the filter passband is reflected from the filter and passes through the relay lens again. The matched focal length ensures the relay lens images the field mirror back onto itself. Since the light was incident on the filter with a mean angle of incidence θ, the image of the field mirror is displaced further down the cavity. If an identical field mirror is placed at this displaced image with angle θ, it will image the relay lens back onto the relay lens but displace it laterally. The entire process can be repeated indefinitely: each field mirror will form an image of the objective lens onto the next relay lens/filter, and each relay lens/filter will form an image of the field mirror (and, as a result, the input port) onto the next field mirror. In effect, the optical axis bounces back and forth between the center of each relay lens/filter pair and the center of each field mirror.

The system consists of two planes forming a cavity. One side of the cavity is a plane with field mirrors all equally spaced at distance W. The other side of the cavity is a plane with relay lenses equally spaced a distance of W, and laterally offset from the spacing of the mirrors by $W/2$. Narrow passband filters are positioned directly behind the relay lenses. The objective lens is on the same plane as the relay lenses, but tilted to be aligned to the optical axis. The focal length of the field mirrors is half the focal length of the relay lens and the spacing between the planes, L, is the same as the focal length of the relay lenses. The geometry of the cavity is then related by $\tan\theta = \frac{W}{2L}$, $f_{\text{relay}} = L$ and $f_{\text{mirror}} = \frac{L}{2}$.

Light within the filter bandpass is passed through the filter rather than reflecting from it, and thus exits the cavity. This collimated light is incident on a condensing lens that is aligned to the optical axis passing through the filter. The condensing lens forms an image of the input port at its focal length. This image location is aligned to coincide with output port of the polychromator for that spectral bin.

Therefore, an image of the input port will be passed down the cavity, and will be repeatedly re-imaged at the field mirrors. Its phase conjugate will be repeatedly re-imaged on each relay lens. Each relay lens will collimate the light onto each filter. The light will be spectrally filtered by each narrow bandpass filter and the image will then be reformed at each output port by the condensing lens.

The objective lens acts as the aperture stop of the system and the field mirror acts as the field stop. It is important that the focal length

of the relay lenses be twice the focal length of the mirrors and equal to the cavity length L to prevent the accumulation of errors in the cavity. In practice, the fact that the field mirrors and relay lenses operate off axis must be taken into account when determining the proper radius of curvature needed to achieve the desired focal length. The objective lens, relay lenses, filters, and condensing lens can all be the same diameter while the field mirror should match the shape of the input port. The filter should be placed immediately behind the relay lens and the condensing lens should be immediately behind that, though construction details limit this in practice.

If the system has properly matched focal lengths, and proper alignment, it will not vignette. This means transmission and reflection at the surfaces are the only losses as the light is transmitted to each filter. A single leg through the cavity—ignoring the filter acting in transmission—consists of a reflection from the filter, a pass through a relay lens, reflection from the field mirror, and a pass through the next relay lens before being incident on the next filter. For high quality lenses with anti-reflective coatings ($R < 0.5\%$ for each surface) and high quality reflective surfaces on the mirrors and filters ($R > 98\%$), the transmission between adjacent output ports should be $T > 0.995^4 \times 0.98^2 > 0.94$, not counting the filter acting in transmission. This is very high, enabling the polychromator to be very photon efficient and to have many output ports. The specifics of this optical layout allow the system to operate at high étendue with a relatively small cavity angle θ, which has important implications for the spectral characteristics which are discussed in the next section.

5.1.1 *Filter considerations*

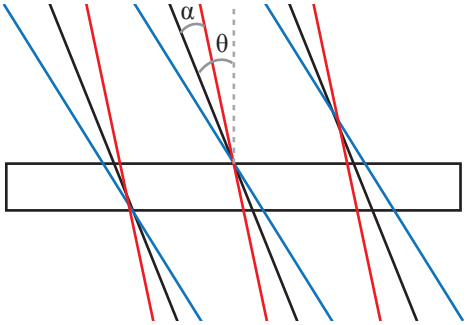

Figure 54: The filter exposed to collimated light from an extended source. Light from the optical axis (black) is incident at a mean angle of incidence θ. Light from the field points (red, blue) is collimated into a converging beam with cone angle α.

The transmission characteristics of an multi-dielectric layer interference filter change depending on the parameters of the filter's illumination. Particularly important are the angle of incidence, the incident cone angle, the filter temperature, and the finite filter illumination size. The effects were explored theoretically by Lissberger and Wilcock [8] and compared to measurements by Blifford [9]. Important results, as they relate to the MSE polychromator, are summarized here.

Because they are interference based, filters are very sensitive to the angle of the rays of light incident on the filter surface. There are two important angles in any real implementation: the mean angle of incidence of the light due to a physical tilt of the filter relative to the optical axis, designated θ, and the cone angle of the light due to a finite beam con-

vergence which occurs in collimated light from an extended source, designated α. The geometry is illustrated in Figure 54.

The center wavelength of the bandpass shifts when the filter is tilted in a collimated beam from a point source:

$$\frac{\lambda_\theta - \lambda_0}{\lambda_0} = -\frac{\theta^2}{2n_{eff}^2} \tag{8}$$

Where λ_θ is the new center wavelength, λ_0 is the original center wavelength, n_{eff} is the effective index of refraction in the filter (1.5-2.5) and θ is the angle of incidence on the filter in radians. The negative sign indicates the filter bandpass shifts to the blue when the filter is tilted. Note the small angle approximation is used here. This angle of incidence dependence is often used to tune the filter's characteristics by tilting it relative to the optical axis.

However, this is not the only modification that occurs when the filter is tilted, the width of the bandpass is also modified:

$$\frac{\Delta\lambda_\theta}{\Delta\lambda_0} = \sqrt{1 + \left(\frac{\theta^2}{n_{eff}^2}\frac{2\lambda_0}{\Delta\lambda_0}\right)^2} \tag{9}$$

Where $\Delta\lambda_\theta$ is the new full-width half max, and $\Delta\lambda_0$ is the full-width half max under normal angle of incidence. Notice the width increases as the filter is tilted. There is a strong dependence on both the angle of incidence and on the narrowness of the original bandwidth ($\frac{\lambda_0}{\Delta\lambda_0}$). The second dependency means this broadening can be a large deleterious effect for ultra narrow bandpass filters, doubling the width of the filter in a moderate, $\sim 5°$, tilt. It has also been shown experimentally that the maximum transmission decreases with filter tilting in a manner proportional to $\frac{\lambda_0}{\Delta\lambda_0}$. Many existing MSE systems use filter tilting to tune the filter bandpass center wavelength and tolerate the deleterious effects. However, tilt-tuning of filters is obviously not viable in a polychromator as any changes would impact overall geometry.

In an analogous manner, illuminating the filter with a converging beam of light creates similar effects depending on the cone angle of the light, α. The shift in center wavelength due to a converged beam with a normal angle of incidence is:

$$\frac{\lambda_\alpha - \lambda_0}{\lambda_0} = -\frac{\alpha^2}{4n_{eff}^2} \tag{10}$$

The change to the bandpass width due to a converged beam with a normal angle of incidence is:

$$\frac{\Delta\lambda_\alpha}{\Delta\lambda_0} = \sqrt{1 + \left(\frac{\alpha^2}{2n_{eff}^2}\frac{2\lambda_0}{\Delta\lambda_0}\right)^2} \tag{11}$$

Note that these effects are less of an issue for a cone angle than a mean angle of incidence of the same value due to averaging effects; a mean angle results in all rays incident at θ and a cone angle results in some rays incident at α, but most rays incident with a smaller angle. The change in maximum transmission (T) due to a converged beam with a normal angle of incidence is:

$$\begin{aligned}\frac{T_\alpha}{T_0} &= \frac{1}{\gamma}\arctan(\gamma) \\ \gamma &= \frac{\alpha^2}{n_{eff}^2}\frac{2\lambda_0}{\Delta\lambda_0}\end{aligned} \tag{12}$$

In real systems with a converging beam with a non-normal angle of incidence, the various effects are combined. Furthermore, the bandpass filter is usually non-homogenous across its surface due to slight errors in fabrication. This creates a passband that can be spatially dependent and the effective passband differs if averaged over different areas of illumination. These combined effects are present for the case for the situation shown in Figure 54 and in the filter-based polychromator. A study of these filter effects and efforts to compensate for them in a real implementation can be found in Ref [10]. Fortunately, heating the filter has very little effect on the filter characteristic except to shift the center wavelength to the red. This effect is linear across a wide temperature range, making temperature tuning an ideal method to tune filters if precision measurements are required [9].

To characterize these effects in the MSE implementation, a test was carried out with the MSE filters illuminated under different angles of incidence. The filter was tilted inside the filter oven and exposed to the typical illumination pattern from the MSE system. The passband was measured using a high resolution spectrometer after first collecting the filtered light in an integrating sphere. The results are shown in Figure 55. Panel (a) shows the measured filter bandpass as the filter is tilted. The manufacturer measurement of the filter under normal incidence with only a small, highly collimated beam is shown as the dashed line. It is apparent that the filter bandpass shape degrades significantly, even at small angles, as the filter is tilted; the transmission decreases, the width increases, and the passband shifts to the blue. A Gaussian fit was performed to the filter transmission curves to quantify changes to the filter parameters. The results of the fits are shown in panels (b) through (d) with linear fits to the param-

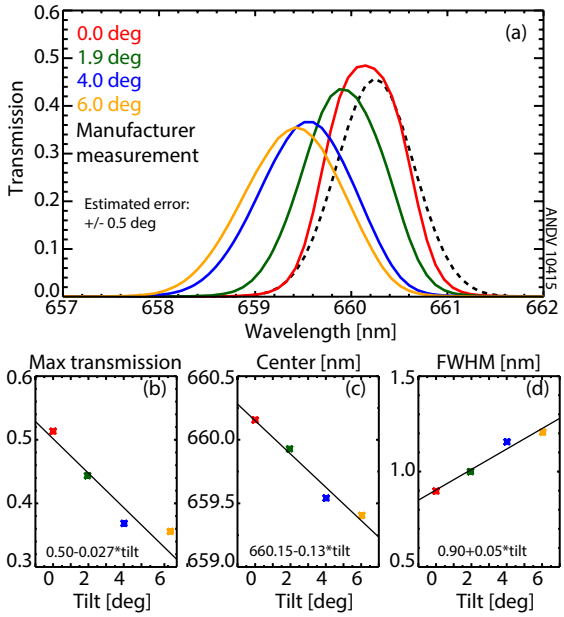

Figure 55: The effect of filter tilting on the filter bandpass shape for MSE filters measured in-situ in a filter oven. The measured filter passband (a). Parameters from a Gaussian fit to the transmission (b)-(d).

eters. The linearity differs from the quadratic expectations from the preceding theoretical treatment. However, the experimental data reproduces the qualitative trend of degraded filter parameters as the filter is tilted and the quantitative agreement to theory is fairly good in the tilt range of $3-5°$. Note substantial uncertainties in the angle of the tilt remain due to experimental setup and that the effective index of refraction is unknown.

In summary, the filter design places three key implications on the layout of a high throughput, high spectral resolution, filter-based polychromator:

1. The angle of incidence θ of the filter relative to the optical axis, i.e. the cavity angle, should be minimized.

2. The cone angle of the light incident on the filter should be minimized, though this is a less significant effect.

3. The filter passband should be measured in-situ in illumination conditions as similar to the operating scenario as possible in order to obtain its bandpass characteristics for use in tuning the filter and interpreting results.

The importance of these issues increases as the filter bandpass gets narrower relative to its center wavelength. Unfortunately, the first two implications have lower limitations in a polychromator; a nonzero angle of incidence θ is necessary to bounce the light down the cavity, and a non-zero cone angle α is required for anything other than a point source. These two angles are tied to the étendue that can be cascaded down the polychromator. This will be discussed in the next section.

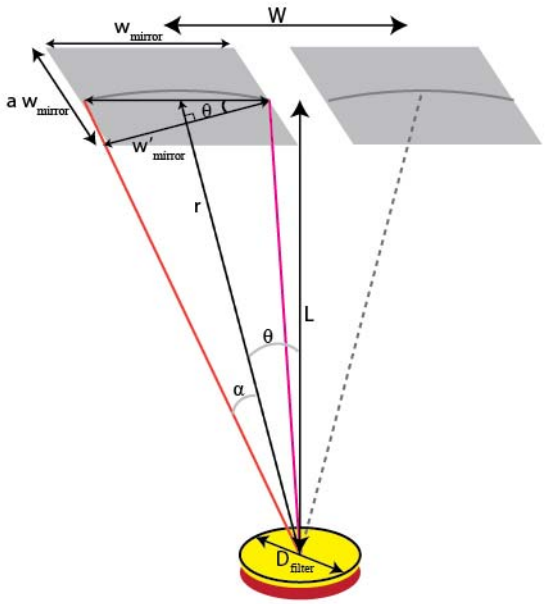

Figure 56: The geometry to calculate the étendue that the relay system can pass.

5.1.2 *Etendue considerations*

The goal of the polychromator is to properly filter a large amount of light at minimal cost. Therefore, the étendue of the field mirror-relay lens combination is of primary concern. A section of this cavity is shown in Figure 56 which illustrates a relay lens/filter combination and the proceeding and following field mirrors. The mirrors are rectangular with width w_{mirror} and height $a \times w_{\text{mirror}}$. The filter has a clear diameter of D_{filter}. The étendue of this configuration is therefore:

$$\epsilon = A_{\text{filter}} \cos(\theta) \Omega_{\text{mirror}} = \frac{\pi D_{\text{filter}}^2}{4} \cos(\theta) \Omega_{\text{mirror}} \tag{13}$$

Where the solid angle subtended by the mirror, Ω_{mirror}, is:

$$\Omega_{\text{mirror}} = \frac{a\, w'^2_{\text{mirror}}}{\left(r - \frac{w_{\text{mirror}}}{2} \sin(\theta)\right)^2} \tag{14}$$

The cone angle α is related to these quantities:

$$\tan \alpha = \frac{w'_{\text{mirror}}}{2\left(r - \frac{w_{\text{mirror}}}{2} \sin(\theta)\right)} \tag{15}$$

Putting it all together yields:

$$\epsilon = \pi D_{\text{filter}}^2\, a\, \cos(\theta) \tan^2(\alpha) \tag{16}$$

Thus, to maximize the étendue through the cavity, it is advantageous to use a larger filter diameter, to minimize the cavity angle θ, and to maximize the cone angle α. However, $\max(\alpha) = \theta$, otherwise the in-

termediate images overlap on the field mirrors, effectively vignetting those regions. It is therefore desirable to make α as close as possible to θ. The physical implications of this are: (1) the field mirrors should cover nearly the entire spacing on the far cavity plane ($w_{\text{mirror}} = W$), (2) the intermediate images should fill these mirrors. Note that elongating the field mirror vertically can increase étendue while leading to smaller detrimental effects on the filter properties than simply making the mirror wider. Setting $\alpha = \theta$ yields an étendue:

$$\epsilon_{\alpha=\theta} = \pi D_{\text{filter}}^2 \, a \, \tan(\theta) \sin(\theta) \tag{17}$$

When designing for a desired étendue, the trade-off is between how large the filters can be made ($) versus how much filter degradation can be tolerated by increasing θ and α. Notice that nowhere in this analysis did the cavity length or spacing come into play as this does not set the étendue directly. However, the spacing W must be greater than the total filter diameter and needs to be sufficient in order to include any hardware surrounding the filters (such as ovens) or the width of the detectors.

Once the cavity properties are determined, the objective lens focal length should be chosen so that the image of the input port fills the field mirror when the objective lens is located on the same plane as the relay lenses. Therefore, the choice of this lens depends on the desired size of the input port and its input numerical aperture (NA). The condensing lens should be chosen so that the image formed at the output port is the correct size for the detector or the desired output NA. The magnification between the input port and output port is then:

$$M = \frac{h_{\text{output}}}{h_{\text{input}}} = \frac{NA_{\text{input}}}{NA_{\text{output}}} = \left(\frac{1}{f_{\text{obj.}}} - \frac{1}{f_{\text{relay}}} \right) f_{\text{cond.}} \tag{18}$$

5.1.3 *Final optical parameters*

The cavity was optimized to provide a sufficient throughput to accept all the light from the fibers for a single MSE sightline, at as small a cavity angle as possible, with adequate cavity spacing to provide enough room for filter ovens. The objective lens, condensing lens, and relay lens are 50.8mm to allow off-the-shelf purchasing of these components. The 50.8mm diameter filters are filled with a beam diameter $D_{\text{filter}} = 40\text{mm}$ to prevent vignetting by the relay lens and condensing lens.

The cavity angle θ_{cavity} was chosen to be 3° to provide adequate étendue and preserve filter bandpass shape. Using a typical $n_{\text{eff}} = 2.0$ and $\frac{\lambda_0}{\Delta\lambda_0} = 825$, this tilt yields a theoretical shift of 0.17nm and a broadening of the passband by 1.3× compared to a filter operated

at normal incidence. These are deemed acceptable for the MSE implementation.

The cavity must provide sufficient space for the filter ovens surrounding the filters, which ultimately sets the cavity's physical size. A cavity length of $L = 750$mm was chosen to allow the use of off-the-shelf relay lenses. This gives a cavity spacing of $W = 78.6$mm, which is large enough to hold the 76mm diameter filter ovens with structural space between them. There are four cavity legs in the polychromator, though more could be added.

To match the cavity length, the field mirrors have a radius of curvature of $R_{curve} = 768$mm, requiring them to be custom fabricated. They are spherical to minimize cost. The field mirrors are extended in the direction perpendicular to the cavity plane; the diameter of 114.4mm is truncated to a 76mm width. This gives a cone angle of 2.9° and the usable rectangular area on the mirror has an aspect ratio $a = 1.2$. Therefore, the cavity can pass an étendue of 15.5mm²sr. The cavity can relay 18.3mm²sr if the top and bottom portions of the field mirror are used. For reference, the typical Thomson scattering polychromator can relay 1 to 3mm²sr.

Each MSE sightline consists of 16 $NA_{fibers} = 0.37$ fibers, each with 1mm core diameter. The periscope under-fills the fibers at $NA_{input} = 0.30$, and tests confirm that the fibers preserve this NA fairly well over their short length. Therefore, the fibers produce an étendue of $\epsilon_{fibers} = n_{fibers}\frac{\pi^2}{4}d_{fibers}^2 NA_{input}^2 = 3.6$mm²sr. However, the fibers have an outer diameter of 1.1mm due to their cladding, and are circular, limiting their packing. Therefore, they are arranged into a 4×4 hexagonal packed orientation within a 6.3mm tall by 5.0mm wide rectangle. In this configuration, the input port fills 8.9mm²sr, well within the capacity of the cavity relay system.

A 62.9mm focal length objective lens is chosen to accept $NA_{inpupt} > 0.3$. The lens under fills the field mirror leading to an actual cone angle of $\alpha = 2.3°$. This provides adequate margin for vignetting and makes the fiber layout the effective field stop. The condensing lens is chosen to be a strongly focusing asphere with focal length of 32mm. This produces an image at the output port with a magnification of 0.46 at a large NA_{output}. The 2.9×2.3mm output image fits well within the desired 5mm APD diameter.

The parameters for the optical components are shown in Table 6. The only custom optical components are the bandpass filters and the field mirrors. By the time the rays reach the fourth APD, they have undergone 55 optical transitions (30 in the periscope and 25 in the polychromator) and 10 reflections (three in the periscope and seven in the polychromator). Therefore, all the lenses have anti-reflection coatings optimized for the $600 - 700$nm region and the mirrors and filters are specified to be highly reflective. The relative transmission between the fiber output and the four output ports measured in-situ

Table 6: The finalized polychromator optical parameters.

Component	Description	Size	Property
16 × 1mm dia. fibers	at input port	close packed within 6.3 × 5mm	NA = 0.37, filled at NA = 0.30
Objective lens	plano-convex	50.8mm dia.	f = 62.9mm
Aperture stop	at objective lens	40mm dia.	
Field mirror	spherical concave	114.4mm dia.×76mm wide	R_{curve} = 768mm
Relay lens	plano-convex	50.8mm dia.	f = 750mm
Filter	narrow bandpass	50.8mm dia.	
Oven window	high transmission	50.8mm dia.	
Condensing lens	convex-asphere	50.8mm dia.	f = 32mm
Filtered image	at output port	~ 2.9 × 2.3mm	NA = 0.64

(with mirrors instead of filters) is 0.93, 0.89, 0.85, 0.80. The low ~ 4 — 5% loss on each leg demonstrates that low reflection and transmission losses are indeed achieved.

The optical layout was fine-tuned in the ray-tracing program OSLO to aid in optimizing the component locations and spacings and to verify that the polychromator would meet its goals. The resulting layout is shown in Figure 57. The fiber orientation is shown in panel (a). The field points are launched at the widest part of the fiber and fill the objective lens at NA_{input} = 0.3. Close-ups of the input port and objective lens (b), relay lens and filter (c), and condensing lens and output port (d) are shown.

Panel (d) shows this system is close to imaging, though with significant aberrations. There is substantial spherical aberration due to the high power of the objective lens and condensing lens. The long focal lengths of the relay lens and field mirror do not substantially contribute to the spherical aberration. However, a decentering distortion and tilt aberration arise because the filter is slightly behind the relay lens and the lens is tilted relative to the optical axis. Additionally, the intermediate images are not formed on the field mirror surface. One side of the image is slightly in front of the surface and the other side is slightly behind the surface, therefore the field mirror is not a true field element for all field points. All of these relay system aberrations are minimized as the angle of incidence is decreased, further motivating a small cavity angle. Additionally, the layout does decrease these aberrations somewhat since the images "flip" side-to-side and top-to-bottom after each pass through the cavity, as can be seen by tracing any of the off-axis field points through the cavity in Figure 57. This "flipping" leads to some cancel-

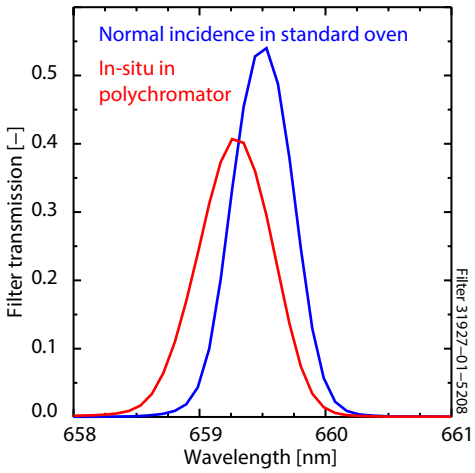

Figure 58: The polychromator's effect on filter bandpass shape compared to the existing system.

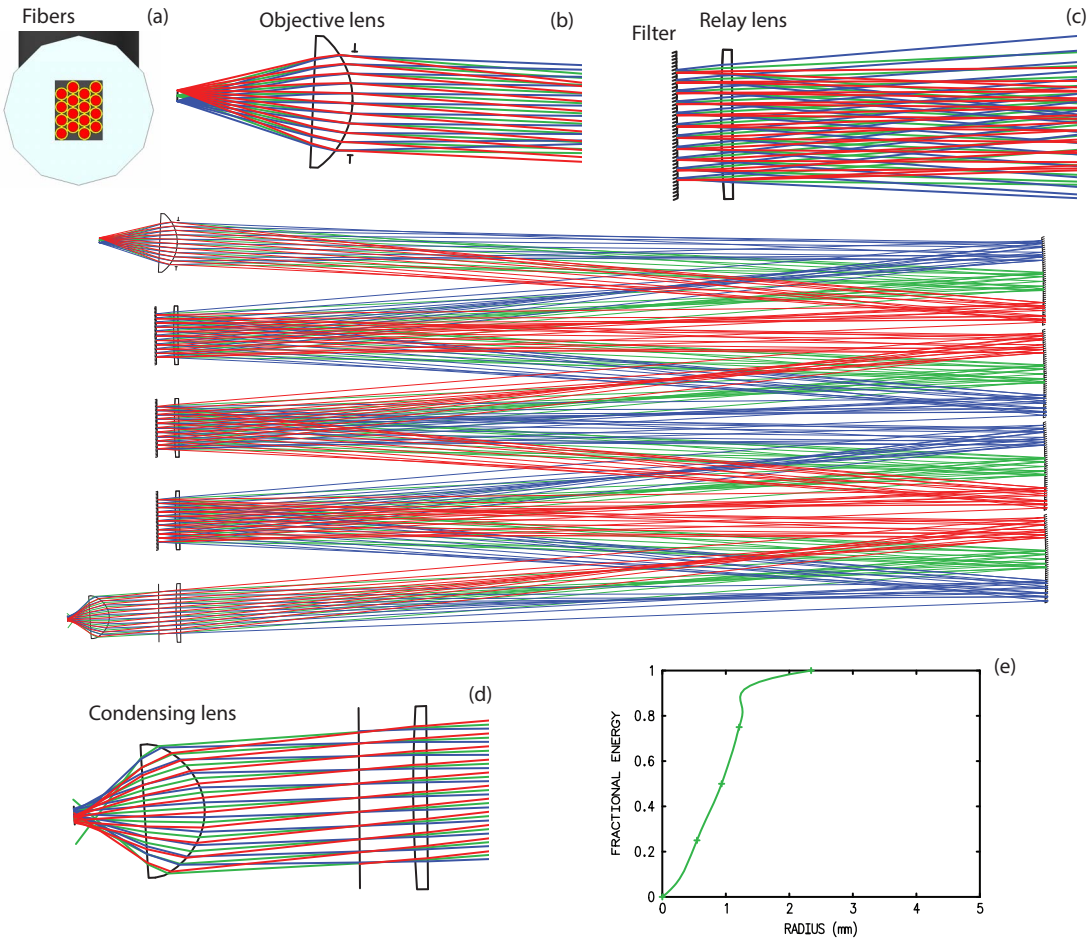

Figure 57: Ray-tracing program (OSLO) output showing the ray trajectories of the optimized polychromator. The important regions of the polychromator are shown in detail. The energy spread at the output port from a point source at the input port is shown as an inset.

lation of aberrations. If the polychromator were operated over a wider wavelength range, the objective lens and relay lens would introduce some chromatic aberration. The field mirror and condensing lens do not contribute to chromatic aberration because they are a mirror and operate on nearly monochromatic light respectively. The aberrations cause rays from a point source at the input port to spread their energy over a 1.5mm radius at the output port as seen in Figure 57 (e). This is not a concern for the MSE application because the vast majority of the energy is still contained within the APD detector diameter.

Overall, this system is capable of efficiently transmitting the light from the MSE fibers to the different filters in a manner that doesn't significantly degrade the spectral resolution. A head-to-head comparison between the filter bandpass under normal incidence in the existing filter oven system and the same filter measured in-situ in the polychromator is shown in Figure 58. Even when tilted, the filter bandpass will adequately select the MSE σ or π triplets.

5.2 OPTO-MECHANICAL DESIGN

Since the optical system is a repetitive cavity that requires precise alignment of two planes (the mirrors and filters), the decision was made to proceed straight to mechanical construction instead of prototyping the system on an optical bench where there would be many degrees of freedom. The polychromator mechanical design places the optics in the correct positions and orientations. This is done by extracting the spacings and locations from the OSLO model of the polychromator and using them as a template in the solid modeling program. The mechanical components are designed so that they can be easily machined at a relatively low cost, are fabricated from aluminum, and are black anodized to prevent stray reflections. To lower cost, off-the-shelf optical adjustments and mounts were incorporated where possible. The major mechanical and optical components are identified in Figure 59. Photographs of the machined elements before assembly and of the fully assembled prototype polychromator are shown in Figure 60. One important mechanical challenge was to design a device with the means to make necessary fine adjustments while still being robust enough to ensure the optical layout stays properly configured over years of use. The details of the opto-mechanical design, including the adjustment capabilities, are shown in Figure 61 and are discussed in this section.

The "main mount" is the primary component on the filter end of the cavity. This element houses the filters and the objective lens. It holds the four "detector limbs" that contain the condensing lens and upon which the detectors are mounted. The main mount also supports the "fiber limb" which holds the input port which interfaces with the MSE fiber. The filter ovens and plugs fit into holes in the

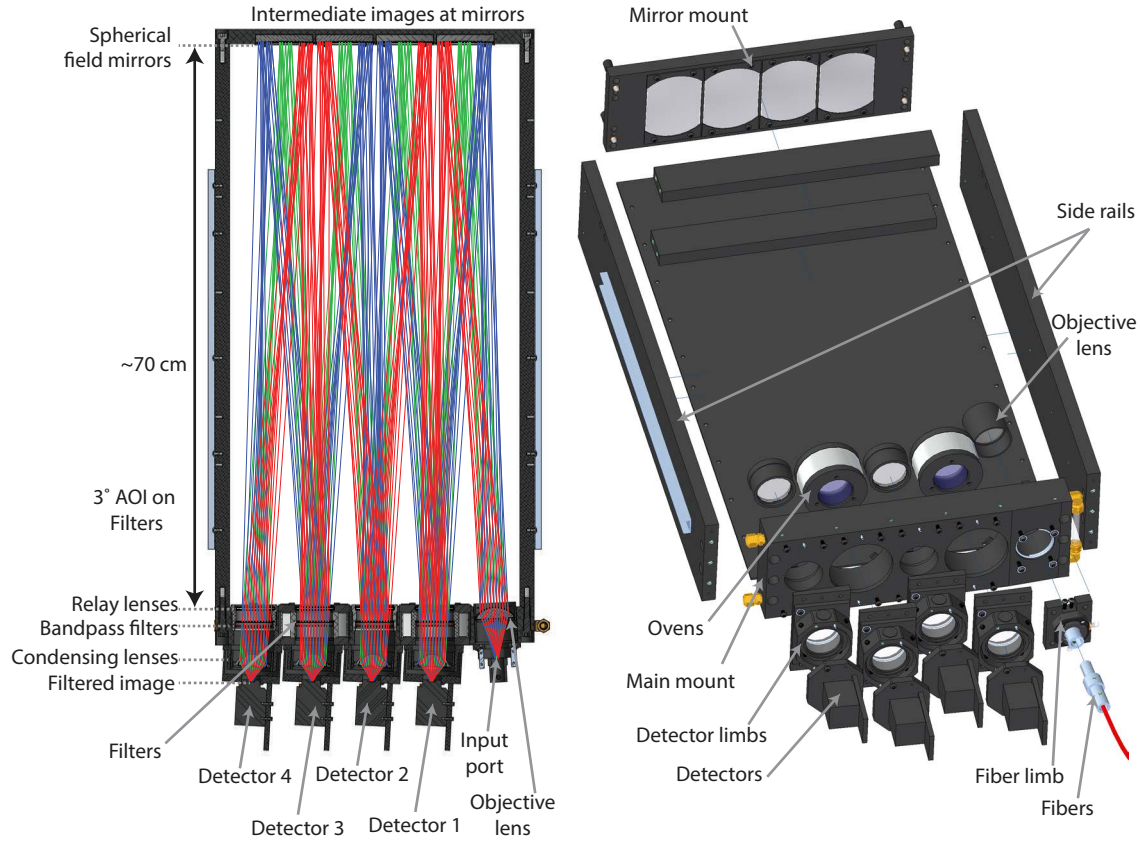

Figure 59: The opto-mechanical design of the polychromator. The major optical components are labeled (left). The mechanical components that hold and align the optical components are labeled (right).

Figure 60: Photograph of the anodized prototype polychromator components prior to assembly (left) and fully assembled (right).

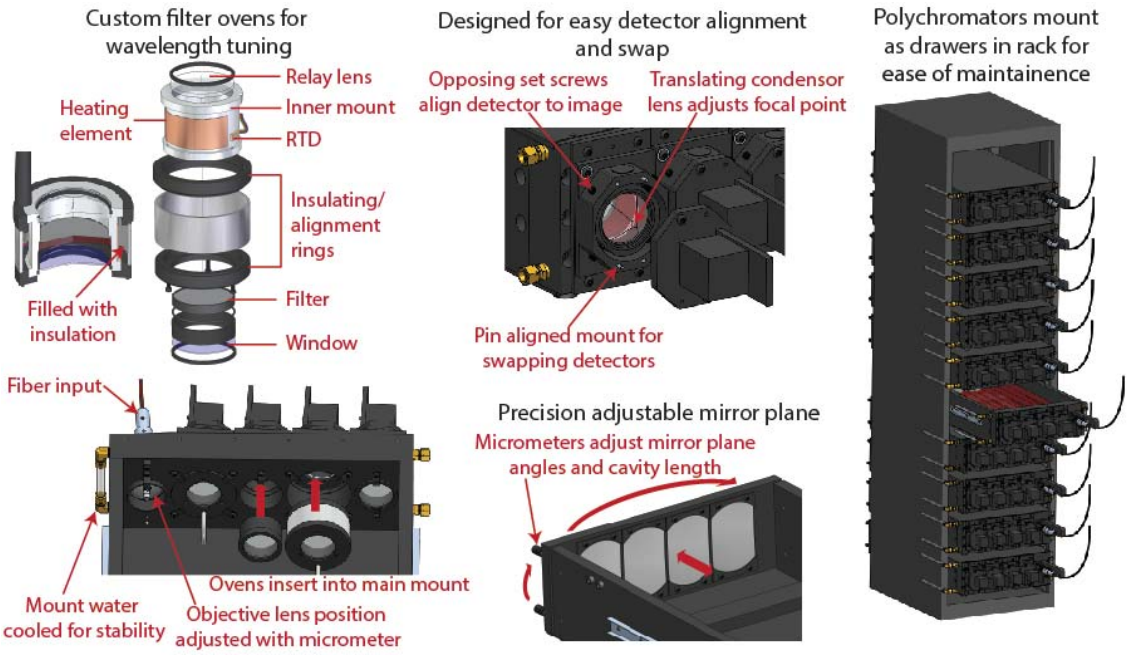

Figure 61: Key opto-mechanical details of the polychromator design to aid in the alignment, operation and maintenance of the optical system.

main mount and are held in the holes with small clamps that allow the ovens and plugs to be easily removed from inside the cavity without tools. The filter ovens are aligned to the proper cavity plane using the back face of the oven on the back face of the main mount. They are held in the correct position perpendicular to the optical axis by the fit between their outer diameter and the main mount's inner diameter. The main mount is water cooled to remove the excess heat from the filter ovens and to provide a stable temperature environment for the detectors, which are thermally sunk to the mount via the detector limbs. The entire cavity can be reversed so the input port is on the left or right side of the main mount.

The main mount is machined so that the fiber limb is aligned to the 3° tilt of the optical axis. The location of the fiber on the input port plane is adjusted in the directions perpendicular to the optical axis using an off-the-shelf 2-translational axis kinetic mount. The keyed fiber ferrule plugs into this kinetic mount and is secured with a set screw. The objective lens is mounted in an off-the-shelf lens tube that is inserted in a hole through the main mount along the optical axis, and the position of the objective lens along the optical axis is controlled using a micrometer acting against a spring.

Behind each filter oven or filter plug is a detector limb. The detector limb base is pin-aligned to the main mount and is machined to provide the 3° tilt that is necessary to align the condensing lens and detector to the optical axis passing through the filter. The condensing lens is mounted in an off-the-shelf lens tube that is inserted into a

hole in the fiber limb base. The lens tube is free to translate along the optical axis, is spring loaded, and is secured with a set screw. The detector mount is placed over the detector limb base and is free to translate in the two directions perpendicular to the optical axis. This translation is controlled using two sets of opposing set screw pairs in a similar manner to the mechanism on the DIII-D polychromators [1]. The detector limb mount has pins which mate to the detectors or to other alignment and calibration tools.

Two side rails are pin-aligned to the main mount and support the mirror mount on the opposite end of the cavity. To create the correct optical path through the cavity, the side rails are precisely machined to place the mirror mount at the proper distance and position. The mirror mount planar aligns the four mirrors, each held in a pocket using plastic retaining clips. The assembly is aligned to the side rails via pins that allow the mirror mount to pivot on two axes and to translate toward and away from the main mount, but constrain motion in the other three dimensions. The position and orientation of the mirror mount relative to the side rails is adjusted using fine-threaded micrometers that push against tension springs as is typical in optical mounts.

The cavity is squared using braces between the side rails at the mirror mount end and a bottom cover that is fastened to the bottom of the side rails. A removable top cover encloses the cavity to prevent light and dust ingress. Slides mounted to the side rails allow the entire polychromator to be mounted in a standard equipment rack and to slide out like a drawer for servicing. In this manner, many polychromators can be mounted in a single rack one above another to save floor space.

5.2.1 *Oven design*

The filters are contained in ovens or unheated plugs. The relay lens and a clear window are mounted on opposite ends of the aluminum inner mount and create an enclosed space that envelopes the filter in the center of the mount. The space between the filter and relay lens is minimized to reduce decentering distortion while still providing a large enough air pocket for uniform heat transfer. A 440Ω Kapton resistance heater and RTD temperature sensor are glued to the outside of the inner mount to regulate its temperature. The inner mount connects to two plastic (Derlin) insulating/alignment rings that interface with the main mount and support the oven outer cover. The space between the inner mount and outer cover is filled with fiberglass insulation. The filter, window, and relay lens are secured using off-the-shelf retaining rings that thread into the aluminum inner mount, requiring a single tool for servicing. The unheated plugs are constructed sim-

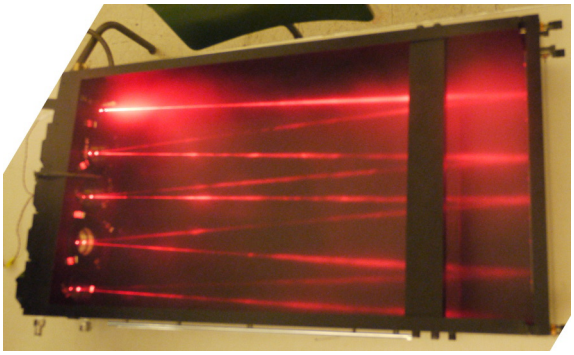

Figure 62: A long exposure showing a laser tracing the optical axis through the polychromator. The laser enters the at the input port on the top left. Photo credit: Dan Brunner

ilarly to the oven inner mount, but consist of only a filter and relay lens.

Each oven is temperature-controlled using a commercially available programmable process controller with PID logic that switches the 120VAC to the heaters. The 32W of power supplied to each oven heats it at approximately 10°C/min. The ovens reach temperatures of ~ 120°C at full continuous power. This is well within safety limits, making the system fail safe. The custom filter ovens and associated control hardware are easy to manufacture, assemble, and control and are < 20% of the cost of the commercial filter ovens used in the existing MSE system.

5.2.2 *Alignment procedure*

The alignment procedure is intended to create the skewed optical cavity so that the optical axis strikes the center of each mirror and filter as shown in Figure 62. The procedure also aligns each detector to the image of the fiber at the output port. The alignment of the polychromator is aided by placing targets at the various intermediate and output images throughout the device. The machining of the components is precise enough for the system to be in good alignment when first assembled, only requiring fine adjustments. The alignment procedure is shown in Figure 63. An LED-illuminated fiber bundle in the configuration of the MSE fibers is used to launch light through the cavity. The first operation is align the cavity:

1. The objective lens is adjusted in and out until a sharp image is formed on the first field mirror.

2. The input port location is adjusted so this image is centered on the first field mirror. The images on the remaining mirrors should be nearly equally spaced.

3. A transparent alignment mask is placed at the objective lens. The angles of the mirror mount are adjusted so that the image of this alignment mask is centered on each of the relay lenses.

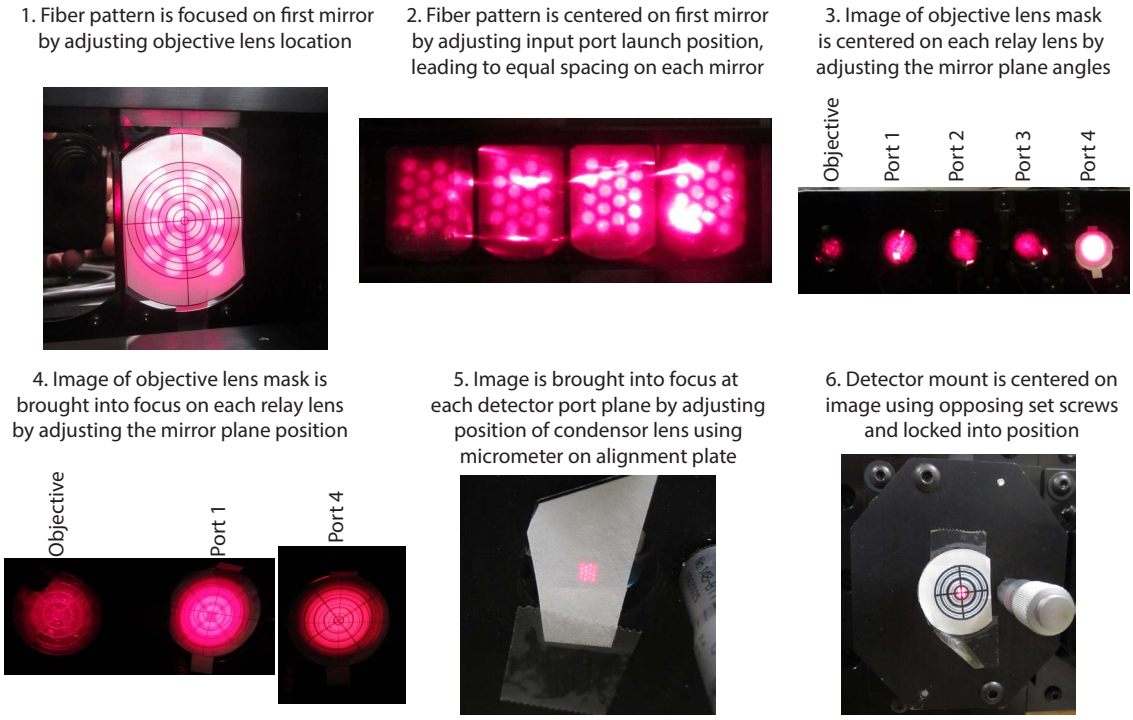

Figure 63: The alignment procedure to set up the optical cavity (steps 1-4) and properly align the detectors to the filtered images (steps 5 & 6).

This ensures that the mirror plane is parallel to the relay/filter plane, eliminating vignetting.

4. The entire mirror mount is translated toward and away from the filters so that the image of the alignment mask is equally in focus at each relay lens. This ensures that the mirror and filter planes are at the optimum spacing.

This process may need to be repeated until a good cavity alignment is achieved. Once this is done, all the adjustments are secured using set screws and lock nuts to keep the cavity aligned, and all alignment masks are then removed.

When the cavity is aligned, filtered images will be produced at each output port. The next procedure is to align the detector limbs so that each detector is centered on the focus of these filtered images:

5. An alignment tool with a micrometer is attached to the detector mount (in place of a detector). The micrometer is used to adjust the condensing lens in and out along the optical axis to bring the filtered image to a sharp focus at the output port plane. The condensing lens is then locked into place with a set screw.

6. The two screws that secure the detector mount to the detector limb base are loosened. The two bottom set screws on the detector mount are backed out a few turns. This allows the mount

to be translated perpendicular to the optical axis using the top two set screws. The mount is adjusted with the set screws until the image is centered on the alignment tool, at which point all the set screws and attachment screws are tightened. This guarantees that when the detector is mounted in place of the alignment tool it will be centered on the image at the output port.

Once this is completed for each output port, the polychromator is properly aligned. The keyed MSE fiber can be replaced at the input port and detectors installed at the output ports. Experience shows that the system stays aligned even through bumps and jostles. Furthermore, the filter ovens can be removed, the filters replaced, and the ovens reinserted without degrading the alignment.

5.3 10 SIGHTLINE SYSTEM

The success of the prototype polychromator led to the development of a full 10 sightline multi-spectral detection system for the C-MOD MSE diagnostic. This system consists of ten polychromators constructed similarly to the prototype system, each with four detectors and four filters. In addition to the construction of the polychromator hardware, a significant effort was spent developing filter specifications, new detectors, and a system to control the hardware. Future work will include improvements to the MSE analysis codes to utilize the wavelength interpolation scheme on a regular basis.

5.3.1 *Changes from the prototype*

Overall, the opto-mechanical design of the prototype was very successful, providing robust optical alignment and ease of use. Thus, only minor changes were required for the second generation system:

- Each polychromator now uses four smaller filter ovens instead of the two ovens and two plugs in the prototype. This increases flexibility and simplifies construction. The ability to tune the filters decreases the cost of specifying filters precisely.
- The oven design was modified with a more robust filter holding mechanism and its assembly was simplified. New clips and connectors allow easier oven installation/removal from the main mount.
- The adjustment system for the mirror plane was changed from a 4-contact system to a 3-contact system for better kinematics.
- The condenser lens was changed from a $f = 37$mm asphere to a $f = 32$mm bi-convex asphere which allows for a smaller APD size, and thus cheaper APD.

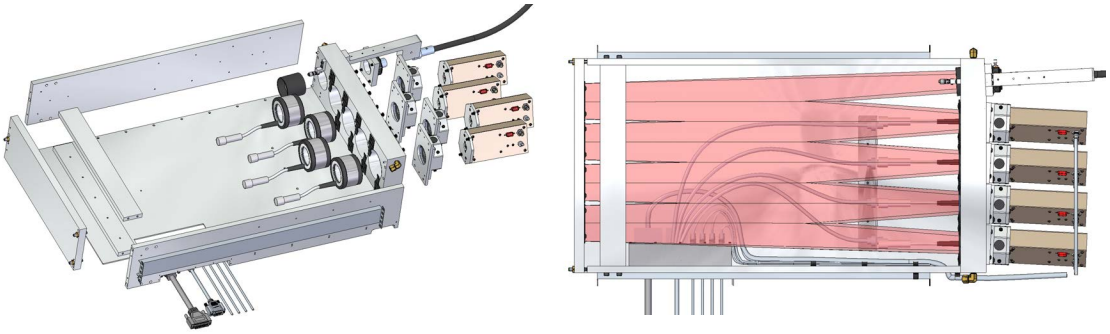

Figure 64: The second generation polychromator design. Showing the light path (right) and an exploded view with the various components (left).

- The cavity's structural components were simplified and made thinner to save material and machining costs.
- The required cabling is now an integral part of the design to simplify installation and maintenance. Each polychromator requires only 2 D-sub connectors (one for the ovens and one for the detectors) and 4 BNCs (one for each detector signal) to control all four detectors and four ovens and to carry the signals. This is a 40% decrease in cables and connections.

These changes led to a lighter, more robust, easier to align and service polychromator that could be easily replicated 10 times. The revised polychromator opto-mechanical design is shown in Figure 64.

5.3.2 *Filter design*

Each polychromator requires four narrow bandpass interference filters. Two of these are used to isolate each of the MSE σ and π multiplets and two are used for the background proxy measurements. The MSE filters are different for each sightline due to the different Doppler and Stark shifts. These filters must be temperature-tuned to follow changes in beam voltage and/or tokamak magnetic field. The proxy filters can be the same for each sightline, thus they can be procured in batches. The proxy filters are still kept in ovens to provide fine tuning to avoid impurity lines and to increase the tolerance on the challenging filter fabrication. The filters are manufactured to achieve their specified bandpasses when operated at 3° angle of incidence with a 2.3° cone angle of collimated light (i.e. light incident from 0.7° to 5.3°). The filters are three cavity designs that produce a bandpass shape with a "flat top." An important consideration for the filters is the parallelism between the filter surface and the outer mounting ring since this ring is used to align the filter in the oven and thus to align the filter to the cavity plane.

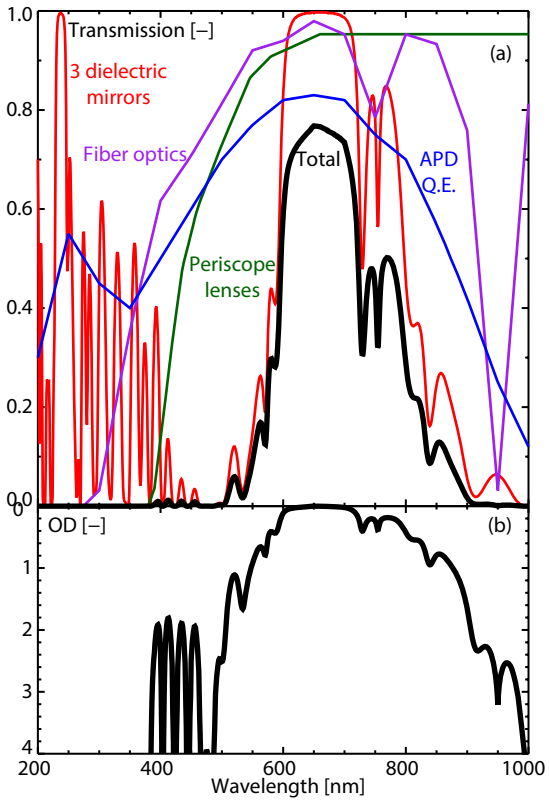

Figure 65: The calculated transmission of the different optical components in the MSE periscope as a function of wavelength (a). The total represents the transmission of the mirrors (red), fibers (purple), lenses (green) and the APD quantum efficiency (blue) multiplied together. Reflection losses from surfaces have been ignored for these calculations. The blocking in terms of optical depth is shown in (b).

An important aspect of the filter is its blocking: how strongly the filter attenuates light outside its bandpass. The MSE system requires a blocking of at least OD5 (10^{-5}) across the entire spectrum. Fortunately, the MSE optical system provides some of this blocking, allowing for a reduced filter design specification. The transmission and blocking of the optical system prior to the filters is shown in Figure 65. It is apparent that significant extra blocking by the filter is required only in the 600nm to 900nm range. Additionally, it is important to block the bright D_α line that is near the MSE wavelengths. The additional blocking required to be provided by the filters is listed in Table 7.

Table 7: Filter blocking parameters.

Wavelengths	Blocking
375-500 nm	> OD2
500-550 nm	> OD4
550-850 nm	> OD5
850-900 nm	> OD4
900-950 nm	> OD3
950-1000 nm	> OD2
656-657 nm	> OD5

The use of wavelength-interpolation background estimation in the MSE-MSLP approach is reliant on placing the filters for the proxy measurements in regions free of impurity atomic lines that would skew the polarization correlation between different spectral regions. The prototype and proof-of-principle experiments selected proxy wavelengths depending on both filter availability and trial and error.

To identify promising regions for the proxy measurement, a comprehensive study of impurity lines near the MSE wavelengths was conducted. Known atomic lines for the typical C-MOD impurities are; H, Ar, He, N, Ne, Mo, Fe, C, Kr, W, and Ca. These impurities are not present with the same frequency. H, Mo, and Fe are unavoidable though variable in concentration. Ar is commonly used for x-ray

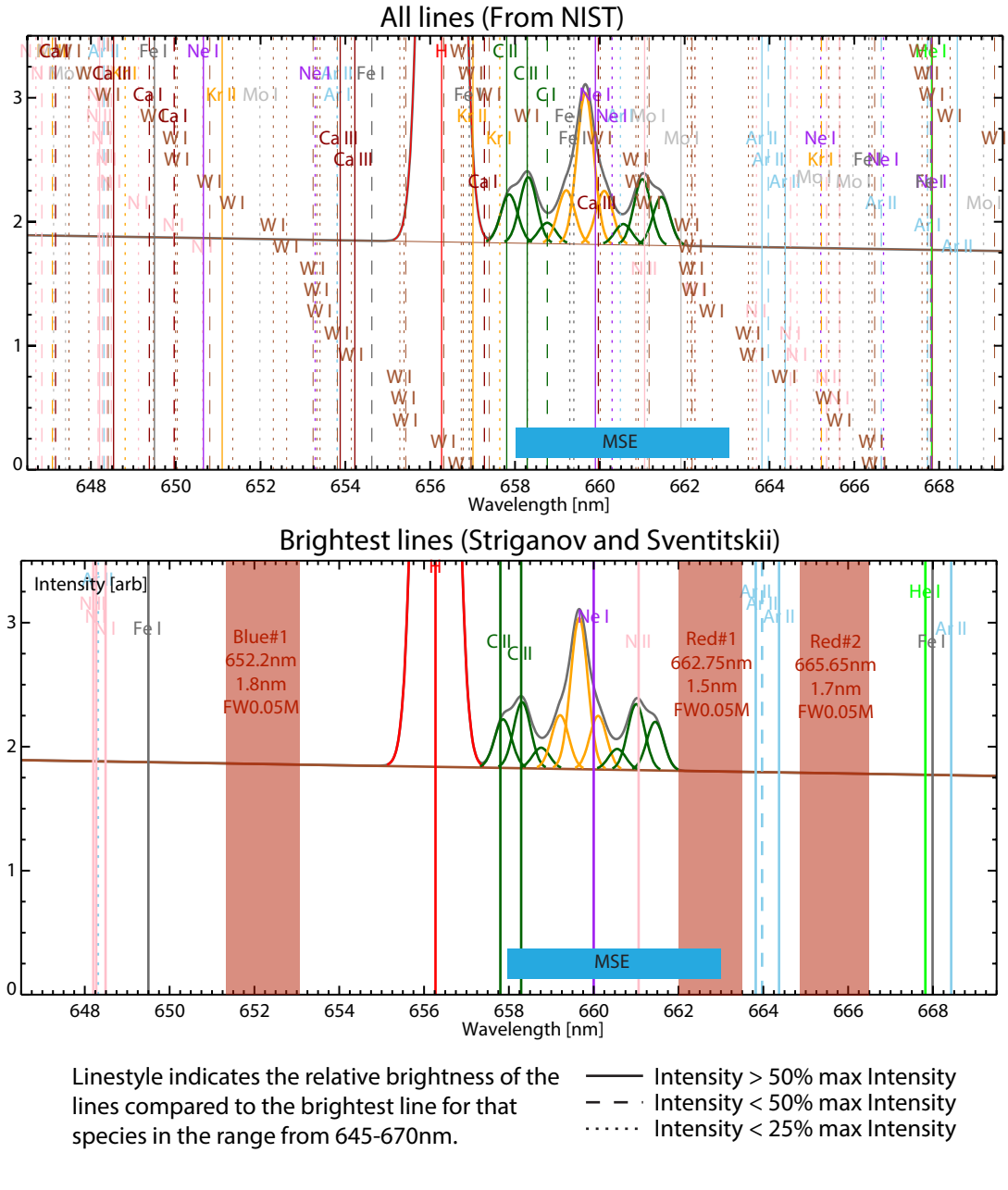

Figure 66: The atomic lines near the MSE wavelengths overplotted on a schematic of the MSE emission. All verified lines from the typical C-MOD impurities were extracted from ref [11] (top). The linestyle indicates the relative brightness compared to the brightest line for that atomic state in the wavelength range from 645nm to 670nm, solid: $> 50\%$, dashed: $25\% - 50\%$, dotted: $5\% - 25\%$ of the max intensity. The brightest lines that appear in ref [12] are shown (bottom). Regions clear of atomic lines are identified as red shaded regions. The MSE wavelengths at 5.4T are indicated with the blue box.

spectroscopy but could be eliminated in some experiments though this would hamper the measurements of T_i and rotation. He, Kr, and Ca are used infrequently as tracers. N and Ne are used for divertor seeding in high power ICRF scenarios. These were extracted from the NIST database [11]. The lines, with the atomic species noted, are shown in the top panel of Figure 66 superimposed on a schematic of the MSE emission. The line style represents the relative strength of the line; solid lines are at least 50 percent as bright as the brightest line in that species (from 645nm to 670nm), dashed lines are less than 50 percent as bright, and the dotted lines are the dimmest, at less than 25 percent but more than 5 percent as bright. It is apparent that the spectral region is full of atomic lines. However, for many species, the brightest line in the region of interest may be fairly dim compared to other sources of background—many of the identified lines are likely very dim or rare. The list of atomic lines was cross-checked with the atomic spectroscopy text Striganov and Sventitskii [12], which lists only the brightest lines for an entire species charge state. These lines are plotted on the lower panel of Figure 66. It is apparent that even though there are many lines, some spectral regions are fairly free from interference.

The high resolution spectrometers on C-MOD were then used to study the MSE spectral region to determine if the identified atomic lines are observable in C-MOD plasmas. Many spectrometer sightlines were used, including views in the both divertors, toroidal views at the midplane, and views through the MSE periscope using the BES system. An example spectrum is shown in Figure 67. The top panel shows spectra from three spectrometer sightlines, a poloidal view through the core (blue), a poloidal view through the lower divertor (red), and a toroidal view through the core (green). The three viewing geometries are shown at the bottom of the figure. The spectra have been normalized to agree at 660nm. Many atomic lines can be seen in the these spectra, with the divertor view having the worst relative contamination. In this particular discharge, there are carbon lines at 658nm, argon lines at 664nm, helium or iron at 668nm, perhaps an iron line at 650nm, and argon or nitrogen at 648nm. Many spectra were obtained in many different discharges, and all of the observed lines were tabulated and are included as vertical lines the top panel.

An important consideration for picking proxy spectral regions is the addition of photon noise to the MSE measurement from using the measurement at the proxy wavelengths. The utility of the wavelength-interpolation technique over the time-interpolation technique will depend on how variable the background is relative to how much random photon noise is injected by using the proxies. The proxy measurements should collect as many photons as possible to limit this source of noise. Therefore, the proxy narrow bandpass filters should

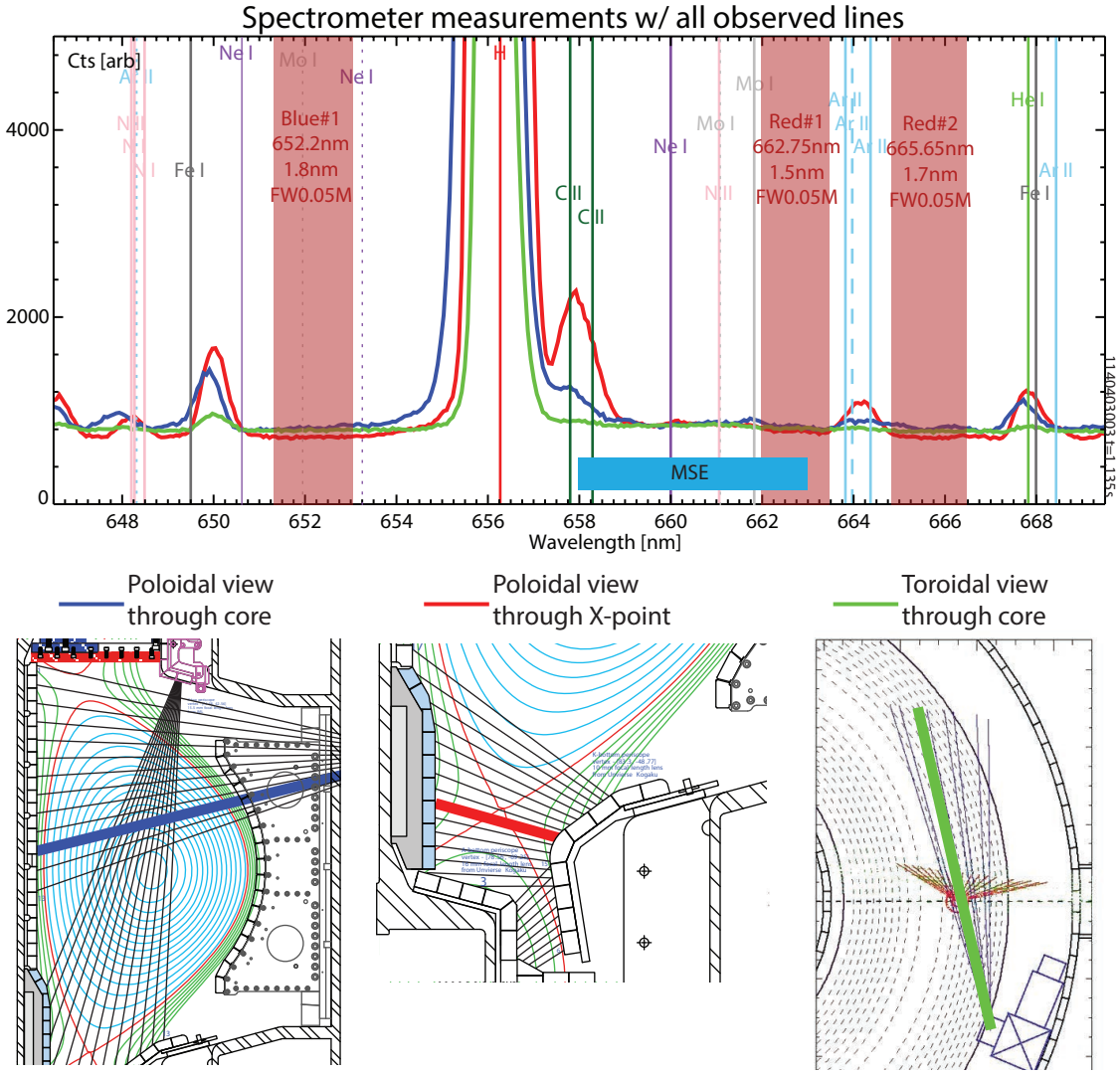

Figure 67: C-MOD's high resolution spectroscopy system was used to examine the MSE spectral region for impurity lines in actual plasmas. The spectra from three spectrometer sightlines are shown (top) with the corresponding spectral views (bottom) for a poloidal view through the core (blue), a poloidal view through the divertor (red), and a toroidal view through the core (green). Identified impurity lines from a variety of discharges are shown as vertical lines with species label. The identified proxy wavelength regions are shown as red shaded regions and the MSE measurement wavelengths at 5.4T are identified by a blue shaded box.

be as wide as possible without overlapping impurity lines or the MSE emission.

As shown in Figures 66 and 67, there are three clean spectral bands near the MSE emission. These are indicated as red shaded areas in the figures. The MSE measurement wavelengths are shown as a blue shaded box. The three measurement regions are:

BLUE #1 Centered at 652.2nm with a full-width 5% max (FW0.05M) of 1.8nm. This bandpass is bounded by a neon line, a possible krypton line, and an unidentified line to the blue, and a neon line to red. It contains a known, but very weak, molybdenum line that are observed during major molybdenum injections.

RED #1 Centered at 662.75nm with a FW0.05M width of 1.5nm. This bandpass is bounded by a molybdenum line at 661.9nm to the blue that is sometimes seen by the MSE system[1] along with the MSE emission from the core sightlines. Bright argon lines are located to the red. These are prominent and strongly polarized and therefore must be avoided. The MSE π emission for the core-most 5 sightlines overlaps this region making it only useful as a proxy for the edge sightlines.

RED #2 Centered at 665.65nm with a FW0.05M of 1.7nm, this bandpass is bounded by the bright argon lines to the blue and helium, argon and iron lines to the red. This region will be used as a proxy for the core MSE sightlines, replacing Red #1.

A new manufacturer[2] that can fabricate narrow bandpass interference filters with a peak transmission of $> 95\%$ (using new hard-coating thin deposition techniques) was identified. This is nearly a factor of two increase in transmission, and thus signal, over existing filter designs. Incorporation of these filters is a significant improvement to the diagnostic performance. However, these high performance filters have small temperature coefficients ($0.004^{nm}/^{\circ}C$), making them difficult to temperature-tune, and the cost of custom individual filters is large. However, the price decreases if the filters are ordered in batches with identical properties. Therefore, these high transmission filters are used for the proxy wavelengths but not the MSE measurements. The specifications for the proxy filters are detailed in Table 8.

Traditional filter technology with large temperature tuning coefficients is used for the filters for the MSE measurements[3]. Some of the existing filter set is reused to lower cost. A previous study undertaken by Paul Geelen [14] used the MSESIM code [13] to simulate the MSE spectrum including all 3D source effects. The results of this study were used to determine the optimum bandpass widths for additional

1 See shot 1120920008 sightlines 06, 07, 08
2 Alluxa www.alluxa.com
3 From Andover Corp www.andover.com

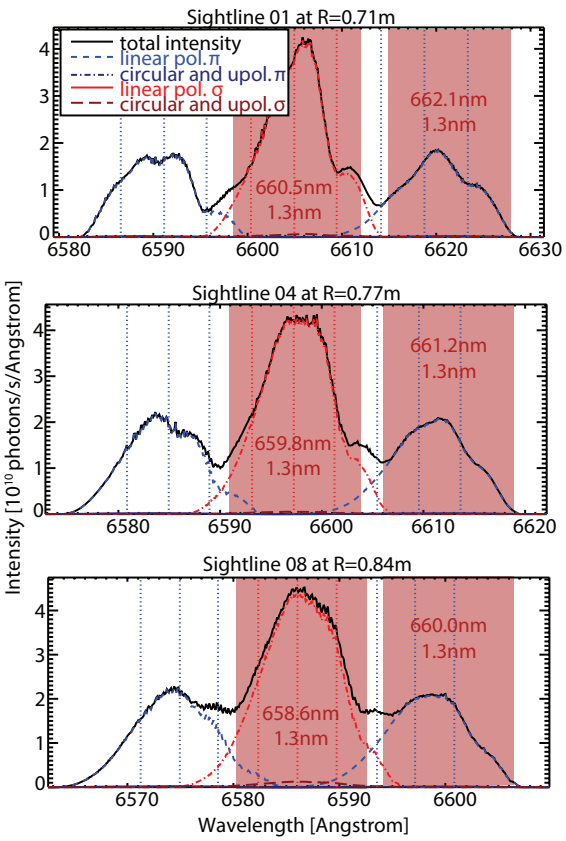

Figure 68: A simulated full energy MSE spectrum using MSESIM[13] for three C-MOD MSE sightlines showing the intensity of the σ and π emission. Adapted from [14]. The shaded regions are the optimized filter bandpass characteristics based on the simulated spectrum showing the center wavelength (top number) and FW0.05M (bottom number). The FWHM in the specification is calculated from this FW0.05M using typical filter shapes.

filters to replace under-performing existing filters and to extend the measurement to the σ emission. The results of the simulations for three sightlines of the full energy beam emission are reproduced in Figure 68. The bandwidth for the MSE filters was chosen so that the MSE π filter collects the entire full-energy π emission with little σ emission and no excess background light, while the MSE σ filter collects all of the full energy σ line, but little of the π lines to either side of it. A bandwidth of 0.8nm FWHM in a 3-cavity filter fits this specification. The bandpass filter regions with transmission $> 5\%$ are shown as red shaded regions in Figure 68. The specifications for the MSE filters are detailed in Table 8.

Figure 69 shows a filter transmission curve for a high performance proxy filter using the new hard coating techniques compared to a transmission curve for the a MSE filter using traditional fabrication techniques. Replacement of the MSE filters with high transmission filters is a future upgrade path in order to increase signal levels. However, a larger temperature coefficient is desired for the high transmission filters. Unfortunately, this this is counter to the direction most of the filter market prefers. Reduction in cost of the high transmission filters for small batches would also represent a significant improvement.

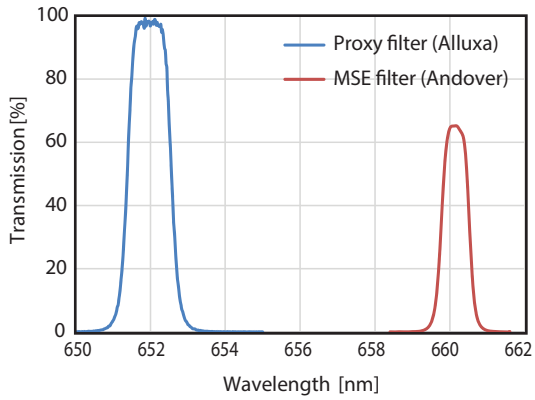

Figure 69: Comparison of the as-measured transmission of the high performance filters used for the proxy measurement (blue) and the standard performance filters used for the MSE measurement (red).

The filter transmission functions are measured in-situ. A small diameter (5cm) integrating sphere assembly is mounted to the polychromator output port in place of a detector. The mount places the sphere's input port at the filtered image location. A fiber is connected between the sphere's output port and a high resolution spectrometer. The integrating sphere ensures the spectrometer measures the fully illuminated filter function instead of only a small set of rays. The polychromator is illuminated with light from the alignment patch fiber and a spectrum is measured both with and without the filter installed in the oven. The ratio of the two spectra yields the transmission curve of the filter. This is then used to properly spectrally tune the filter using the ovens in place of the manufacturer's data.

5.3.3 *Detector design*

The prototype polychromator used off-the-shelf APDs with 10mm diameter elements. These units required a custom second stage amplifier and proved to be expensive and unreliable. The MSE APDs used in the existing system are also 10mm diameter elements. These units require a controllable external high voltage supply ($1.5 - 2$kV), which adds complexity. Furthermore, the packaging of these APDs is too large to be incorporated into the polychromator output port spacing. Both APD types require various voltages to power the APDs and amplifiers, including some voltages at high current.

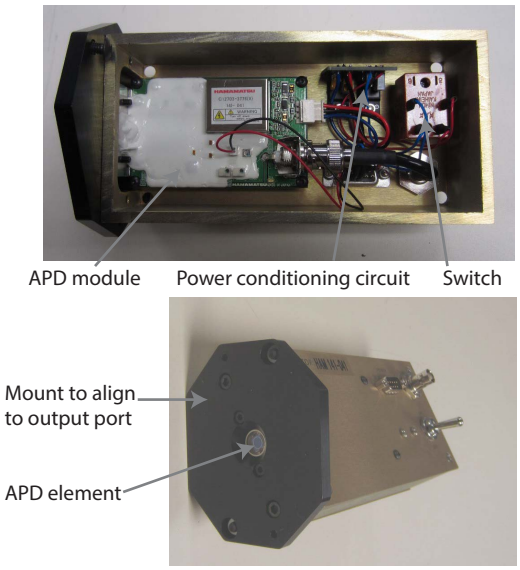

Figure 70: The custom APD modules are installed within an RF shield box along with a switched power conditioning circuit (top). The APD element is precisely positioned on the polychromator image using pin alignment holes in the detector front plate (bottom).

Table 8: General specifications for the proxy and MSE narrow bandpass filters.

Quantity	Specification
Diameter	$50.8 + 0.0 - 0.8$mm
Clear aperture	> 45mm
Thickness	< 10mm
Mounting parallelism	$< 0.1°$
Reflectivity	$> 95\%$
Surface quality	80/50 scratch/dig
Temp coefficient (proxy)	> 0.004nm/°C
Temp coefficient (MSE)	> 0.015nm/°C
Operating Temp	$10 - 100$°C
Angle of incidence	3.0°
Cone angle	$\pm 2.3°$
Max transmission (proxy)	$> 90\%$
Max transmission (MSE)	$> 50\%$
CWL tolerance (proxy)	$+0.0 - 0.5$nm
CWL tolerance (MSE)	± 0.15nm
FW0.05M tolerance (proxy)	$+0.0 - 0.2$nm
FWHM tolerance (MSE)	$+0.0 - 0.2$nm

The high magnification of the optical system allows the image of the fiber to be focused within a < 5mm diameter spot size at F/# ~ 0.8. Therefore, smaller, lower cost APD elements can be used without a decrease in signal. The decision was made to work with a manufacturer to develop a new, low-cost, simple, and standalone APD detector to fit the MSE requirement.

Manufacturers have recently started packaging APDs as compact all-in-one modules for commercial use. One leading manufacturer[4] was contacted to develop a custom APD module for use in the new polychromator system. A 5mm diameter, high sensitivity, un-cooled APD element and a custom trans-impedance and second stage amplifier were incorporated into an off-the-shelf APD module circuit layout. The module includes an on-board high voltage generator that is feedback-stabilized to produce constant gain despite changes in temperature. Functionality was added to control this gain using an external voltage to provide the ability to adjust the APD sensitivity for different plasma scenarios. Each module consumes a small amount of current at ±5V, simplifying the hardware needed for power and control. The module is the size of a business card and costs 1/5 as much as the APDs used in the existing C-MOD system. The detailed specifications of the APD modules are listed in Table 9.

Table 9: APD module specifications

Quantity	Specification
APD active area	5mm diameter
Spectral response	$400-1000$nm
Photo sensitivity	$15^{A/W}$ at 800nm, $M = 30$
Quantum efficiency	$> 70\%$ at 800nm
APD Gain (M)	$10-100$ controllable
Temp stability of gain	$\pm 5\%$ max
Dark current	< 30nA at $M = 40$
Cutoff frequency (-3dB)	> 150kHz
Feedback resistance	2.0MΩ
2nd-stage gain	-5
NEP	$< 100^{fW}/\sqrt{Hz}$ at 800nm
Supply voltage	±5V
Current consumption (+5V)	$50-100$mA
Current consumption (−5V)	$20-40$mA

The APDs used in the existing MSE system were carefully constructed to ensure that the amplification was independent of frequency. There is less of an emphasis on frequency-independent amplification in the new system since the frequency dependence can be easily compensated for through calibration if the need arises. Furthermore, the ISC system provides the final calibration at in a manner that would seamlessly account for any frequency-dependent effects.

A head-to-head test of signal to noise was conducted between a prototype of the new module and the existing MSE detectors. It was found using bench tests that the new detector has a $30-40\%$ lower signal to noise ratio than the existing APDs it replaces. However, head-to-head tests to measure the variability in polarization angle during plasmas showed there was little difference between the two units. This is likely because the noise in the measurement is not limited by detector noise but by fluctuations in the plasma, though this has yet to be quantified. The simplicity, size, and cost advantages of the new modules were significant, thus the decision was made to proceed with a purchase of the new custom APD modules instead of modifying and purchasing more of the existing APDs.

The APD modules are assembled with an RF shield box, power switch, connectors, and a mounting system that can interface with

4 Hamamatsu http://www.hamamatsu.com

Figure 71: The polychromator control hardware with 40 oven controllers and APD gain control all commanded through TCP/IP.

the polychromator output port to align the APD element on the filtered image. A small power conditioning circuit is included in each of the detector assemblies to ensure a clean ±5V power supply. Each detector outputs its signal via a BNC connector grounded at the RF shield box.

5.3.4 *Data acquisition and control system*

The signals from the APD modules are transmitted over BNC cables (RG58) to the CPCI based digitizer[5]. This 16-bit ±2.5V differential input digitizer operates at 500$^{\text{ksamples}}/_{\text{s}}$ with 96 channels, though only 64 channels are enabled. The digitizer has 1GB RAM that allows the 64 channels to be digitized for the full 11.5s long MSE shot cycle. As in the current system, the PEM waveforms and ISC feedback and position signals are also digitized by this system. The system can stream data in near real time to allow for a future real-time MSE upgrade for plasma control. The unit connects to the C-MOD data system through TCP/IP and has various digital and analog inputs and outputs to sequence other tasks. This digitizer replaces a similar, 14-bit, 16-channel system operating at 1000$^{\text{ksamples}}/_{\text{s}}$ from the same manufacturer. Tests confirmed that the decrease in sampling rate does not affect the accuracy of the MSE measurement. The analog lockins and CAMAC digitizers that were used for general diagnostic observation, but not for physics analysis, were retired with the conversion to the new MSE-MSLP system.

The polychromator detectors and ovens are controlled using a set of custom electronics that interface with the network at C-MOD and the MDSPLUS data structure. Each of the 40 individual oven controllers converts the RTD signal to a calibrated temperature. Each controller also contains logic that prevents over-heating in case of a sensor malfunction or an off-normal event. Each controller is connected to a RS-485 serial bus inside the control box and displays the measured temperature and temperature set point on the outside of the control

5 D-TACQ model #: ACQ196-96-2V5 www.d-tacq.com

box. The detector gains are controlled with digital-to-analog convertors that supply a gain control voltage to each of the detectors. An additional digital input and output device controls the power to the detectors en-mass, controls the main power to the ovens, and provides extra digital inputs and outputs that allow the box to control external components such as the cooling water supply. All of these controllers are connected to the serial bus. The control hardware is shown in Figure 71.

The serial bus connects to hardware that transfers data between the bus and the TCP/IP network in the diagnostic lab. This allows the ovens to be enabled or disabled, their temperature to be set or read, the detectors to be turned on or off, and their gains to be set remotely over the internet. This hardware replaces a substantial amount of dated and hard-to-service CAMAC-based control hardware with more compact and simpler equipment, all contained within a small box. Furthermore, the new hardware has a maximum voltage of 120V instead of 2000V, removing equipment that was subject to more stringent safety procedures. An additional upgrade is planned to replace the PEM control and monitoring hardware with a TCP/IP-enabled system. When this happens, the entire MSE diagnostic including PEMS, ovens, detectors, digitizer, ISC and robotic calibration subsystems will be controllable remotely over the Internet.

5.3.5 *Implementation*

The mechanical design allows 10 polychromators, along with all necessary power and control equipment, cabling, and tubing, to be incorporated in a single, full-height, 19-inch wide standard electronics rack. This modular design is easy to integrate into the diagnostic lab and requires only a network connection and 120VAC power. The system replaces a larger footprint of existing hardware. The system accepts the MSE sightline fibers with small modifications to the ferrules.

The cost breakdown for the system is shown in Figure 72. The most expensive items are the filters, component machining, and detectors. The remaining components cost significantly less. The total cost of \$21000 per sightline is within the target of $< 2\times$ the $\sim$ \$11000 cost per sightline for the existing MSE APD, filter, and oven combination. This is a significant value given the increased capability of the MSE-MSLP system, especially considering the system has $> 2\times$ the signal than the existing system through utilization of the MSE σ and π lines simultaneously.

As of this writing, the system has been installed in the diagnostic hall and has been calibrated using the robotic calibration system and has observed first light from the plasma. Photographs of the system are shown in Figure 73. Hardware assembly and testing is complete, though the system requires further in-situ calibration of the filter func-

Figure 73: Photographs of the 10-sightline multi-spectral system during assembly. The 10 polychromators assembled in the lab with top covers removed (left) along with the author and his thesis advisor. The 10 polychromators with their control system assembled into the electronics rack in the MSE area of the C-MOD diagnostic hall (right).

tions and calibration of the detector sensitivities. Software to manage and control the various sub-systems and interface with the MDSPLUS database is under construction. Further work is required to modify the MSE analysis codes to utilize the multi-spectral technique and to handle the large increase in data from the MSE system. The analysis techniques are likely to be modified in the future as experience is gained using the multi-spectral system with wavelength interpolation in a variety of plasmas.

The system is nearly tokamak independent, requiring only a filter and fiber ferrule change to operate on other tokamaks. Since C-MOD's MSE system has the largest sightline étendue, the polychromators can replace existing detectors at the other tokamak facilities without any loss of signal. Additionally, the network architecture of the system allows it to be commanded remotely, making off-site collaboration easier. These attributes make it likely that the system will be transfered to another tokamak at the end of C-MOD operations.

5.3.6 *Calibration strategies*

The standard MSE-LP technique uses a single filter and detector combination to measure the polarization from the beam. This attribute gives the technique its high accuracy relative to other techniques to measure the magnetic geometry. Furthermore, in the standard MSE-LP technique, the same detector and filter are used to make the measurement of the background before and after the beam pulses. Thus, there

is no need to calibrate the gain of the detector and throughput of the filter to subtract the background or for any other fundamental reason.

The use of MSE-MSLP requires that different detectors and filter combinations be multiplexed into the estimate of the background. Fortunately, the polarization angle from the beam σ or π is still measured with a single detector and the other detectors only influence this measurement through background subtraction. To subtract the background, the Stokes vectors from the two proxy regions must be scaled to agree with the measurement of the MSE background. To do this properly, the gain of the detectors and the transmission of the filters used for the proxy measurements must be accounted for. This can be done by inputing white light into the polychromator and measuring the response of the four different detectors.

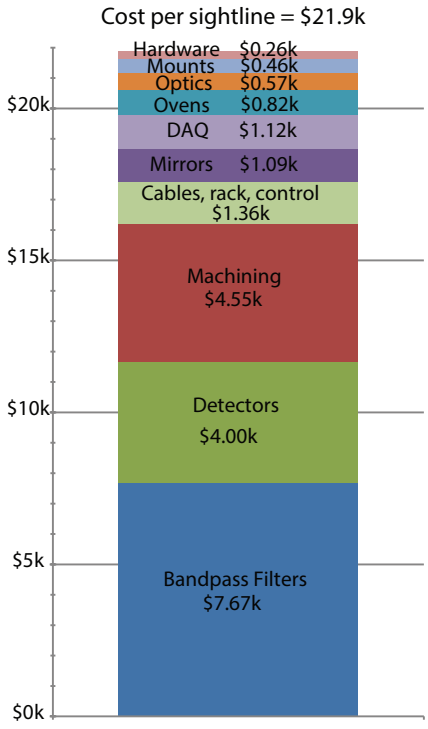

Figure 72: Polychromator costs per sightline.

The prototype experiments used time windows within a plasma to normalize the gains of the different wavelength channels and equal weighting of both proxy wavelengths: $C_{red} = C_{blue} = 0.5$. This proved to be fairly successful at estimating the background. However, there are many ways to obtain the relative gain calibrations, and methods are listed here in order of most desirable to least desirable:

1. White light through only the polychromator occasionally
2. White light from the ISC
3. Simple plasmas with only visible bremsstrahlung
4. Beam-off periods within each discharge

Each of these capabilities will be available in the full implementation of the MSE-MSLP technique and will be cross-compared once the system is operational. In the simplest case, the gains are constant in time and only need occasional updating. In the most unfavorable case, the gains need to be updated multiple times within a discharge, though it is difficult to see why this would occur (there are no indications of requiring this approach from experience with the prototype system). Additionally, the new system is thermally stabilized in an attempt to provide constant APD gain.

The weightings of the different proxies will have to be evaluated. These could include weightings based on spectral separation or inverse noise level. If the background spectrum is non-monotonic and its spectral shape changes significantly within a discharge, these weightings may need to be updated during beam-off periods.

The full MSE-MSLP system will also explore how to combine the two orthogonal MSE measurements to better understand systematic polarization angle errors. This will be completed for sightlines that do not have contamination from lower energy beam components. The C-MOD MSE system does not have problems with mirror diattenuation, so this cannot be investigated. However, the system can have time-dependent retardance from stress-induced birefringence (when the thermal management systems are disabled). Therefore, the system will be used to explore whether or not measurements of σ and π can be used to track these changes. The system will also explore how the orthogonal polarizations can be used to monitor the ability to estimate the background.

Experience with the new C-MOD MSE-MSLP system will shed light on these issues, and will also explore the limits of how well the background can be subtracted using wavelength-interpolation. Hopefully, it will further inform the design of next-generation MSE systems.

BIBLIOGRAPHY

[1] T. N. Carlstrom, J. C. DeBoo, R. Evanko, C. M. Greenfield, C.-L. Hsieh, R. T. Snider, and P. Trost. A compact, low cost, seven channel polychromator for Thomson scattering measurements. *Review of Scientific Instruments*, 61(10):2858, 1990.

[2] F. Orsitto, A. Brusadin, E. Giovannozzi, D. Santi, R. Bartiromo, and P. Pizzolati. Thomson-scattering diagnostic on the Frascati tokamak upgrade. *Applied Optics*, 34(15):2712–2718, May 1995.

[3] J. W. Hughes, D. Mossessian, K. Zhurovich, M. DeMaria, K. Jensen, and A. Hubbard. Thomson scattering upgrades on Alcator C-Mod. *Review of Scientific Instruments*, 74(3):1667–1670, March 2003.

[4] Yang Li, Zhao Junyu, and Fang Zishen. The Design of the Polychromator for Thomson Scattering Measurements on HT-7 Tokamak. *Plasma Science and Technology*, 6(4):2383–2386, August 2004.

[5] Y. Huang, P. Zhang, Z. Feng, C. H. Liu, P. L. Shi, X. T. Ding, and Yong Liu. The development of Thomson scattering system on HL-2A tokamak. *Review of Scientific Instruments*, 78(11):113501, 2007.

[6] J. Cantarini, J.P. Knauer, and E. Pasch. Studies for the design of the Wendelstein 7-X Thomson Scattering polychromators. *Fusion Engineering and Design*, 84(2-6):540–545, June 2009.

[7] D. Dimock, B. Grek, D. Johnson, B. LaBombard, B. Lipschultz, and G. McCracken. A compact Thomson scattering system. *Review of Scientific Instruments*, 68(1):700, 1997.

[8] P. H. Lissberger and W. L. Wilcock. Properties of All-Dielectric Interference Filters. II. Filters in Parallel Beams of Light Incident Obliquely and in Convergent Beams. *Journal of the Optical Society of America*, 49(2), February 1959.

[9] Irving H. Blifford. Factors Affecting the Performance of Commercial Interference Filters. *Applied Optics*, 5(1):105–111, January 1966.

[10] M. G. Lofdahl, V. M. J. Henriques, and D. Kiselman. A tilted interference filter in a converging beam. *Astronomy & Astrophysics*, 533:A82, September 2011.

[11] A. Kramida, Yu Ralchenko, J. Reader, and NIST ASD Team. NIST atomic spectra database (version 5.2) [online]. available: http://physics.nist.gove/asd, 2014.

[12] A. R. Striganov, N. S. Sventitskii, and A. R. Striganov. *Tables of spectral lines of neutral and ionized atoms*. New York, IFI/Plenum, 1968., 1968.

[13] M. F. M. De Bock, N. J. Conway, M. J. Walsh, P. G. Carolan, and N. C. Hawkes. Ab initio modeling of the motional stark effect on MAST. *Review of Scientific Instruments*, 79(10):10F524, 2008. Printed.

[14] Paul Geelen. *Simulation of the Motional Stark Eeffect on C-MOD using MSESIM and PERF*. Internship report, Eindhoven University of Technology, 2013.

6 CONCLUSIONS

The hardware designed and implemented as part of this thesis has led to greater understanding of the operation of MSE diagnostics and to the successful operation of the C-MOD diagnostic. This will enables future physics studies, including studies of LHCD using the upgraded diagnostic across a wider range of plasma regimes.

6.1 ROBOTIC CALIBRATION OF MSE DIAGNOSTICS

A robotic calibration system has been developed for the ALCATOR C-MOD MSE diagnostic that is able to illuminate the diagnostic with polarized light from known positions along the path of the C-MOD diagnostic neutral beam during maintenance periods. The system consists of a positioning system capable of precise 3D alignment inside the vessel and a polarization generation head that creates arbitrary polarization states with orientations known with respect to gravity to $< 0.05°$.

The automation, speed, and repeatability of the robotic calibration system has allowed systematic errors in the MSE polarization measurement to be studied extensively and the diagnostic operation to be optimized. The high accuracy of the system likely leaves the orientation of the toroidal field relative to gravity as the largest remaining uncertainty in the polarization calibration. Unlike other MSE calibration techniques, these techniques do not require any plasma or beam-into-gas discharges, eliminating impacts on machine operation for diagnostic calibration except for occasional checks on the diagnostic operation. The nature of the robotic calibration allows it to be used on other facilities to calibrate other MSE diagnostics. The linear stage would need to be replaced with one the length of the beam line, but all other components and methodologies would transfer easily.

6.2 INTER-SHOT CALIBRATION OF THE MSE DIAGNOSTIC

The ISC system provides a high-quality reference calibration of the MSE diagnostic within seconds of every discharge throughout the campaign. The flexibility of the system bridges the gap between the very flexible and accurate calibrations performed during maintenance periods and interpreting the diagnostic state when the vessel is under vacuum using beam into gas and plasma discharges. The ISC system's repeatability, calibration, and use for determining the diagnostic response is covered elsewhere. The system has been operational inside

the C-MOD vacuum vessel since the FY12 experimental campaign. The uniformity of the illumination was upgraded for the FY14 campaign to better capture the diagnostic calibration. Since the system's installation, it has performed over 8000 actuations, with approximately half occurring in vacuum. There has not been any sign of mechanical performance deterioration.

6.3 THERMAL CONTROL OF THE MSE PERISCOPE

The realization that stress-induced birefringence can be important in any transmissive element led to the deployment of systems to provide a uniform and constant a temperature environment for the entire MSE optical train. This was a challenge in such a demanding and harsh thermal environment. The slow pace of iteration—changes can only be made once a campaign—further added to the challenge.

Unique strategies were applied for the internal and external optics, greatly improving the thermal environment by slowing transients and smoothing gradients. Tests show that this approach was successful in eliminating the diagnostic drift due to thermal-stress induced birefringence. Though the techniques deployed on C-MOD are not directly applicable to future devices, this work highlights the importance and feasibility of controlling external environmental variables which cause changes to the diagnostic response using a comprehensive approach.

6.4 DEVELOPMENT OF A HIGH-THROUGHPUT POLYCHROMATOR

A high throughput polychromator was successfully designed and built which splits the light from a single sightline into four different wavelength bins, passing it to an APD detector. This system allows multiple narrow bandpass filters to be operated on a single sightline simultaneously with very high photon efficiency. The system is flexible, with ovens that tune the filter wavelengths. The system small cavity angle provides good spectral selectivity and the system proved easy to align.

Success with a prototype system led to the development of a second generation system to replace all the existing single wavelength MSE detectors on C-MOD with new polychromator detectors which will enable wavelength interpolation of the partially polarized background. This sytle of detector is anticipated for use on ITER.

COLOPHON

This document was typeset using `classicthesis` developed by André Miede (although aspects were changed to comply with the MIT thesis standards and the author's personal preferences). The style was inspired by Robert Bringhurst's seminal book on typography "*The Elements of Typographic Style*". `classicthesis` is available for both LaTeX and LyX:

http://code.google.com/p/classicthesis/

Final Version as of June 23, 2015 (`classicthesis` version 4.1).

Hermann Zapf's *Palatino* and *Euler* type faces (Type 1 PostScript fonts *URW Palladio L* and *FPL*) are used. The "typewriter" text is typeset in *FPL*, originally developed by Bitstream, Inc. as "Bitstream Vera". (Type 1 PostScript fonts were made available by Malte Rosenau and Ulrich Dirr.)